HYSTERESIS AND PATTERN FORMATION IN ELECTRONIC PHASE TRANSITIONS IN QUANTUM MATERIALS

A Dissertation

Submitted to the Faculty

of

Purdue University

by

Sayan Basak

In Partial Fulfillment of the

Requirements for the Degree

of

Doctor of Philosophy

December 2020

Purdue University

West Lafayette, Indiana

THE PURDUE UNIVERSITY GRADUATE SCHOOL
STATEMENT OF DISSERTATION APPROVAL

Prof. Erica W. Carlson, Chair

Department of Physics and Astronomy

Prof. Gábor Csáthy

Department of Physics and Astronomy

Prof. Yuli Lyanda-Geller

Department of Physics and Astronomy

Prof. Sergei Khlebnikov

Department of Physics and Astronomy

Approved by:

Prof. John Finley

Department of Physics and Astronomy

To my parents and my brother.

ACKNOWLEDGMENTS

Graduate school plunges one into the trenches. It has been a constant eddying back and forth, a journey that often entailed walking backward, going back to the roots. It is my advisor who has been at the root of all of this, the constant light guiding me through this tunnel. It is her belief in me, her critical inputs, her generosity and openness that has made every discovery, big and small, possible. Thank you, Prof. Erica Carlson, for taking a shot at me, for giving me the freedom to explore possibilities, for your continued kindness and patience, for mentoring me, for breaking down concepts, helping with every aspect of what I have here. She will always be an academic role model I look up to. Going forward, it is her work ethic and generosity I wish to embody in future workplaces. Thank you so much for teaching me so much these past few years.

I am thankful for the insights my committee, namely, Prof. Gabor Csathy, Prof. Yuli Lyanda-Geller, Prof. Sergei Khlebnikov, provided all these years. I am also very grateful to my collaborators, Prof. Karin Dahmen and Prof. Alexandre Zimmers, for sharing their valuable experience and immense guidance in the critical parts of this thesis. I thank all the faculty and administrative staff of the Physics and Astronomy department at Purdue University. A special acknowledgment is definitely in order for Sandy Formica and Janice Thomas for the innumerable times I sought their help during this period.

I would like to extend my gratitude to my teacher, Anirban Sir, who kindled my interest in Physics and Mathematics in high school. I also cherish the guidance of Late Prof. G.V. Pai, who gave me the final push I needed to jump into this mammoth venture.

So many people have rallied together, been constant cheerleaders, purveyor of everything beautiful and light —I will always remember them with fondness. To

Sambit, Mohit, and Ashish for first opening up their hearts and space, by taking in a stranger, when I came to Purdue in 2014. To Sambit, who has become that force in my life whom I have come to rely on for everything —it is his incredible warmth and sound advice that has kept me going for many years now. To Mohit, his stories, his ready help, his industriousness, his practical skills —I feel so lucky to have had the privilege of his friendship and guidance. To Abhishek, my first flatmate, his vivacity, his humor, his easy camaraderie, I fondly remember my first two years at Anthrop Drive. To Tarutal, my second flatmate, his recipes, the spirited discussions, his easy warmth —every bit of the living situation was so pleasant the last four years. To my long-suffering friends —the one who has been in this for the long haul since my school days to always being there through thick and thin —Tamaghna; the one who shares my enthusiasm for new ventures —Soumyajit; and Souvik, his indefatigable energy, and quirkiness that has been the centerpiece of my funniest memories from my IIT days, and the many subsequent San Diego trips later —you all mean the world to me. I also want to thank SayanDa for his critical inputs during the final stages of my project.

To all the trips I made to upstate New York to meet my partner, Amrita —her love and sustained friendship have been a mainstay for all these years. Despite all the odds, the many balancing acts, this has been a sliver of home and belonging, I have always thrived on. I am happy that I got to experience the conclusion of my grad school journey with her by my side. To Satadisha, Anrin, Amrita, the inmates of the "59 Schiller" group at the beginning of this bizarre year, thank you for making the lockdown social distancing experience one of the highlights of this year. I fondly remember our card games, marathon movie sessions, and the constant cheerful banter that saw us through this strange dark year.

To my family, my mother, father, and brother, who has been the underlying palimpsest to all these journeys —it is their continued faith and endless love that has nourished me through all these years. They are the cornerstones of every achievement.

Thank you for supporting me in everything. Nothing would be possible without you all.

TABLE OF CONTENTS

Page

LIST OF TABLES

LIST OF FIGURES

Figure Page

Figure Page

Figure Page

Figure Page

Figure Page

Figure Page

Figure Page

Figure Page

ABSTRACT

Basak, Sayan PhD, Purdue University, December 2020. Hysteresis and Pattern Formation in Electronic Phase Transitions in Quantum Materials. Major Professor: Erica W. Carlson.

We propose an order parameter theory of the quantum Hall nematic in high fractional Landau levels in terms of an Ising description. This new model solves a couple of extant problems in the literature: (1) The low-temperature behavior of the measured resistivity anisotropy is captured better by our model than previous theoretical treatments based on the electron nematic having XY symmetry. (2) Our model allows for the development of true long-range order at low temperature, consistent with the observation of anisotropic low-temperature transport. We furthermore propose new experimental tests based on hysteresis that can distinguish whether any two-dimensional electron nematic is in the XY universality class (as previously proposed in high fractional Landau levels), or in the Ising universality class (as we propose). Given the growing interest in electron nematics in many materials, we expect our proposed test of universality class to be of broad interest.

Whereas the XY model in two dimensions does not have a long-range ordered phase, the addition of uniaxial random field disorder induces a long-range ordered phase in which the spontaneous magnetization points perpendicular to the random field direction, via an order-by-disorder transition. We have shown that this spontaneous magnetization is robust against a rotating driving field, up to a critical driving field amplitude. Thus we have found evidence for a new non-equilibrium phase transition that was unknown before in this model. Moreover, we have discovered an incredible anomaly at this nonequilibrium phase transition: the critical region is accompanied by a cascade of period multiplication events. This physics is reminiscent of the period bifurcation cascade signaling the transition to chaos in nonlinear systems,

and of the approach to the irreversibility transition in models of yield in amorphous solids [1,2]. This period multiplication cascade is surprising to be present in a statistical mechanics model, and suggests that the non-equilibrium transition as a function of driving field amplitude is part of a larger class of transitions in dynamical systems. Moreover, we show that this multi-period behavior represents a new emergent classical discrete time-crystal, since the new period is robust against changes to initial conditions and low-temperature fluctuations over hundreds of driving period cycles. We expect this work to be of broad interest, further encouraging cross-fertilization between the rapidly growing field of time-crystals with the well-established fields of nonequilibrium phase transitions and dynamical systems.

Geometrical configurations gave us a better understanding of the multi-period behavior of the limit-cycles. Moreover, surface probes are continually evolving and generating vast amounts of spatially resolved data of quantum materials, which reveal a lot of detail about the microscopic and macroscopic properties of the system. Materials undergoing a transition between two distinct states, phase separate. These phase-separated regions form intricate patterns on the observable surface, which can encode model-specific information, including interaction, dimensionality, and disorder. While there are rigorous methods for understanding these patterns, they turn out to be time-consuming as well as requiring expertise. We show that a well-tuned machine learning framework can decipher this information with minimal effort from the user. We expect this to be widely used by the scientific community to fast-track comprehension of the underlying physics in these materials.

1. OVERVIEW

1.1 Symmetry of underlying Nematic

A 2D Electron Gas(2DEG) in the presence of moderate to strong magnetic fields exhibits the Integer Quantum Hall Effect. In moderate to weak magnetic fields, which imply high Landau level occupancy, and temperature below $\sim$ 100mK, anisotropy in longitudinal resistivity is observed at half integer filling $\nu = m + 1/2$, for $m \geq 4$ (Fig. 1.1) [3].

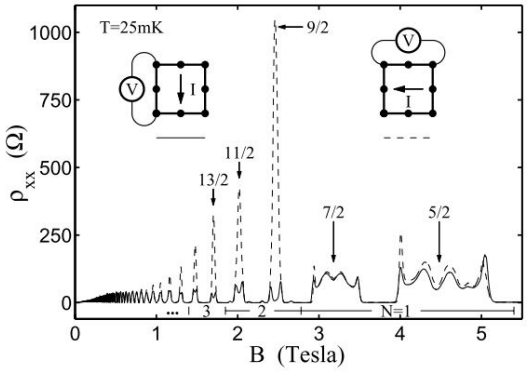

Figure 1.1. Reprinted figure 3 with permission from [(Ref. [3]) M. P. Lilly, K. B. Cooper, J. P. Eisenstein, L. N. Pfeiffer, and K. W. West. Phys. Rev. Lett., 82, 394, 1999.] Copyright (2020) by the American Physical Society. The anisotropy in the longitudinal resistivity along crystalline axes at 25mK as reported by Lilly et al. [3]. The solid line gives the longitudinal resistivity along the $\langle 1\bar{1}0 \rangle$ and the dashed line, along $\langle 110 \rangle$. This shows that the easy transport occurs parallel to the $\langle 1\bar{1}0 \rangle$ crystal axis of the GaAs.

The Integer Quantum Hall effect (IQHE) by itself cannot justify the anisotropic longitudinal resistivity in between IQHE plateaus. At high fractional Landau levels, uniform quantum Hall phases are unstable to the formation of stripe and bubble

phases, with the stripe phases being preferred near high half-filling [4]. This state has been identified as a nematic quantum Hall metal (NQHM), an oriented, compressible stripe phase of interleaved integer quantum Hall states [5, 6].

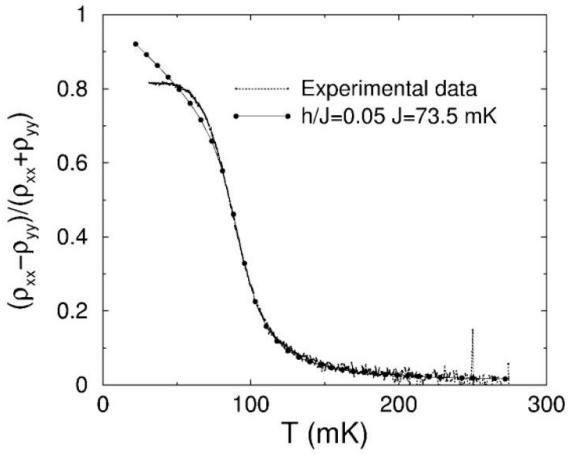

Figure 1.2. Reprinted figure 2 with permission from [(Ref. [5]) Eduardo Fradkin, Steven A. Kivelson, Efstratios Manousakis, and Kwangsik Nho. Phys. Rev. Lett., 84, 1982, 2000.] Copyright (2020) by the American Physical Society. The resistivity anisotropy defined as the $\rho_a = (\rho_{xx} - \rho_{yy})/(\rho_{xx} + \rho_{yy})$ plotted as a function of temperature from experimental data. The simulation result from a lattice 2D XY model is a reasonable match with the experiment only down to T=55mK in the presence of a weak symmetry breaking field.

Fradkin *et al.* [5] developed an order parameter theory of the nematic to describe the temperature evolution of the resistivity anisotropy. Using symmetry to map the resistivity anisotropy to the nematic order parameter, they showed that the temperature evolution of the resistivity anisotropy in the $\nu = 9/2$ state is well described by a classical 2D XY model, with a weak uniform symmetry-breaking field, through the onset of the resistivity anisotropy as the temperature is lowered below $T \sim 150$mK, with deviations from the theory appearing below $T \sim 55$mK (See fig. 1.2). This model places the transition in the BKT universality class [7, 8].

One difficulty with this identification is that a true BKT transition does not break symmetry, and in fact in that model long-range order of a nematic is forbidden at

finite temperature. However, as stressed in Ref. [5], the nematic susceptibility is sufficiently strong in the BKT phase that net nematicity can develop anyway in the presence of even a weak uniform orienting field. Note that without the development of net nematicity, the resistivity anisotropy would be zero.

In chapter 2 we address the above discrepancy, devise a protocol to distinguish an Ising from an XY nematic, and demonstrate evidence of Ising character in these materials.

1.2 Emergent Ising symmetry from Order-by-Disorder Phenomenon

A system where long-range order is stimulated by disorder in the system, but does not order otherwise is termed as order-by-disorder or disorder-induced order. [9–15]

The 2D XY model does not have long-range order at low temperature and in the presence of disorder naively one would expect the system goes to a more disordered state. But there is a type of disorder that promotes order in this system - Uniaxial Random Field Disorder. The random fields are only along one axis in the spin subspace. In the case of a nematic, this type of disorder maps to two mutually perpendicular axes. Similar to a crystalline field giving rise to a uniform field, it can also give rise to random field disorder along the crystalline axes.

The uniaxial random field XY model on a square lattice, in the presence of an external field $\vec{H}[\phi]$ is given by:

$$\begin{aligned}\mathcal{H} = -J \sum_{\langle i,j \rangle} \cos\left(\theta_i - \theta_j\right) \quad &- \quad \sum_i h_i \cos\left(\theta_i\right) \\ &- \quad H \sum_i \cos\left(\theta_i - \phi\right), \end{aligned} \tag{1.1}$$

where $\vec{S}_i \equiv (\cos(\theta_i), \sin(\theta_i))$ is the XY spin on each site i, and J is the nearest neighbor interaction strength. The second term arises from the interaction of a local random field along the x-axis and the XY spins. We choose a random field h_i at each site i from a Gaussian probability distribution of width R_x, $P(h_i) = exp[-h_i^2/(2R_x^2)]/(\sqrt{2\pi R_x^2})$.

The order parameter is the magnetization per site $\vec{m} = \frac{1}{N}\sum_{i=1}^{N}\vec{S}_i$, where $N = L \times L$ is the number of sites.

The results from Monte Carlo simulations of Eqn. 1.1 in thermal equilibrium are demonstrated to shed light on the order-by-disorder transition and its robustness against applied field and temperature. We employ a Metropolis algorithm with checkerboard updates, in which one Monte-Carlo sweep (MCS) updates black sites and then white sites. We follow a field-cooling protocol in which the system is started at a high temperature of $T = 2J$, then we reduce the temperature in steps of $\Delta T = 0.05J$ until $T = 0.05J$. At each temperature step, we thermalize the system with 128,000 MCS and then take 12,800 measurements which are taken randomly between 1 MCS and 16 MCS.

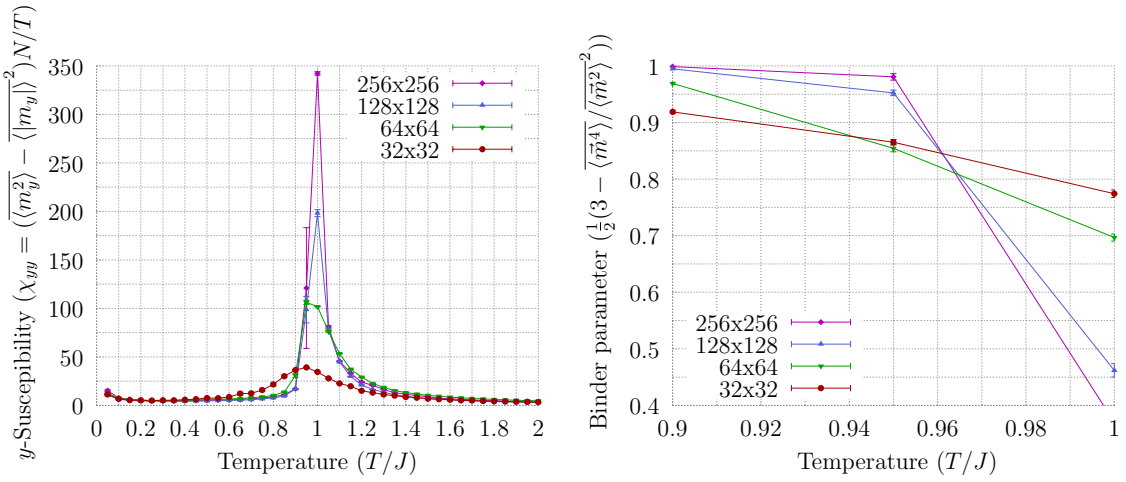

(a) Susceptibility of y-magnetization at $R_x = 0.5J$ (b) Binder parameter *vs.* temperature, at $R_x = 0.5J$

Figure 1.3. Susceptibility to order and Binder parameter at moderate uniaxial disorder strength, $R_x = 0.5J$. (a) The magnetic susceptibility (χ_{yy}) in the y direction peaks near $T_c \simeq J$, and diverges as the system size is increased. (b) The Binder parameter yields a transition temperature $T_c \simeq 0.96J$, consistent with the peak in the magnetic susceptibility shown in panel (a).

It is known that the presence of uniaxial random field disorder in the x direction ($R_x > 0$) favors spontaneous symmetry breaking in the form of ferromagnetic order in the y direction, [9, 13, 16, 17] via an order-by-disorder mechanism. Bera *et al.* have used mean-field theory on the classical XY magnet to argue that the order-by-disorder phenomenon is robust against an applied uniform magnetic field. [14] Indeed, our simulations at moderate uniaxial random field strength $R_x = 0.5J$ are consistent with spontaneous symmetry breaking in the y direction, and indicate that this phase is rather robust against disorder strength. In Fig. 1.3, we show that the magnetic susceptibility in the y direction diverges with system size at the transition temperature $T_c = 0.96J$ determined from the Binder parameter.

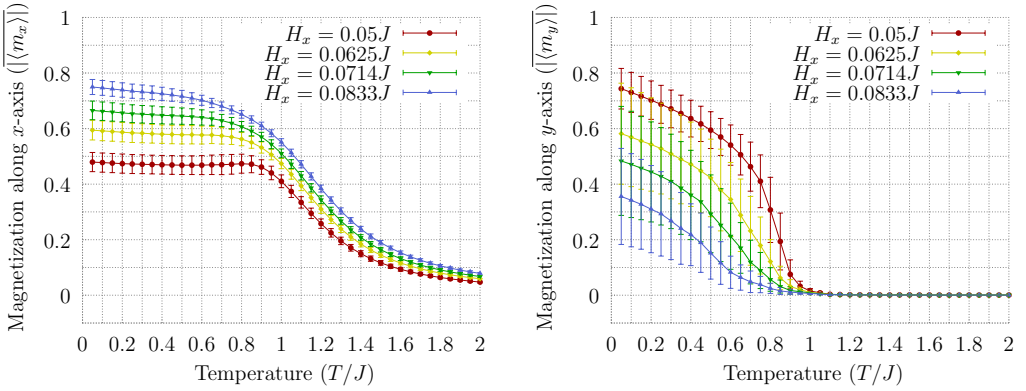

(a) $R_x = 0.5, R_y = 0.0, m_x(T),\ N = 128^2$ (b) $R_x = 0.5, R_y = 0.0, m_y(T),\ N = 128^2$

Figure 1.4. Transverse field cooling at $R_x = 0.5J$. (a) Magnetization in the x direction m_x and (b) magnetization in the y direction m_y in the presence of both uniaxial random field disorder R_x *and* an applied uniform field H_x. The spontaneous magnetization m_y remains robust at finite disorder strength and in the presence of a uniform field applied transverse to the ordering direction.

This order-by-disorder transition is robust even against a uniform field applied parallel to the uniaxial random field. Our simulations of cooling in a uniform applied field parallel the uniaxial random field direction (see Fig. 1.4) show that an order

parameter develops in the direction perpendicular to the uniaxial random field, even in the presence of an applied field. This shows that the spontaneous magnetization m_y is robust even for moderate random field $R_x = 0.5J$, and finite uniform applied field H_x, as shown in Fig. 1.4(b), consistent with the mean field results of Ref. [14].

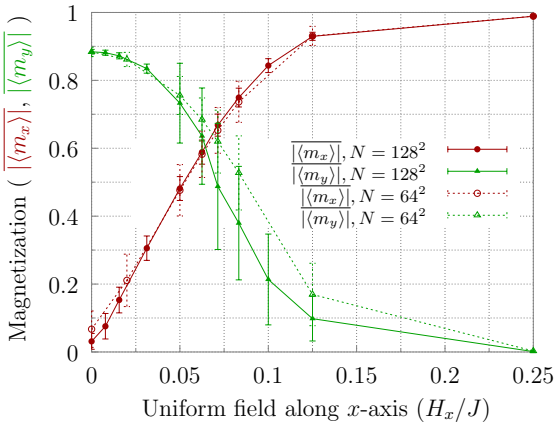

(a) $T = 0.05J,\ R_x = 0.5J,\ R_y = 0$

Figure 1.5. Field cooling. Equilibrium, field-cooled magnetizations in the x and y direction, with applied field along the axis of the random field disorder $\vec{H} \parallel R_x$ with $R_x = 0.5J$, as described in the text. The horizontal axis is the value of the applied uniform field H_x during the field-cooling protocol. Upon field cooling with $H_x \lesssim R_x/10$, the net magnetization in the y direction m_y dominates over the net magnetization in the x direction m_x. This illustrates the robustness of the spontaneous magnetization in the y-direction even in the presence of an applied transverse field.

With strong enough transverse applied field H_x, the order-by-disorder phenomenon must be suppressed and the system will remain in the paramagnetic phase. Fig. 1.5 shows this crossover of the dominant magnetization from the y-axis to the x-axis with increasing applied transverse field.

In chapter 3 we probe this system with a rotating driving field at zero temperature to uncover a rich non-equilibrium phase diagram, non-repeatability, and possible connections to time-crystal and chaotic systems all happening near the critical region.

1.3 Categorizing Surface Probe images

Surface probes have been around since 1982 and their number and types are increasing, each with its specialization. [18, 19] The copious amounts of data they provide are crucial for understanding materials down to the atomic scale. Near a phase transition, patterns emerge which are self-similar at multiple length scales, much like fractals. [20, 21] These geometric clusters bring out the statistical models describing the system. While a precise analytical tool is cumbersome and requires expert knowledge in the specific area, a machine learning approach can act as complementary tools for a similar result with the least amount of effort. [22] Since a deep learning framework with convolutional networks leads the field of pattern recognition, we can utilize it for a similar purpose and improve upon the existing framework so that it can be widely used.

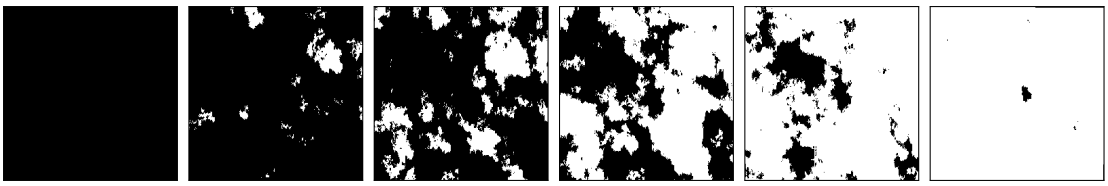

(a) T=341K (b) T=342.4K (c) T=342.6K (d) T=342.8K (e) T=343K (f) T=343.6K

Figure 1.6. (a-f): Adapted figure 1 with permission from Ref. [23]. Copyrighted by the American Physical Society. Thresholded s-SNIM data at intensity 2.5. The white region is metallic and the black region is insulating.

A typical example of the type of experimental data we can analyze after thresholding it appropriately as shown in figure 1.6(a-f). This data was collected by a scattering scanning near-field infrared microscope (s-SNIM) on VO_2. [24] This material undergoes a Metal-Insulator transition and the intensity gives a measure of the local insulating/metallic phase. A threshold intensity of 2.5 sets apart a metallic

from an insulating region (Fig. 1.6(g-l)). As shown in Ref. [23], the results are robust against setting a threshold within 15% of this value.

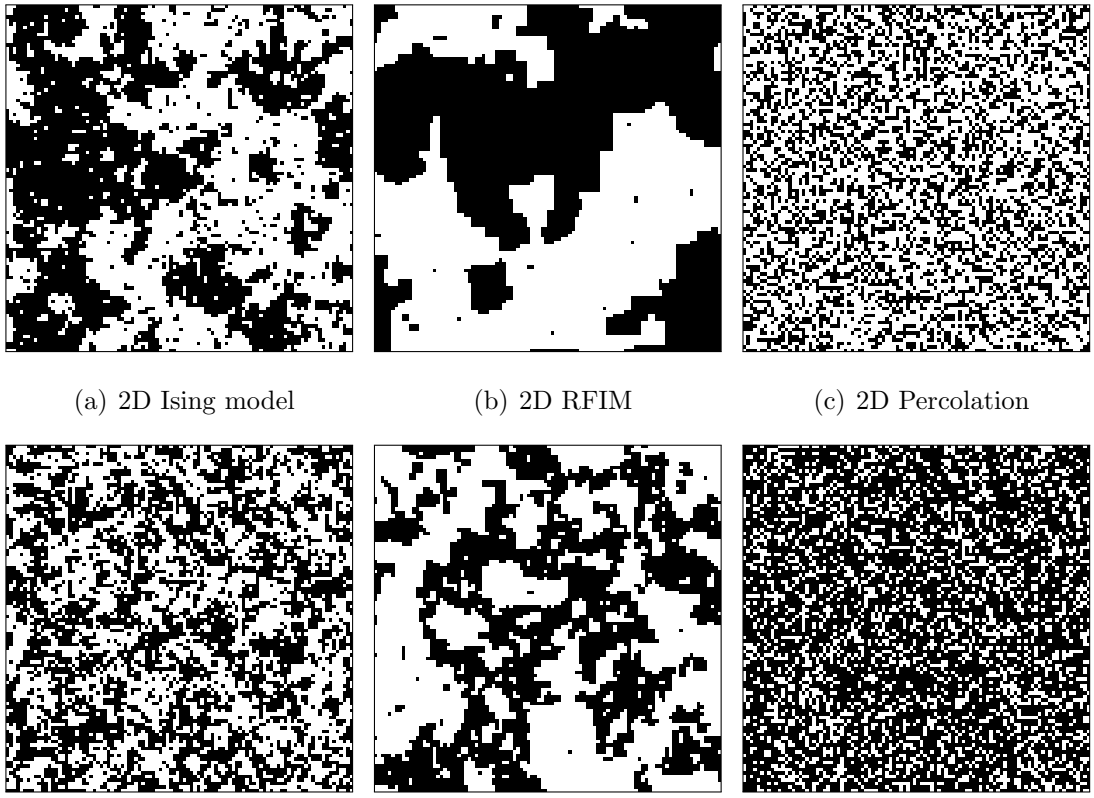

(a) 2D Ising model (b) 2D RFIM (c) 2D Percolation

(d) 3D Ising model (e) 3D RFIM (f) 3D Percolation

Figure 1.7. Critical configurations of different Ising models and percolation models.

Figure 1.7 demonstrates a few of the intricate patterns that form in various 2-state statistical models on a square/cubic lattice near criticality. Our goal is to categorize figures 1.6(g-l) based on the patterns that form in one of:

- 2D/3D clean Ising model
- 2D/3D random field Ising model (RFIM)
- 2D/3D uncorrelated percolation model

In chapter 4, we show the effectiveness of a deep learning framework keeping in mind the application to experiments. We show symmetry-based data reductions and out of sample space rejection criteria.

2. DISTINGUISHING XY FROM ISING ELECTRON NEMATICS

2.1 Introduction

The two-dimensional electron system/gas (2DES/2DEG) has intrigued the scientific community for quite some time due to the fascinating physical phenomena it exhibits. The Quantum Hall Effect (QHE) is one of the most interesting phenomena in 2DES (and otherwise) which demonstrates Landau quantization in the presence of a magnetic field. A 2DES/2DEG can be realized at a heterojunction of semiconductor materials such as in GaAs/AlGaAs, which is also the system being investigated in this study for data analysis.

Strong electron correlations can drive systems into a variety of novel electronic phases of matter. Electronic liquid crystals [25–27] form when electronic degrees of freedom partially break the symmetries of the host crystal. Like their molecular counterparts, electron nematic phases break rotational symmetry, while retaining liquidity. Such oriented electronic liquids have been observed in a variety of systems, including strontium ruthenates [28], iron superconductors [29–31], cuprate superconductors [32, 33], the (111) surface of bismuth [34, 35], and high fractional Landau levels. The key signature in the quantum Hall regime is a pronounced transport anisotropy that develops at low temperature [3, 36–39].

Through a comparison of simulations with experiments, we obtained an Ising universality class for the order parameter description of the electron nematic in GaAs/AlGaAs heterojunction. It is thus necessary to settle the question of which universality class it actually belongs to: Ising or XY. In order to address this question, we have proposed a test for determining the same. It applies to systems acquiring macroscopic nematic order at low temperatures.

2.2 Quantum Hall Effect

In this section, we give a pedagogical overview of the quantum Hall effect. [40]

The ordinary Hall effect was discovered by Edwin Hall in 1879. It is the phenomenon that produces a voltage difference across a conductor simultaneously perpendicular to an applied electric field and a magnetic field. This effect can be best understood when we study the motion of an electron in a crossed electric ($\vec{E}$) and magnetic field ($\vec{B}$) given by the Lorentz force ($\vec{F}$) equation:

$$\vec{F} = -e(\vec{E} + \vec{v} \times \vec{B}) \tag{2.1}$$

A free electron will perform cyclical motion in this configuration with a net drift velocity ($\vec{v}_{drift}$) perpendicular to both the electric field and magnetic field:

$$\vec{v}_{drift} = -\frac{\vec{E} \times \vec{B}}{B^2} \tag{2.2}$$

In a finite conductor, current flow is in the direction of the electric field, and in a steady state there cannot be any net motion of charge carriers in the direction perpendicular to it. Hence, there must be a charge buildup at the edges of the conductor which provides the necessary electric field required to compensate the initial $\vec{v}_{drift}$. This charge buildup produces a Hall voltage. For only electronic charge carriers, the Hall resistance (R_H) is:

$$R_H = -\frac{B}{n_e e} \tag{2.3}$$

where, n_e is the 2D carrier electron density.

A 2DEG/2DES in the presence of a perpendicular magnetic field and at a sufficiently low temperature produces quantized Hall resistance, which is an integer or rational factor of h/e^2.

$$\rho_{xy} = \begin{cases} \frac{1}{n}\frac{h}{e^2}, \ n \in \mathbb{Z}^+ & IQHE \\ \frac{1}{p/q}\frac{h}{e^2}, \ \{p, q\} \in \mathbb{Z}^+ & FQHE \end{cases} \tag{2.4}$$

The Integer Quantum Hall Effect (IQHE) is marked by the Hall resistance plateaus at integer factors, and the Fractional Quantum Hall Effect (FQHE) is marked by Hall resistance plateaus at rational fractions.

2.2.1 Landau quantization and Integer Quantum Hall Effect

The energy gets quantized upon application of strong magnetic field perpendicular to a 2DEG. The quantized energies are called Landau levels (LL). To see how the 2DEG is formed in a 3D system, let us begin with a 3D Hamiltonian:

$$H_{3D} = \frac{(\mathbf{p} + e\mathbf{A})^2}{2m_b} + e\Phi(x, y) + V(z) \tag{2.5}$$

where, $\mathbf{A}$ is the vector potential due to the magnetic field in the z-direction ($B\hat{z}$), $\mathbf{p}$ is the momentum operator, and m_b is the band mass of the electron. The dynamics in the z-direction are highly constrained because of the confining potential energy ($V(z)$), in other words, there is an energy gap between the two lowest energy states. The $\Phi(x, y)$ plays the role of the potential in the x-y plane which will be required in Sections 2.2.2 and 2.2.3 to understand quantized Hall resistance and longitudinal resistivity.

Since the magnetic field is in the z-direction, and $\mathbf{B} = \nabla \times \mathbf{A}$, without loss of generality we can set $A_z = 0$. Therefore, the Hamiltonian is:

$$H_{3D} = \Big[\frac{(p_x + eA_x)^2}{2m_b} + \frac{(p_y + eA_y)^2}{2m_b} + e\Phi(x, y)\Big]_{2D} + \Big[\frac{p_z^2}{2m_b} + V(z)\Big] \tag{2.6}$$

Hence, the Hamiltonian is separable in the z-direction. At low temperatures, the dynamics become quasi-2D as excitations in the wavefunction in the z-coordinate become thermally unfavorable.

As a result, the wavefunction in the z-direction decouples from the x and y directions:

$$H_{3D}|x, y, n_z\rangle = H_{3D}|x, y\rangle \otimes |n_z\rangle = (H_{2D} + \mathcal{E}_{n_z})|x, y\rangle \otimes |n_z\rangle \tag{2.7}$$

The exact quantization of $\mathcal{E}_{n_z}$ is given by the form of the confining potential energy in the z-direction, nonetheless $n_z = 0$ gives the ground state energy of the wavefunc-

tion in the z-coordinate which is relevant for the 2DEG. Now, the 2D Hamiltonian is:

$$H_{2D} = \frac{(\mathbf{p} + e\mathbf{A})^2}{2m_b} + e\Phi(x, y) \tag{2.8}$$

hereafter, the $\mathbf{p}$ and $\mathbf{A}$ are in the two-dimensional x-y plane only.

We make $\Phi(x, y) = 0$ as it is not relevant for the quantization of energy in a 2DEG ($\Phi(x, y) \neq 0$ will be used in Sections 2.2.2 and 2.2.3). The quantization follows after choosing an appropriate gauge. The two most used gauges are the symmetric gauge and the Landau gauge.

Symmetric gauge: This gauge preserves only the rotational symmetry of the system about the z-axis. The form of the vector potential is:

$$\mathbf{A}_S = B(-\frac{y}{2}, \frac{x}{2}) \tag{2.9}$$

Let's define the mechanical (pseudo) momenta operators ($\mathbf{\Pi}_\pm$), which is useful in the quantization of energy levels and hidden degeneracy of each energy level in this gauge.

$$\mathbf{\Pi}_\pm = \mathbf{p} \pm e\mathbf{A} \tag{2.10}$$

Now, the 2D Hamiltonian looks like:

$$H_{2D} = \frac{\mathbf{\Pi}_+ \cdot \mathbf{\Pi}_+}{2m_b} \tag{2.11}$$

To quantize this Hamiltonian we have to define new operators using Eqn. 2.10:

$$\begin{aligned} a_\pm &= \frac{l_b}{\sqrt{2}\hbar}(\Pi_{\pm,x} - i\Pi_{\pm,y}) \\ a_\pm^\dagger &= \frac{l_b}{\sqrt{2}\hbar}(\Pi_{\pm,x} + i\Pi_{\pm,y}) \end{aligned} \tag{2.12}$$

where, $l_B = \sqrt{\hbar/eB}$ is the magnetic length. Their commutation relations are:

$$\begin{aligned} &[a_\pm^\dagger, a_\pm] = 1, && [a_\pm, a_\pm] = [a_\pm^\dagger, a_\pm^\dagger] = 0 \\ &[a_\pm^\dagger, a_\mp] = 0, && [a_\pm, a_\mp] = [a_\pm^\dagger, a_\mp^\dagger] = 0 \end{aligned} \tag{2.13}$$

Using these operator relations and with a little bit of algebra the Hamiltonian can be simplified to:

$$H_{2D} = \hbar\omega_c\big(a_+^\dagger a_+ + \frac{1}{2}\big) \tag{2.14}$$

where, ω_c is the cyclotron frequency given by $\hbar/(m_b l_B^2)$. The energy spectrum takes the harmonic oscillator form :

$$\mathcal{E}_{n_+,n_-} = \hbar\omega_c\big(n_+ + \frac{1}{2}\big) \tag{2.15}$$

where, $n_\pm = a_\pm^\dagger a_\pm$ are number operators. $n_- \in 0, 1, 2...$ gives the degeneracy of each Landau level ($n_+ \in 0, 1, 2...$).

Excitations in the Landau levels are given by:

$$|n_+, n_-\rangle = \frac{(a_+^\dagger)^{n_+}(a_-^\dagger)^{n_-}}{\sqrt{n_+! n_-!}}|0, 0\rangle \tag{2.16}$$

where, n_- gives the degeneracy of each LL n_+. Each LL should ideally be infinitely degenerate, but it is restricted by the number of magnetic flux quanta ($n_B = eB/h$) threading the finite area of the sample surface, as a result giving the filling factor $\nu = n_e/n_B$

The choice of gauge depends on the geometry of the sample. The Landau gauge is most suitable for the upcoming discussion.

Landau gauge: This gauge preserves the translational symmetry of the system in only one of the directions.

$$\mathbf{A}_L = B(-y, 0) \tag{2.17}$$

In this gauge example the vector potential has translation symmetry in the x-direction only. With this choice of vector potential the wavefunction in the x-direction will be a plane wave solution ($e^{ik_x x}$) and now the Hamiltonian is:

$$H_{2D} = \frac{m_b\omega_c^2}{2}(y - k_x l_B^2)^2 + \frac{p_y^2}{2m_b} \tag{2.18}$$

This is a shifted harmonic oscillator Hamltonian. The wavefuntion in the y-direction will be that of a shifted harmonic oscillator for each k_x.

$$\begin{aligned}\langle x, y|n_x, n_y\rangle &= \langle x, y|k_x = n_x(2\pi/L_x), n_y\rangle \\ &\sim e^{ik_x x}\mathcal{H}_{n_y}(y - k_x l_B^2)e^{-(y-k_x l_B^2)^2/2l_B^2}\end{aligned} \tag{2.19}$$

where, $k_x = n_x(2\pi/L_x)$ with periodic boundary condition. $\mathcal{H}_n$ is the Hermite polynomial of n^{th} order. And there is a shift of $k_x l_B^2$ in the wavefunction in y-direction.

The energy takes the harmonic oscillator form :

$$\mathcal{E}_{n_x,n_y} = \hbar\omega_c(n_y + \frac{1}{2}) \tag{2.20}$$

where, $n_x \in 0, 1, 2...$ gives the degeneracy of the harmonic oscillator in each $n_y \in 0, 1, 2...$ harmonic oscillator energy level, which is the LL index in this case.

The potential landscape in the x-y plane is due to the impurity potential ($\Phi_{conf}(y)$) as well as the confining potential ($\Phi_{imp}(x, y)$), (Fig. 3.1 of Ref. [40])

$$\Phi(x, y) = \Phi_{conf}(y) + \Phi_{imp}(x, y) \tag{2.21}$$

here the confining potential is taken in the y-direction as we will be looking at transport in x-direction, hence relevant for this particular choice of Landau gauge. The Hamiltonian in the presence of this confinement potential still possesses the translational symmetry in the x-direction.

To first order in the Taylor expansion, the confinement potential near y_0 is:

$$\Phi_{conf}(y) \simeq \Phi_{conf}(y_0) - E_{conf}(y_0) \cdot (y - y_0) + \mathcal{O}\big(\frac{\partial^2 \Phi_{conf}}{\partial y^2}\big) \tag{2.22}$$

where, $E_{conf}(y_0)$ is the electric field in the y direction at y_0. Putting this back in Eqn. 2.8 and using Eqn. 2.18 neglecting second order terms in $\Phi_{conf}(y_0)$, the Hamiltonian becomes:

$$H_{2D} = \frac{p_y^2}{2m_b} + \frac{m_b\omega_c^2}{2}(y - (y_0 + \frac{eE_{conf}}{m_b\omega_c^2}))^2 + e\Phi_{conf}(y_0) \tag{2.23}$$

and the energy spectrum becomes,

$$\mathcal{E}_{n_x,n_y} = \hbar\omega_c\big(n_y + \frac{1}{2}\big) + e\Phi_{conf}(n_x(2\pi/L_x)l_B^2) \tag{2.24}$$

2.2.2 Localized states

Localized states form near a peak or a valley of the impurity potential. In Fig. 3.1 of Ref. [40], the valleys and peaks are marked by $(-)$ and $(+)$, respectively. Localized

states are formed away from the edges of the 2DEG. The insulating nature of these states are due to the formation of closed orbits around peaks and valleys.

2.2.3 Extended states

Extended states are responsible for the conduction of electrons and the reason behind non-zero resistivity. They extend over the whole sample in x/y-direction.

Current in the n_y^{th} Landau level is given by:

$$\begin{aligned} I^x_{n_y} &= -\frac{e}{L_x}\sum_{k_x}\langle n_y, k_x|v_x|n_y, k_x\rangle \\ &= -\frac{e}{\hbar L_x}\sum_{n_x}\frac{\Delta\mathcal{E}_{n_x,n_y}}{\Delta(n_x 2\pi/L_x)} \\ &= -\frac{e}{\hbar L_x}\sum_{n_x}\frac{L_x}{2\pi}(\mathcal{E}_{n_x+1,n_y}-\mathcal{E}_{n_x,n_y}) \\ &= -\frac{e}{h}(\mu_{max}-\mu_{min}) = \frac{e^2}{h}V \end{aligned} \tag{2.25}$$

Therefore, each Landau level contributes to a single quantum of conductance. Hence the total conductance for n_y completely filled LLs:

$$G = \sum_{n'=0}^{n_y-1} G_{n'} = n_y\frac{e^2}{h} \tag{2.26}$$

where this is an example of quantum transport given by the Landauer-Büttiker formula [41]:

$$G_n = \frac{e^2}{h}T_n \tag{2.27}$$

where, T_n is the transmissin coefficient for the n^{th} quantum channel and it is related to the reflection coefficient (R_n) by $T_n + R_n = 1$.

Edge states

The edge states have the property of dissipationless transmission of current along the equipotentials near the edges, which are at a higher potential than the bulk, creating an effective electric force away from the edges. (Fig. 3.1 of Ref. [40]) These

states are chiral in nature, i.e. their net motion (Hall drift) is only along the positive or negative x-direction depending on which edge (upper edge and lower edge, respectively) they are close to. The chirality is the same for all edge states near the same edge, hence there is no backscattering. From Eqn. 2.27, we can see that $T_n = 1$ and $R_n = 0$ for each fully filled LL. Hence current can pass through it without any resistance away from half-filling and we get the Hall resistance for the IQHE:

$$R_{XY} = G^{-1} = \frac{1}{n}\frac{h}{e^2} \tag{2.28}$$

Bulk states

Near half-filling, bulk states are extended nearly over the whole area of the 2DEG (Fig. 3.5 of Ref. [40]). The highest partially filled LL contributes to the reflection coefficient $R_n \neq 0$ which contributes to the longitudinal resistance.

These states help in backscattering when the n_y^{th} Landau level is half full and the potential valleys are filled up. The Fermi energy traces out equipotentials which are spread throughout the system, which makes the bulk states extend throughout the material and effectively connecting the edge modes. So, an electron scattered onto an extended bulk state from one of the chiral edge states can travel to the opposite edge and therefore backscattered. This contributes to the longitudinal resistance near half-filling by connecting edge states and helping to backscatter. (Refer to Fig. 3.5 of Ref. [40])

Please note that the above discussion is possible in a Landau gauge ($\mathbf{A}'_L = B(0, x)$) and confining potential ($\Phi_{conf}(x)$), which keeps the Hamiltonian translationally invariant in the y-direction, where x and y can be interchanged so as to come to the same conclusion about resistance in the y-direction, *i.e.* ρ_{xx} and ρ_{yy} will not be different, even if the sample is not a square, according to this discussion and both should have a peak near half-filling.

2.3 The Nematic phase

We first give a pedagogical introduction to nematics [42], followed by our simulation results.

A liquid crystal phase that favors a particular direction or orientation without having any order in position is called a nematic. The relevant physics of an electron nematic phase can be understood from the symmetry of the phase. A Landau theory which obeys the symmetries of the nematic phase cannot retain odd-ordered term, since they are not invariant under reflection or 180^o rotation. Hence a Landau theory for the nematic only admits even-ordered invariants in the absence of an applied field. Whether a nematic-to-isotropic transition is discontinuous or continuous is determined by the symmetry of the order parameter.

As mentioned in Section 1.1, we are interested in half-integral filling in quantum Hall systems, where transport, i.e. the longitudinal resistivity, becomes anisotropic. Our description assumes the formation of nematogens which are small domains of stripes with alternately filled and empty $(m+1)^{th}$ Landau Level, averaged to give filling fraction $\nu = m + 1/2$. The nematic director, in this case, is given by the stripe orientation of a nematogen.

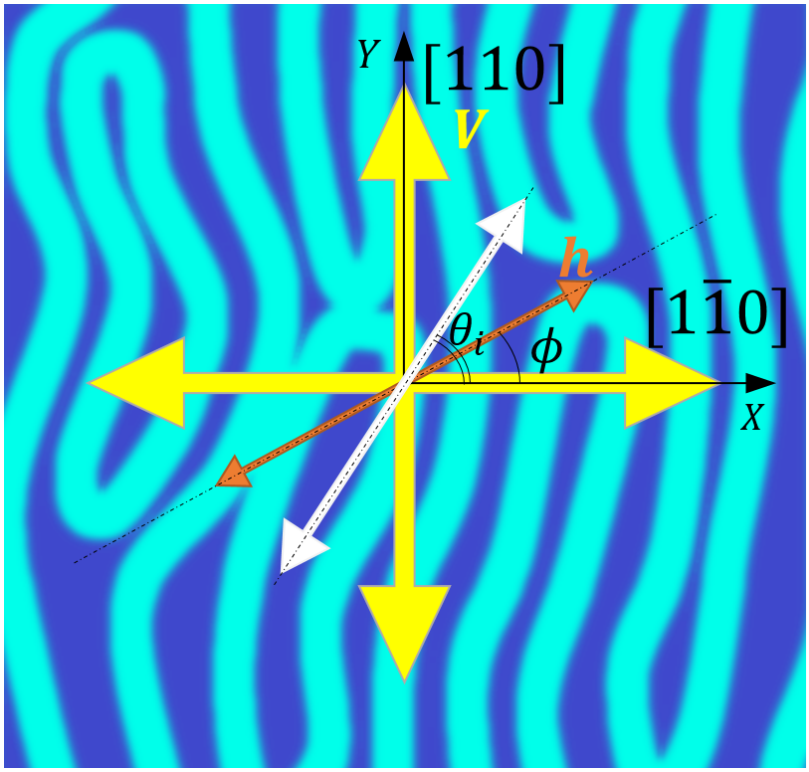

Figure 2.1. The four yellow arrows represent the orientations in which the crystal field term (V) is maximum. The orange double headed arrow gives the orientation of the h-field with respect to the crystal field. The gray double arrow gives the nematic orientation (θ) at a lattice position denoted by i. The longitudinal resistivities ρ_{xx} and ρ_{yy} are typically measured along the crystallographic directions [1$\bar{1}$0] and [110], respectively. Schematic of a barely melted stripes, of alternating filling fraction $\nu = m$ (cyan) and $m + 1$ (blue), which usually forms in the [110] direction for $m = 4$, hence becoming the easy axis of transport in the $\nu = m + \frac{1}{2}$ state.

A nematic director ($\hat{\eta}^\alpha$) has the property of pointing parallel or antiparallel to any given direction, hence both $\hat{\eta}^\alpha$ and $-\hat{\eta}^\alpha$ contribute equally to the nematic order. A second rank tensor representation is sufficient for its description. Also a high temperature isotropic phase is requires the nematic order to yield zero when averaged

over directions. This leads us to the nematic order parameter defined as a symmetric traceless tensor [42]:

$$\mathcal{Q}_{ij} = \frac{A}{N}\sum_{\alpha}(\eta_i^{\alpha}\eta_j^{\alpha} - \frac{1}{2}\delta_{ij})\delta(\vec{r} - \vec{r}^{\alpha}) \tag{2.29}$$

where, A/N makes the quantity dimensionless. When it is averaged over the positions of the lattice the nematic order parameter in a two-dimensional system:

$$\langle\mathcal{Q}_{ij}\rangle = \mathcal{N}(n_i n_j - \frac{1}{2}\delta_{ij}) \tag{2.30}$$

where, $\hat{n}$ is the unit vector along the principle axis, which is also called the Frank director. We take the x-axis as our principle crystalline axis, and with the help of Eqn. 2.30 and Eqn. 2.29 we get:

$$\begin{aligned}\mathcal{N} &= \langle(2(\hat{\eta}^{\alpha}\cdot\hat{n})^2 - 1)\rangle \\ &= \langle(2\cos^2\theta^{\alpha} - 1)\rangle = \langle\cos(2\theta^{\alpha})\rangle\end{aligned} \tag{2.31}$$

where θ^{α} is the angle between the principle axis ($\hat{n}$) and the nematic director ($\hat{\eta}^{\alpha}$) at position $\vec{r}^{\alpha}$.

Therefore the nematic order parameter is completely determined by the angle the nematic director makes with the principle crystalline axis. This closely resembles an XY spin and is symmetric under π rotation, which is expected as the director should not have a net direction but an orientation.

For a nematic which breaks the $U(1)$ symmetry [26,32,43,44] into a C_4 symmetry with its principle axis along x-direction, the order parameter is given by:

$$\mathcal{N} \propto \frac{\rho_{xx} - \rho_{yy}}{\rho_{xx} + \rho_{yy}} \tag{2.32}$$

This is an example of how the nematic order can be related to transport anisotropy. In a 2DEG with near half-filled LL, with $N \geq 2$, the anisotropic resistivity in x and y-direction is characteristic of a nematic phase. Hartree-Fock calculations were carried out by Koulakov et al. [4,45], and Moessner and Chalker [46] show that unidirectional stripe order charge density wave ground states form because of softening of Coulomb

interactions at the nodes of the electronic wavefunction in excited LL. Hence, at $\nu = 9/2$, the system phase separates into a $\nu = 4$ and a $\nu = 5$. They predicted a CDW wavelength of the order of the classical cyclotron radius of $\sim$ 100nm for half-integer filling of LL $N \geq 2$, which matches with experiments. At lower filling, for LL $N < 2$ the CDW order may be destroyed by quantum fluctuations.

A nematic can form by partial melting of a solid, i.e. a stripe or a smectic, restoring translation symmetry, but not orientation symmetry [36]. Thermal and quantum fluctuations can lead to a stripe-nematic phase transition in a quantum Hall system and the thermal phase transition is well studied in Ref. [26]. A nematic can also form from a thermal/quantum melting of a frustrated quantum antiferromagnet. From a Fermi-liquid perspective, where the Fermi surface reflects the underlying symmetry of the system, a nematic phase can form due to a Pomeranchuk instability of the Fermi surface. Hence, in a 2DES, a Pomeranchuk instability induces a nematic quantum phase transition by distorting a circular Fermi surface to an ellipse due to quadrupolar effects [38, 47].

In the following sections, we study some of the lattice models which can describe nematic order. Lattice models are useful for simulations.

2.3.1 2D XY Nematic

The nematic order parameter is a headless vector, which depends on orientation but not the direction. It is symmetric under a π rotation. Using the nematic order parameter formulated in Eqn. 2.31, the Hamiltonian for an XY nematic with nearest neighbor coupling and an explicit symmetry breaking field is defined as:

$$H_{XY} = -J \sum_{\langle i,j \rangle} \cos\left(2(\theta_i - \theta_j)\right) - h \sum_i \cos\left(2(\theta_i - \phi)\right) \tag{2.33}$$

where, J is the tendency of neighboring sites to align their orientation, h is the symmetry breaking field, and θ is orientation of the nematic order. The h-field sets the preferred orientation of the nematic to be along $\theta = \phi \pmod{\pi}$, hence the two-fold symmetry of the h-field term is apparent.

2.3.2 2D XY Nematic with four-fold symmetry breaking field

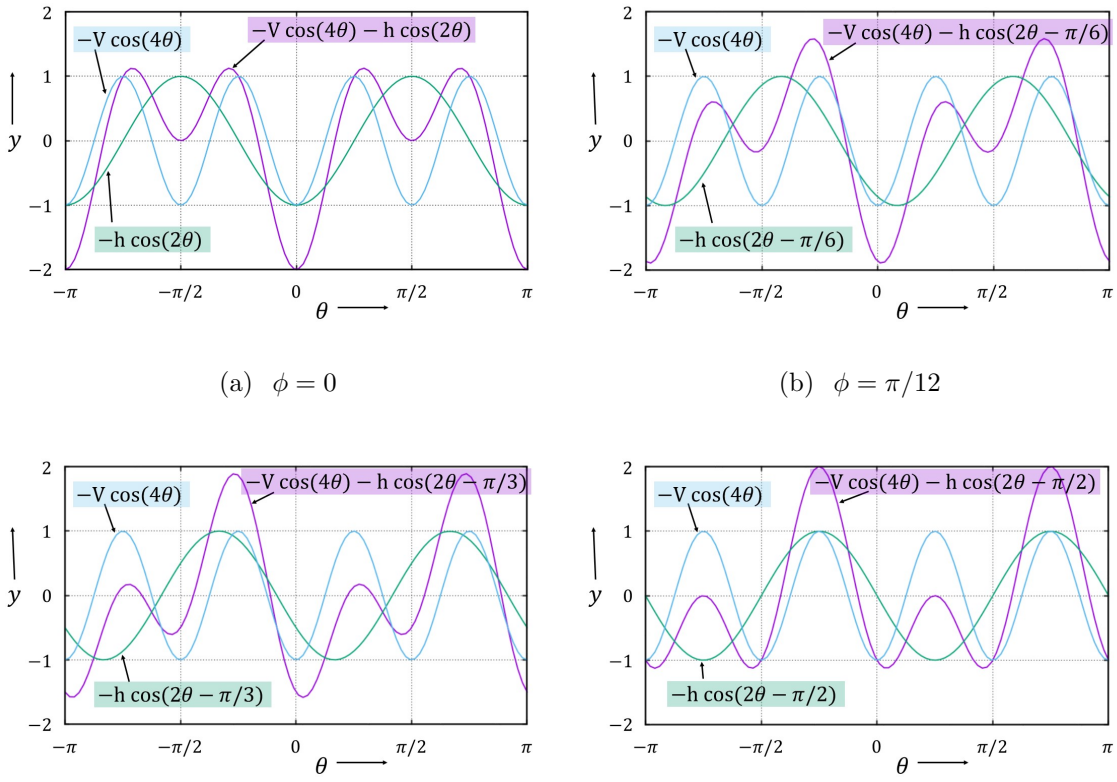

(a) $\phi = 0$ (b) $\phi = \pi/12$

(c) $\phi = \pi/6$ (d) $\phi = \pi/4$

Figure 2.2. Plot of a single site potential energy as a function of θ. The h-term with different ϕ ((a)-(d)) is plotted in green, the V-term is plotted in blue and the total site energy (V-term+h-term) is plotted in purple. (a) The difference between the 2 distinct potential minima is largest; (d) All the potential minima are at same energy.

In the presence of a four-fold symmetry breaking field which can arise due to crystalline lattice effects or otherwise, the Hamiltonian of this "modified XY nematic", using Eqn. 2.33 is given by:

$$H_{XY-V} = H_{XY} - V \sum_i \cos\left(4\theta_i\right) \tag{2.34}$$

where, V is the strength of the four-fold symmetry breaking field. In the absence of a two-fold symmetry breaking field (h), V sets the preferred orientation along $\theta = 0 \pmod{\pi/2}$, hence the four-fold symmetry of the V-term is evident in the absence of an h-field. Also, if the h-field points along one of the symmetry axes of the four-fold V, then the four-fold symmetry is broken down to two-fold symmetry.

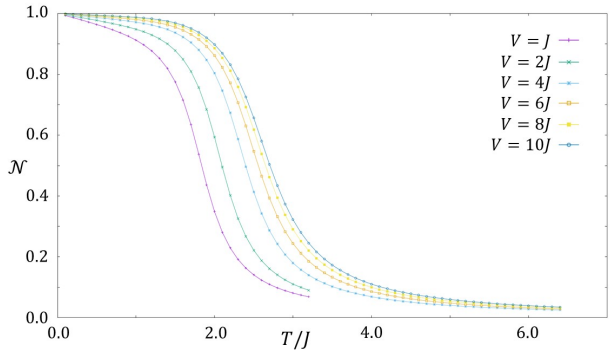

(a) Varying V in XY-V model with $h = 0.15J$ and $\phi = 0$.

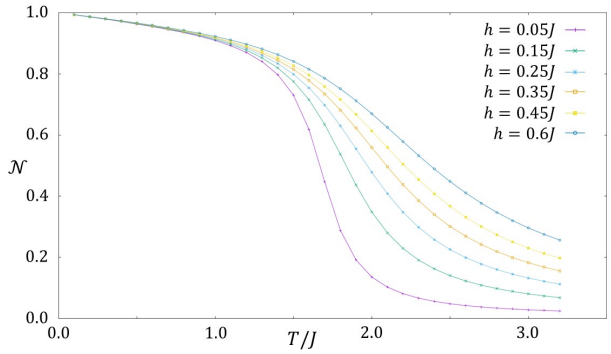

(b) Varying h in XY-V model with $\phi = 0$ and $V = J$.

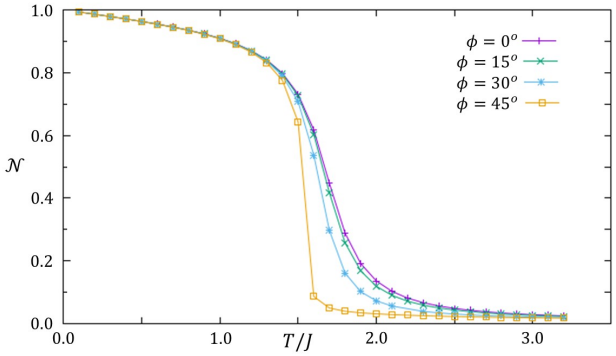

(c) Varying ϕ in XY-V model with $h = 0.05J$ and $V = J$.

Refer to Fig. 2.2 for details.

Figure 2.3. Simulation of the modified XY model with 4-fold symmetry breaking term given in Eqn. 2.34.

Our simulations (Fig. 2.3(a)) show the effect of increasing V. They show that the low-temperature phase becomes more gradual, as a function of temperature for a larger V. The $V \to \infty$ limit will be a flat curve near $T = 0$ which is the Ising case. Here we can observe the shift in the transition temperature T^*_{XY-V} towards the Ising transition temperature T^*_{Ising}. Fig. 2.3(b) shows the dependence on h, which show that the transition becomes more gradual, as a function of temperature, as h is increased, and the T^*_{XY-V} increases.

The effect of rotating the uniform orienting field h away from a crystalline axis is explored in Fig. 2.3(c), where the angle ϕ between h and the crystalline axes is varied. Note that up until $\phi \approx \pi/6$ the impact on the temperature evolution is negligible. However, at the high symmetry point $\phi = \pi/4$, there is a true symmetry breaking transition, and the temperature onset is quite sudden. This symmetry arises due to the degeneracy of the on-site potential at two different θ's (mod π) for $\phi = \pi/4$ (Fig. 2.2).

2.3.3 Ising Nematic

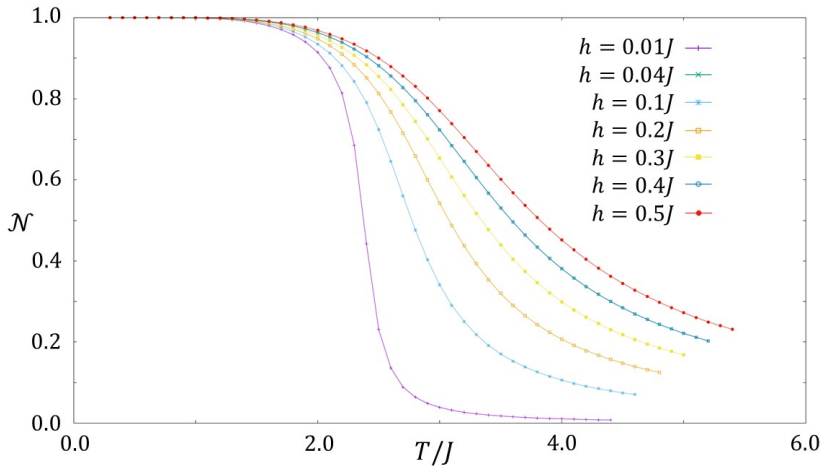

Figure 2.4. Simulation of an Ising model on 100×100 lattice, where we vary the h with $\sigma_\phi = +1$, Eqn. 2.36

A two-dimensional Ising nematic is same as the Ising model with the mapping of:

$$\begin{aligned} \sigma = +1 &\leftrightarrow \theta = 0 \ (\text{mod } \pi) \\ \sigma = -1 &\leftrightarrow \theta = \frac{\pi}{2} \ (\text{mod } \pi) \end{aligned} \tag{2.35}$$

The Hamiltonian of the Ising nematic is a special case of the modified XY nematic (Eqn. 2.34), where $V \to \infty$. This can be seen with a slight modification of Eqn. 2.34, where the last term is replaced by $-V \sum_i (\cos(4\theta_i) - 1)$. This removes the $-\infty$ from the lowest energy configurations of the on-site potential due to $V \to \infty$. Now, the finite energy configurations of this model is given by $\theta = 0 \ (\text{mod } \pi)$ and $\pi/2 \ (\text{mod } \pi)$, which corresponds to the Ising nematic configuration. The Ising Hamiltonian is given by:

$$H_{Ising} = -J \sum_{\langle i,j \rangle} \sigma_i . \sigma_j - h \sum_i \sigma_i . \sigma_\phi \tag{2.36}$$

where, $\sigma_\phi = \cos(2\phi)$ is dependent on the value of ϕ. J and h holds the usual nearest neighbor interaction and on-site two-fold symmetry breaking potential, respectively.

The effect of h-field on the order parameter as a function of temperature is shown in Fig. 2.4. It shows the same effect as that of Fig. 2.3(b), i.e. the transition becomes gradual and the onset temperature of order (T^*_{Ising}) shifts towards higher temperatures.

2.4 Hysteresis

A phenomenon in which a system remembers the previous state of the system, where the system lags the conditions. In the present context of lattice models the hysteresis at $0 < T < T_c$ is governed by the existence of a spontaneously broken symmetry phase with no external symmetry breaking field present.

2.4.1 2D XY universality class

The *Mermin-Wagner Theorem* states that continuous symmetry cannot be spontaneously broken at finite temperatures in systems with sufficiently short-range interactions in dimensions $d \leq 2$. As a result the XY model, which is a special case, cannot spontaneously break the continuous $U(1)$ (circular) symmetry of the model in a $d \leq 2$ dimensional lattice. Hence the XY model does not undergo a second-order phase transition at any finite non-zero temperature with its spontaneous magnetization vanishing for all temperatures. Although there is no second-order phase transition, the model has a transition from a quasi-ordered phase to an isotropic phase. Spin-spin correlation function decays exponentially at high temperatures but at low enough temperatures decays as a power law (quasi-long range order). This low temperature bound vortex-antivortex phase (quasi-ordered) to an unpaired vortex and antivortex phase above a critical temperature ($T_{KT} = 0.89J$ in the square lattice XY model with nearest-neighbor coupling strength J) is known as a *Kosterlitz-Thouless*

(KT) transition. Hence the XY model is in Berezinskii-Kosterliz-Thouless (BKT) universality class.

Another way to see why the low-temperature phase does not show any spontaneous magnetization is in the following manner. There is an infinite degeneracy of the ground state which are connected in a continuous manner. A fluctuation in the transverse direction to the magnetization is massless, which implies that it comes about with no energy cost. These fluctuations (which are related to the transverse susceptibility) are *Nambu-Goldstone* modes of broken continuous symmetry which destroy the ordered phase because they logarithmically diverge with system size.

In the presence of an explicit symmetry breaking field the system develops a finite order parameter below a transition temperature T^*_{XY}. The critical exponent δ gives the power-law dependence of the magnetization M with the magnetic field h: $M(h) \sim h^{1/\delta}$.

2.4.2 2D Ising universality class

The square lattice Ising model was exactly solved analytically by Lars Onsager for $h = 0$ [48]. The spontaneous magnetization at $T \leq T_c$ is given by:

$$M(T, h = 0) = \left[1 - \sin^{-4}\left(\frac{2J}{T}\right)\right]^{1/8}, \; T < T_c \tag{2.37}$$

This model has a spontaneously broken symmetry phase which exist below $T < T_c = 2.27J$. An applied magnetic field ($h \neq 0$) moderates the abrupt transition near T_c and also elevates T^*_{Ising}.

A moderate two-fold symmetric field in an XY model, which is the same as a four-fold symmetric field (V) of the XY nematic, makes the nature of the transition Ising like. Hence the modified XY model (nematic) is in the Ising model (nematic) universality class.

At a finite field h and at a temperature below the transition temperature T^* there is a developed order parameter for both the Ising and the XY model. As h is reduced to zero the order of the phase will be determined by the spontaneously

broken symmetry phase. Since the Ising case has spontaneously broken symmetry, the magnetization in the absence of applied field will be determined by its previous state, i.e. the sign of the h, and the strength of the coercive field h_c required to reverse the magnetization depends on the temperature; whereas in the XY case the magnetization goes to zero as $h^{1/\delta}$, hence requiring no coercive field to change the magnetization. Therefore, it is evident that the XY model is more susceptible to changes in h $(0 < T < T_c)$ than the Ising model, hence hysteresis is demonstrated in the Ising universality class but not in the XY universality class.

2.5 Dependence of resistivity anisotropy on Temperature

As mentioned in the section 2.3, the nematic phase gives rise to anisotropic transport properties at a macroscopic scale. The longitudinal resistivity becomes anisotropic with decreasing temperature. The resistivity increases in the direction perpendicular to the stripes, if we assume the formation of stripes with alternating filling fraction m and m+1. The anisotropy is only seen in half-filled LL $N \geq 2$, which implies a half-integer filling fraction of $\nu \geq 9/2$, this corroborates with the prediction of CDW states by Koulakov et al. [4, 45], and Moessner and Chalker [46]. The formation of stripes along one of the principle axes helps us to understand the low resistivity along the stripe axis, where current can be propagated in an almost dissipationless manner by the edge states whereas the conductance in the transverse direction is hindered due to traversal across alternately filled Landau levels.

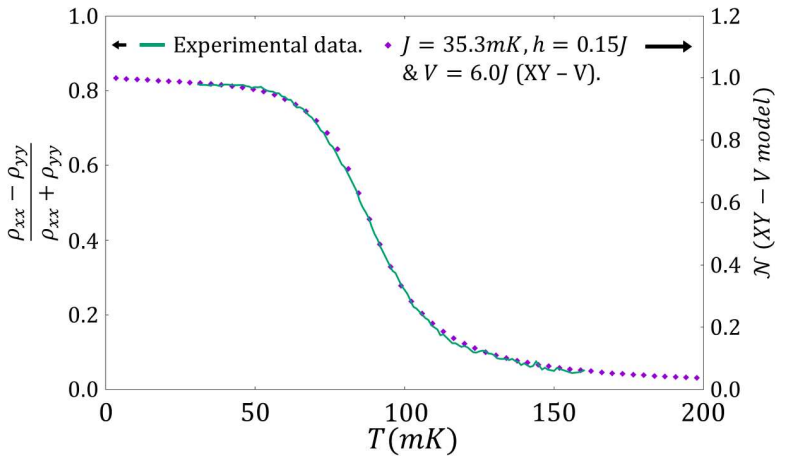

(a) XY model with moderate 4-fold symmetry breaking term V, Eqn. 2.34

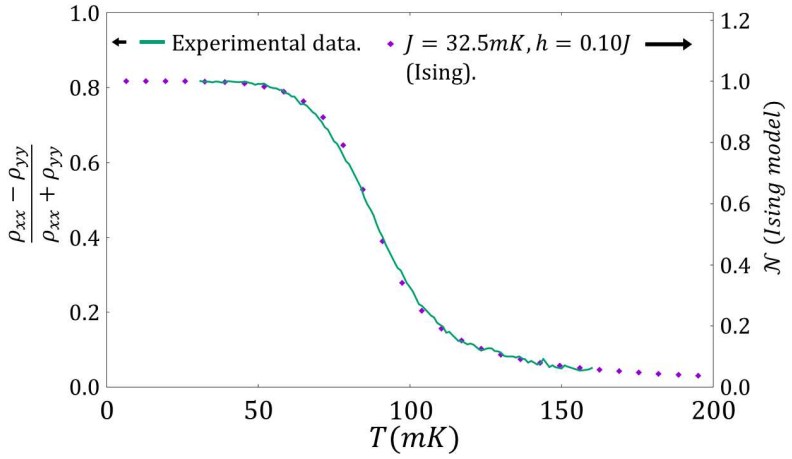

(b) Ising Model, Eqn. 2.36

Figure 2.5. Monte Carlo simulations (purple dots) on a lattice of 100x100 sites, compared to experimental data (green line) of resistivity anisotropy $\frac{\rho_{xx}-\rho_{yy}}{\rho_{xx}+\rho_{yy}}$ from Lilly *et al.* [3]. The theoretical comparison is to: (a) the Ising model with a uniform orienting field h, and (b) the XY model with a moderate four-fold symmetry breaking field V and uniform orienting field h. Note that within an XY description, a moderate 4-fold symmetry breaking term $V \neq 0$ is required to capture the low-temperature dependence of the resistivity anisotropy, which changes the universality class of the electron nematic from XY to Ising. The resistivity anisotropy $\frac{\rho_{xx}-\rho_{yy}}{\rho_{xx}+\rho_{yy}}$ is from the experimental data of Lilly *et al.* [3].

2.5.1 A comparison with XY model with four-fold symmetry breaking term

The effect of V on the universality class of the pure XY model is that as the V field becomes stronger, the transition temperature changes from $0.89J$ towards $2.27J$. Our simulations are done with very large V which shift the T_c near the Ising universality class. Fig. 2.5(a) shows how the resistivity anisotropy data of Lilly et al. [3] compares with this classical model.

The "nematicity" (order parameter of the nematic) in this model is $\mathcal{N} = \left\langle e^{2i\theta} \right\rangle$ [5]. Because the (normalized) macroscopic transport anisotropy ρ_a transforms under rotations in the same way as the nematicity, the two are related as $\rho_a \equiv \left[(r+1)/(r-1)\right]\left(\rho_{xx} - \rho_{yy}\right)/\left(\rho_{xx} + \rho_{yy}\right) = f(\mathcal{N})$ where $f(\mathcal{N})$ is an odd function of $\mathcal{N}$, and $r \equiv \rho_{xx}(\mathcal{N} \to 1)/\rho_{yy}(\mathcal{N} \to 1)$ is what the ratio of macroscopic resistivities would be in a fully oriented state. For small $\mathcal{N}$, $f(\mathcal{N}) = \mathcal{N}$ [5, 43].

We find that the entire temperature evolution can be captured in the presence of both nonzero h and nonzero V, as shown in Fig. 2.5(a) [49]. In the Figure, we use uniform orientational field $h = .15J$ along with four-fold symmetry breaking term $V = 6J$, and $J = 35.3$mK. Smaller values of V have too steep of a slope at low temperatures. For larger values of V, the higher temperature behavior $(100-150$mK$)$ can no longer be captured. For the parameters of Fig. 2.5(a), the absolute strength of the interaction J is about half that of Ref. [5]. Because the value of V that we use is not small with respect to J, the universality class of the transition is now Ising, not XY. For a pure XY model with $h = 0$ and $V = 0$, the transition temperature is $T_{\mathrm{KT}} = .89J$ [8], but in Fig. 2.5(a) the onset of nematicity is happening closer to the (2D) Ising transition temperature of $T_c = 2.27J$, consistent with this shift of universality class [49].

2.5.2 A comparison with Ising model

Our comparison of the experimental resistivity anisotropy to an Ising model is shown in Fig. 2.5(b) [49]. We find that the data can be well described throughout the entire temperature range within a simple Ising model, with $J = 32.5mK$ and $h = 0.1J$.

The nematic order parameter in this case is $\mathcal{N} = (1/N)\sum_i \sigma_i$. As in the case of an XY model of an electron nematic, the (normalized) macroscopic resistivity anisotropy ρ_a maps to the macroscopic order parameter in the Ising description as $\rho_a = g(\mathcal{N})$ where $g(\mathcal{N})$ is an odd function of $\mathcal{N}$ and to first order in $\mathcal{N}$, $g = f$.

Remarkably, we find that the entire temperature range of the resistivity anisotropy ρ_a can be captured quite well within an Ising model in the presence of a weak uniform orienting field. Within this context, the low temperature saturation of $\big(\rho_{xx} - \rho_{yy}\big)/\big(\rho_{xx} + \rho_{yy}\big)$ to a value $\approx .818 \neq 1$ could have several origins [5, 43]: (i) Taken at face value, the saturation implies that the bare "nematogens" represented by each Ising variable have an intrinsic resistivity anisotropy which persists down to the lowest temperatures, $r = \rho_{xx}/\rho_{yy} \approx 10$. This could be attributable to quantum fluctuations within a bare nematogen. (ii) Similar saturation effects could also arise from even a small amount of quenched disorder, since the critical (random field type) disorder strength is zero in a two-dimensional Ising model. (iii) Nonlinear terms in the function $g(\mathcal{N})$ can lead to $g \neq 1$ as $\mathcal{N} \to 1$ at low temperature.

The conclusion from these comparisons is that both the models support the presence of a two-fold symmetry breaking field and there is a large four-fold crystalline field in play that effectively makes this transition Ising like.

2.6 Symmetry breakers

The circular symmetry of a free 2DEG can be broken by the point group symmetry of the lattice. The four-fold symmetry of the host crystal or piezoelectricity of GaAs can break the circular symmetry. Whereas the two-fold symmetry is not

apparent at the heterojunction since a $\pi/2$ rotation is not one of the valid symmetry operations. The symmetry-breaking mechanism from four-fold to two-fold is not well understood and a matter of ongoing research. The search for the intrinsic two-fold symmetry breaking mechanism behind the easy axis of conduction has been inconclusive. Experimentally there have been discoveries of external factors that can control the transport axis for easy conduction. This has also led to the development of some theoretical understandings based on these factors.

2.6.1 In-plane magnetic field

An in-plane magnetic field ($B_{\parallel}$) can switch the symmetry directions and the dependence on it is not linear. In a weak in-plane magnetic field, the easy axis is oriented perpendicular to the field (Fig. 2.6) [50,51]. However, a strong in-plane magnetic field can switch it back to stripes parallel to the applied in-plane field as observed by Shi et al. [52].

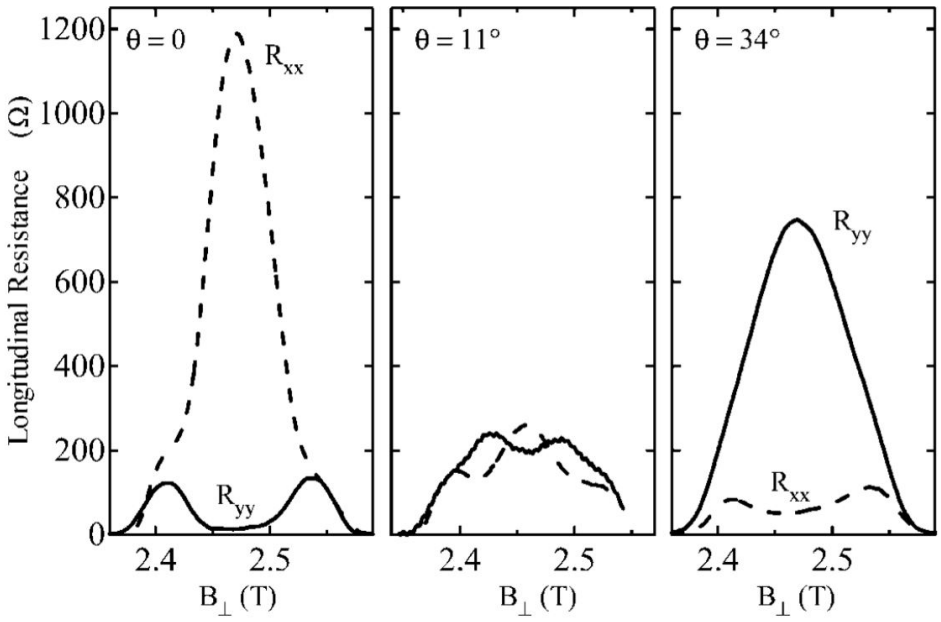

Figure 2.6. Reprinted figure 2 with permission from [(Ref. [50]) M. P. Lilly, K. B. Cooper, J. P. Eisenstein, L. N. Pfeiffer, and K. W. West. Phys. Rev. Lett. 83, 824, 1999.] Copyright (2020) by the American Physical Society. Switching of easy transport axis with applied in-plane magnetic field.

2.6.2 Uniaxial strain

It was observed experimentally that an external strain can switch the easy axis direction in a two-dimensional hole gas (2DHG) [53]. A theoretical description was also devised based on spin-orbit interaction. According to this theoretical description, at zero strain, both crystalline axes were equivalent and shear strain (internal or external) could break the symmetry between the two axes of the 2DHG/2DEG. Experimental data from Ref. [53] is shown in Fig. 2.7.

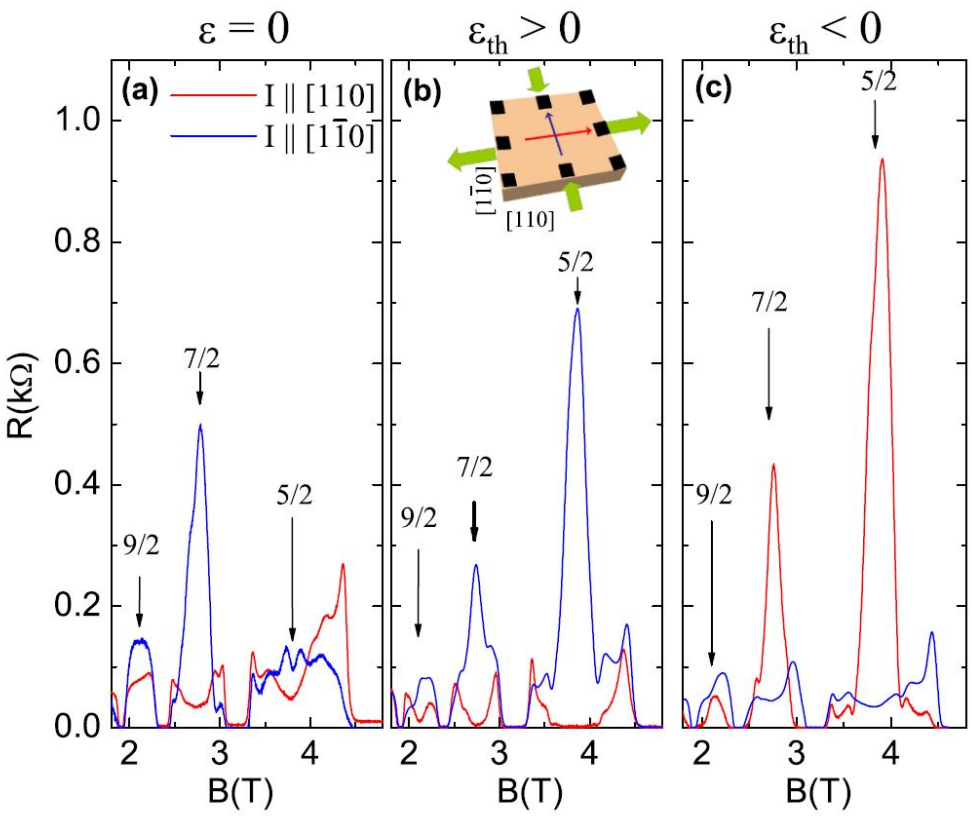

Figure 2.7. Reprinted figure 1 with permission from [(Ref. [53]) Sunanda P. Koduvayur, Yuli Lyanda-Geller, Sergei Khlebnikov, Gabor Csathy, Michael J. Manfra, Loren N. Pfeiffer, Kenneth W. West, and Leonid P. Rokhinson. Phys. Rev. Lett. 106, 016804, 2011.] Copyright (2020) by the American Physical Society. (a) Anisotropy due to internal strain. (b) and (c) Thermally induced tensile strain along [110] and [1$\bar{1}$0], respectively, switches the easy transport axis.

2.6.3 Density of 2DEG

Most of the experiments have shown the easy axis of conduction to be $\langle 110 \rangle$. However, Zhu et al. [54] have reported the switching of the easy axis from $\langle 110 \rangle$ to $\langle 1\bar{1}0 \rangle$ upon increasing the in situ density of the 2DEG as shown in figure 1 of Ref. [54].

2.7 A proposed experimental test to determine the universality class based on hysteresis

The order parameter theory which best describes the system may depend on the chemistry of the system. We propose a test to distinguish them, assuming it is in the clean limit of both the Ising and the XY model.

As discussed in Section 2.4, a two dimensional Ising model undergoes spontaneous symmetry breaking at low enough temperature but a two-dimensional XY model does not according to the Mermin-Wagner theorem. The 2D Ising model is a candidate of hysteresis when we change the h-field in the ordered phase. But the XY model does not show hysteresis as there is a goldstone mode in the absence of any field which can destroy nematic order.

The effect of an in-plane magnetic field on the nematic order is discussed in Section 2.6.1. Since, the nematic order is symmetric under π rotation and the nematic order parameter switches sign upon a $\pi/2$ rotation, the dependence of the orienting field on the applied in-plane magnetic field has to be of the form $h \propto (B_x^2 - B_y^2)$ to the lowest order in a Taylor expansion. Hence $h \sim B_\parallel^2 \cos(2\phi)$ is invariant under π rotation which preserves the symmetry of the Hamiltonian. An appropriate choice of $B_\parallel$ can cancel the effect of h_{int} which is determined by the microscopics of the system. Other external perturbations also contribute to an orienting field, such as uniaxial strain (Section 2.6.2), electron density in the 2DEG (Section 2.6.3) [53, 54]. In all models, a phase transition only exists at zero orienting fields, $h = 0$. In the Ising case, the phase transition is into a low-temperature, long-range ordered nematic phase which spontaneously breaks rotational symmetry. For the 2D XY model, the phase transition is in the BKT universality class, and the low-temperature phase is critical throughout the temperature range, with no long-range order, and therefore no net nematicity $\mathcal{N}$, measurable by $\mathcal{N} \propto (\rho_{xx} - \rho_{yy})/(\rho_{xx} + \rho_{yy})$. Upon field cooling in any weak h, *all models* will develop a net nematicity below a crossover temperature

which is close to the phase transition temperature, whether $T_c = 2.27J$ in the Ising case, or $T_{KT} = .89J$ in the XY case.

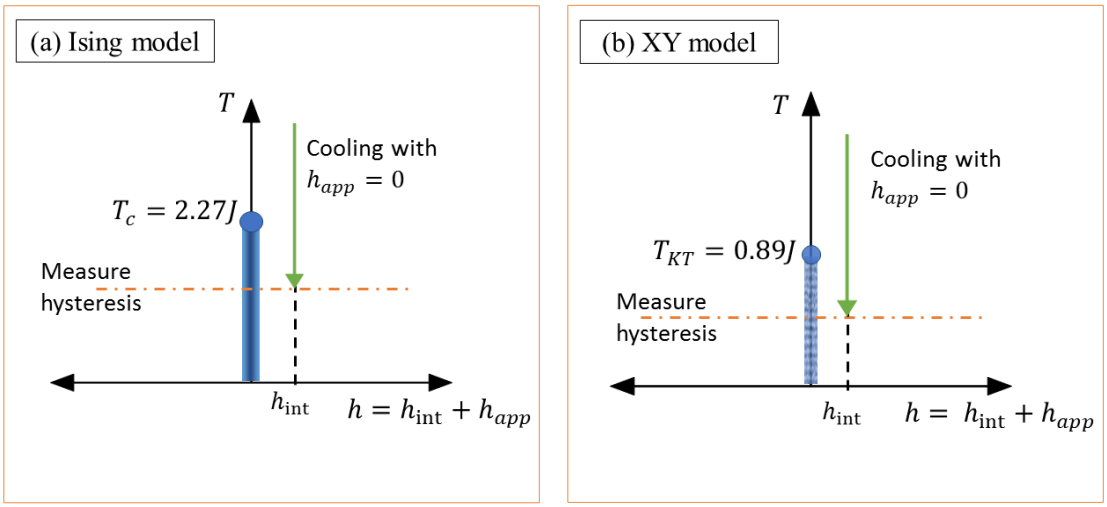

Figure 2.8. Equilibrium phase diagram for (a) two-dimensional Ising model and (b) two-dimensional XY model. In both cases, a low-temperature phase transition occurs only without an orienting field $h = 0$. In the Ising case, the low-temperature phase has long-range nematic order, and in the XY case, the low-temperature phase only has topological order but no long-range nematic order. The experimental hysteresis test we propose begins by (i) cooling (green arrow) with or without applied field h_{app}, followed by (ii) sweeping the orienting field h_{app} so as to move the system back and forth across the low-temperature phase (orange dotted line). Refer to Fig. 2.9 for the experimental prediction of the response of the nematicity $\mathcal{N}$ as a function of applied orienting field.

However, hysteresis can clearly distinguish between these universality classes. The hysteresis protocol we propose (shown in Fig. 2.8) is the following [49]: Cool in an orienting field $h > 0$ such as in-plane magnetic field (see Ref. [55, 56] for a list of orienting fields), and go to low temperature, well within the nematic region. Then, reduce h to zero, and sweep it to negative values $h < 0$. Using, *e.g.*, in-plane magnetic field as an orienting field, this is equivalent to cooling with an in-plane field configuration of $\vec{B}_{\text{in-plane}} = (B_x > 0, B_y = 0)$, then holding the temperature fixed, decreasing

B_x to zero, then immediately increasing the field B_y from zero while holding $B_x = 0$ so as to end with an in-plane field configuration of $\vec{B}_{\text{in-plane}} = (B_x = 0, B_y > 0)$. Indeed, quantum Hall stripes can be reoriented via application of in-plane field [51]. At low temperature in the Ising case, there is hysteresis in the net nematicity $\mathcal{N}$ as the in-plane field is swept so as to take h from positive to negative and back again, or *vice versa*. Therefore in the Ising case, the net nematicity should remain in an oriented state, until the coercive field strength $h_c \neq 0$ is reached.

However, in the XY case, there should be no hysteresis. This follows from the Mermin-Wagner-Hohenberg theorem, since decreasing an applied field h so as to end on the critical phase at $h = 0$ can leave no long range order, $\mathcal{N}(h \to 0) \to 0$ where $\mathcal{N}$ is the net nematicity. Because $h \to 0$ with $T < T_{\text{KT}}$ is critical, $\mathcal{N} \propto h^{(1/\delta)}$ as field is swept, where the critical exponent $\delta = (4/\eta) - 1$ varies from $\delta(T_{\text{KT}}) = 15$ to $\delta(T \to 0) \to \infty$ [57]. This case is shown in Fig. 2.9(b) [49].

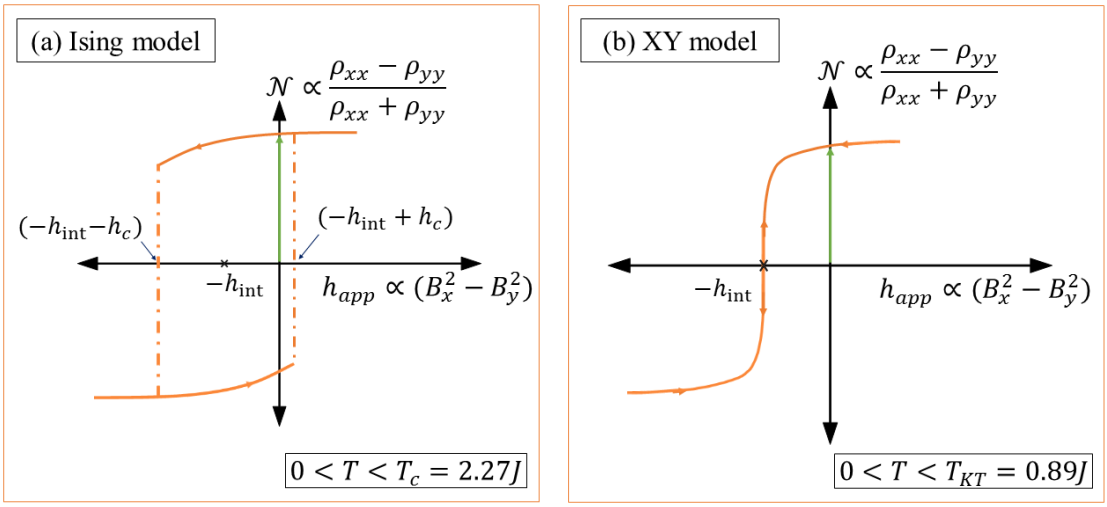

Figure 2.9. Predicted result of hysteresis test for (a) an Ising nematic and (b) an XY nematic. Cooling (green arrow) the system below T_c (Ising) or T_{KT} (XY) gives rise to a net nematicity in the presence of any orienting field h, including the case of no applied orienting field, since then $h = h_{\text{int}} \neq 0$. Subsequently sweeping the in-plane orienting field gives rise to either hysteresis in the Ising case, or no hysteresis in the XY case.

It should also be noted that the test is clearest in clean samples, since the addition of random field effects in the presence of a net orienting field h puts both models in the universality class of the random field Ising model [58], which has hysteresis at a low temperature. Whereas hysteresis of a clean Ising model has a net macroscopic jump in the nematicity, hysteresis of a random field Ising model is smooth in two dimensions [59]. At very weak but finite random-field strength, the model predicts avalanches in the resistivity anisotropy around the hysteresis loop with power-law behavior set by critical exponents characteristic of the 2D random field Ising model critical point.

Note that our simulations, as well as those of Ref. [5], indicate the presence of a weak intrinsic orienting field, h_{int} in the sample, on the order of $h_{\text{int}} \approx 3 - 5\text{mK}$. (Section 2.6) This means that to achieve $h = 0$ requires that some extrinsic orienting field, such as an in-plane magnetic field or uniaxial strain [55, 56], must be applied to compensate. Assuming this could be achieved, then zero-field cooling (ZFC) with $h = h_{\text{int}} + h_{app} = 0$ has stark differences in the two models. In the Ising case, ZFC gives rise to long-range order with net nematicity and macroscopic resistivity anisotropy, with Ising critical behavior at the onset of nematicity, and the direction of that nematicity can randomly switch upon repeated cooling at $h = 0$. In the XY case, ZFC can't produce long-range order or net nematicity, but the system would instead enter a topological phase with power-law nematic order, and accompanying critical phenomena.

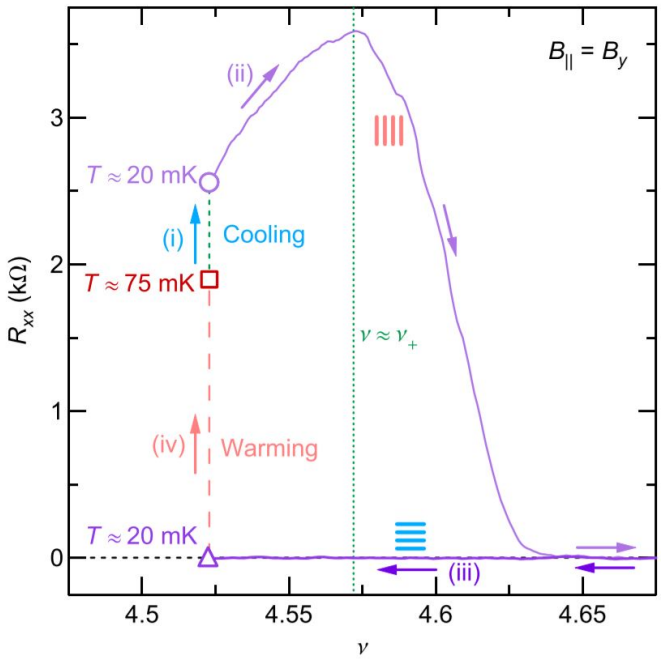

Figure 2.10. Reprinted figure 2 with permission from [(Ref. [60]) Q. Shi, M. A. Zudov, B. Friess, J. Smet, J. D. Watson, G. C. Gardner, and M. J. Manfra. Phys. Rev. B 95, 161404(R), 2017.] Copyright (2020) by the American Physical Society. Experimentally observed temperature-induced hysteresis by Shi *et al.* near half-filling upon changing the LL filling and in presence of a small (constant) in-plane magnetic field.

In Ref. [60], Shi *et al.* showed (Fig. 2.10) that a nematic can maintain its orientation at a low temperature when the LL filling is changed. The nematic re-orients to its equilibrium orientation only upon heating. This behavior is not possible for a nematic falling in the XY universality class because it is reoriented at any finite temperature. Although hysteresis only at a constant filling fraction is discussed here, the observed hysteresis upon changing filling in the presence of a small (constant) in-plane field reinforces the idea that these NQHMs possibly belong to the Ising universality class .

2.8 Conclusion

To summarize, we have shown that the temperature-dependent anisotropic resistivity in NQHM at $\nu = 9/2$ can be entirely described by an Ising order parameter model. We have also outlined an experimental method for hysteresis to distinguish Ising nematic from XY nematic, which generally applies to any system which may be described by an Ising model or an XY model. We also recognized experimental evidence of Ising behavior in a hysteresis protocol different than our protocol, but ultimately reinforcing our idea of NQHMs falling in the Ising universality class.

3. PERIOD MULTIPLICATION CASCADE AT THE ORDER-BY-DISORDER TRANSITION IN UNIAXIAL RANDOM FIELD XY MAGNETS

3.1 Introduction

The XY model, in which interacting spins are confined to rotate within a plane, has been a staple of statistical mechanics and condensed matter studies, having been applied to a broad range of physical systems including planar magnets, superfluids, superconductors, two-dimensional melting, nematic liquid crystals, and electron nematics, among others. [3, 9, 10, 61–67] In two dimensions, the XY model exhibits a BKT transition to a power-law ordered phase, yet with no long-range order. [7, 68] As such, the addition of random fields to a two-dimensional XY model is expected to result in even less order: Imry and Ma argued that a ($d \leq 4$)-dimensional system with continuous order parameter (with O(n) symmetry with $n \geq 2$) in the presence of random fields cannot have long-range order for any finite disorder strength. [69]

However, the addition of uniaxial random fields reduces the global symmetry of the Hamiltonian, and the Imry-Ma argument no longer applies. [13] In this case, the low-temperature phase has long-range order via an order-by-disorder transition, in which XY spins align perpendicular to the random fields. [13, 16] This is a special case of a more general class of order-by-disorder transition, where an n-dimensional spin system orders in an (n-k)-dimensional subspace due to orthogonal k-dimensional random fields. [9, 10, 13, 17]

We consider the possibility of a non-equilibrium transition. We use simulations to study the order-by-disorder transition in the presence of a rotating driving field at zero temperature.

By analyzing the avalanche size distribution as a function of the magnitude of an applied driving field, we find evidence that the system undergoes a continuous non-equilibrium phase transition at a critical amplitude of the driving field. Once a limit-cycle is established, we observe that the period of the hysteresis loops become n-fold near a critical applied field strength, where n is as large as 7 in our largest systems. We present evidence that the period of the subharmonic entrainment is rigid against perturbations in initial conditions, and perturbations of the drive field, indicating that a classical discrete time-crystal emerges near criticality. [70, 71] We present finite-size scaling evidence that the period of these multi-period limit-cycles will diverge in the thermodynamic limit. An experimental test of this would be the presence of non-repeatability in the response due to a rotating driving field near the transition.

As discussed further in section 3.5 there are several experimental systems corresponding to the XY model into which uniaxial random field disorder can be incorporated, whereby these ideas can be tested experimentally. These include layers of Josephson junctions, [61] superfluid in a uniaxially stressed aerogel, [62] ultracold atoms in the presence of speckle radiation, [9] uniaxially stressed 2D Wigner crystals, [63–66] the half-integer quantum Hall effect, [3] and possibly the graphene quantum Hall ferromagnet. [10, 67]

3.2 Models

3.2.1 2D Ising model with Disorder

The energy of the random field Ising model is given by the following Hamiltonian:

$$\mathcal{H}^{RFIM} = -J \sum_{\langle i,j \rangle} \sigma_i . \sigma_j + - \sum_i (H + h_i) . \sigma_i \tag{3.1}$$

The critical field strength for a 2D Ising model with random fields is zero in the thermodynamic limit. But in a finite-size system, the critical field strength is dependent on the system size and the random field strength. The near the critical field strength

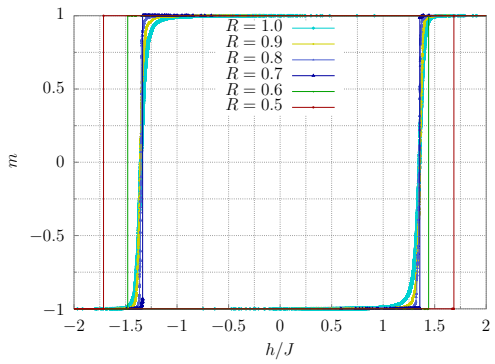

(a) Ising model, $T \to 0,\ N = 1024^2$

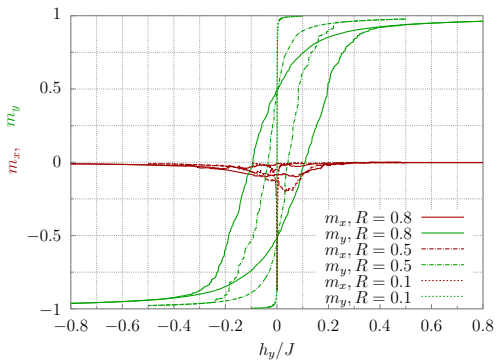

(b) XY model, $T \to 0, R_x = R_y = R,\ N = 128^2$

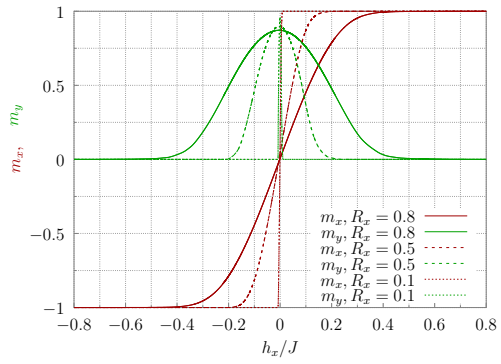

(c) XY model, $T \to 0,\ R_y = 0,\ N = 128^2$

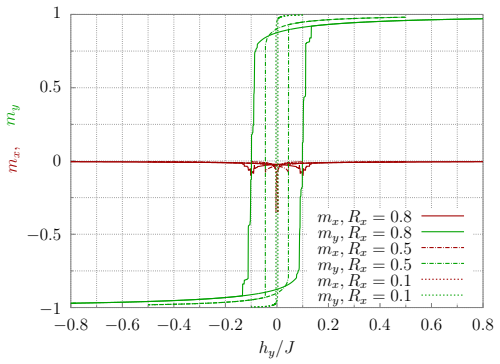

(d) XY model, $T \to 0,\ R_y = 0,\ N = 128^2$

Figure 3.1. (a) Hysteresis of Ising model of 1024^2 sites at zero temperature with Gaussian distribution of random field given by R in each plot. (b) Hysteresis of XY model of 128^2 sites at zero temperature with isotropic Gaussian distribution of random fields given by $R_x = R_y$. The hysteresis curves were generated for an applied field along Y-axis. (c) Hysteresis of XY model of 128^2 sites at zero temperature with uniaxial Gaussian distribution of random fields given by R_x . The hysteresis curves were generated for an applied field along X-axis. (d) Hysteresis of XY model of 128^2 sites at zero temperature with the uniaxial Gaussian distribution of random fields given by R_x . The hysteresis curves were generated for an applied field along Y-axis.

the Ising model has avalanches at all length scales. An avalanche is described as flipping a large cluster from up (+1) to down (−1) or vice versa triggered by desta-

bilizing a few spins. Figure 3.1(a) shows that upon increasing the Gaussian random field strength the critical field strength decreases.

3.2.2 2D XY model with Disorder

The energy of the random field XY model is given by the following Hamiltonian:

$$\mathcal{H}^{RFXY} = -J\sum_{\langle i,j\rangle}\vec{S}_i.\vec{S}_j + -\sum_i(\vec{H}+\vec{h}_i).\vec{S}_i \tag{3.2}$$

The XY model with random field disorder would have a coercive field strength which increases with disorder strength. The following two cases are quite distinct:

2D XY model with Isotropic Random Field

When the random fields point in any direction with the same probability, the random field are said to be isotropically distributed. In this case, the critical field strength increases with increasing random field strength. The axis along which the driving field is swept is irrelevant. The effect of increasing random field strength on zero temperature hysteresis is shown in figure 3.1(b).

2D XY model with Uniaxial Random Field

The uniaxial random field case is a special case. As described in section 1.2, there is an emerging Ising character in this system which arises due to the competing interaction between the spins and the on-site field.

There is no hysteresis if the field is swept along the axis parallel to the random fields. A constant nominal field is applied along the Ising symmetry axis to break this symmetry while sweeping the field along the random field axis. The results for different strengths of random fields are shown in figure 3.1(c).

The hysteresis curves upon field sweep along the emerging Ising symmetry axis makes the system undergo avalanches similar to the random field Ising model. The

results for different strengths of random fields are shown in figure 3.1(d). Unlike the random field Ising model, here the critical field strength increases as a function of random field strength, since the stability of the Ising like order parameter is dependent non-monotonically on Random field strength. The non-monotonicity comes from the fact that if the random fields are too large then the local spins will be aligned with the random fields which are randomly oriented giving no net order. Hence, only at intermediate random field strengths one would observe the order-by-disorder transition of the Uniaxial Random Field XY model to the Ising universality class.

In the subsequent sections, we concentrate on the uniaxial random field XY model on a square lattice, in the presence of driving applied field $\vec{H}[\phi]$, with constant magnitude $H = |\vec{H}|$ given in Eqn. 1.1. We study this system at zero temperature under the influence of a rotating applied driving field whose angle $\phi = \omega t$ advances in time slowly, in the $\omega \to 0$ limit. The dynamics is quasi-static: after each small increment of the driving field angle, the energy of the system is minimized. (See section 3.6 for details of the simulation method.) This type of dynamics [1] presupposes that the system is connected to a heat bath which prevents heating by the drive.

Symmetry considerations imply that the timescales associated with barriers to equilibration of this model diverge exponentially near criticality [72], for the following reasons. In the presence of a uniform applied field H, the symmetry of the XY model is reduced to that of the Ising model. This means that the system can have a symmetry-breaking transition, in which a spontaneous magnetization forms perpendicular to the applied field H. Adding a uniaxial random field along any axis that is not parallel to H applies random fields to that Ising variable, placing the critical behavior in the universality class of the random field Ising model. It is well-known that the timescales to equilibration diverge exponentially with proximity to criticality in the random field Ising model. [72] In fact, at the corresponding critical point, temperature fluctuations are irrelevant in the renormalization group sense, meaning they are not necessary in order to capture the essential critical behavior. During a single cycle of the rotating applied field we consider here, the symmetry of the system remains in the universality

class of the random field Ising model, except for a set of measure zero (when H is parallel to the random fields). Therefore, as the applied field is rotated, the system is forced to traverse regions with enormous energy barriers most of the time. On long enough length scales, these energy barriers must be present. For a given rate of dissipation of the heat bath, the energy barriers can be made to diverge sufficiently to beat the rate of dissipation by moving closer to criticality. Thus, we study our model at zero temperature, for the same reason that zero temperature results from the random field Ising model have been applied to many disparate physical systems, some even at room temperature. [73]

3.3 Results

3.3.1 Behavior of the Limit Cycles

Fig. 3.2 shows the rich behavior of the limit-cycles in rotating driving field, as a function of the magnitude of the driving field H at intermediate disorder strength $R_x = 0.5J$. Panel (b) shows the sense of the driving field, which is held at constant magnitude, but rotated counterclockwise, *i.e.* ϕ increases in time as $\phi = \omega t$ in the $\omega \to 0$ limit, starting from $\phi = \pi/2$. Fig. 3.2 (a) shows a plot of m_x *vs.* the angle ϕ of the applied field. Panel (d) shows a plot of m_y *vs.* the angle ϕ of the applied field. Panel (c) shows the combined parametric plot of magnetization m_x in the x direction, plotted against the magnetization m_y in the y direction. The sense of the parametric plot in panel (c) is counterclockwise. In each case, the system is started from a locally stable configuration in an applied field $\vec{H}||\hat{\vec{y}}$ at zero temperature, which has been relaxed from an initially saturated state aligned with the applied field. This The transient response before the limit-cycle is not shown in this figure. We discuss the transient response in section 3.3.3.

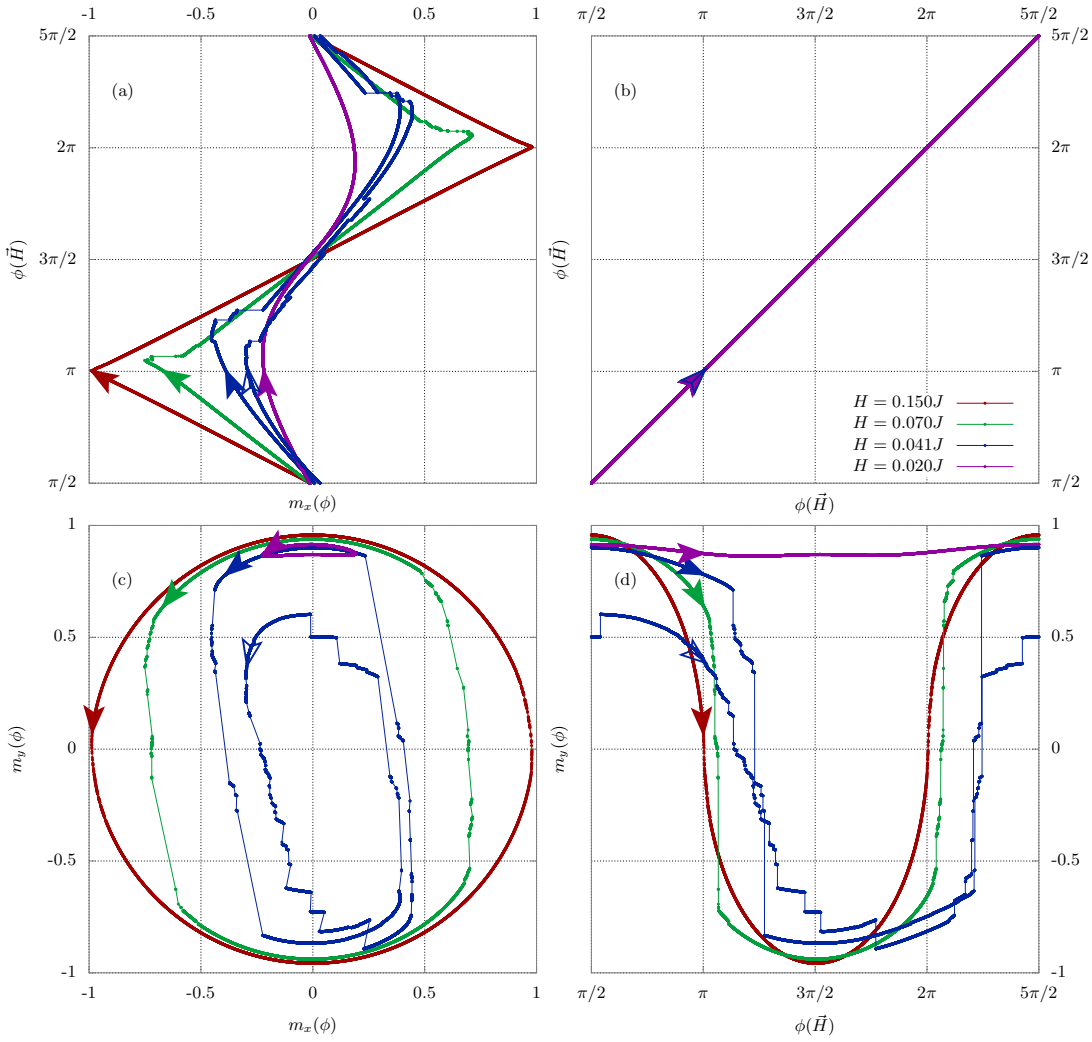

Figure 3.2. Steady state response to rotating applied field at $T = 0$. A system of size $N = 160 \times 160$ with $R_x = 0.5J$ is started from an initial applied field in the y-direction. The initial spin configuration is aligned with the applied field, then relaxed according to Equations (3.4) as described in the text, after which the applied field is rotated counterclockwise as denoted in panel (b). Panels (a), (c), and (d) show the response once a steady state is reached under the driving field. Panel (a) shows the response of the magnetization in the x direction, while panel (d) shows the response of the magnetization in the y direction. Panel (c) is a parametric plot of m_y *vs.* m_x. In all panels, the arrows denote the state of the system when the driving field is at an angle $\phi = \pi$, *i.e.* aligned along the x direction. For driving field strength $H = 0.041J$, the response of the system has double the period of the driving field. The open arrow on this trace denotes the state of the system at driving field angle $\phi = \pi$ during every other cycle of the driving field.

For moderate disorder strength $R_x = 0.5J$, we find that at small amplitudes of the driving field, the spontaneous magnetization in the y direction remains robust. This is evident in the small hysteresis loops we find for $H = 0.02J$ as shown by the purple trace in the parametric plot Fig. 3.2(c). This indicates that the system continues to display spontaneous symmetry breaking in the y direction, retaining its Ising ferromagnetic character in the presence of a weak rotating driving field.

As the magnitude of the applied field is increased, there is a change in behavior from ferromagnetic to paramagnetic response. This is evident in the large, almost circular hysteresis loop we find for larger $H = 0.15J$, as shown by the red trace in the parametric plot Fig. 3.2(c). This change is consistent with either a crossover in behavior or a non-equilibrium phase transition at a critical magnitude of the driving field. Note that the rotating hysteresis loops at intermediate driving field strengths $H = 0.041J$ and $H = 0.07J$ have a rich structure: Numerous avalanches are evident in these traces. As we will see in Sec. 3.3.2, the avalanche structure provides further insight into the question of whether the change from ferromagnetic to paramagnetic response is a crossover or a phase transition. Perhaps the most intriguing feature of the intermediate driving field regime is that in the blue trace ($H = 0.041J$), the limit-cycle has double the period of the driving field. We find that limit-cycles often become multi-periodic at intermediate field strength, for a large enough system size. We explore this region of the phase diagram in more depth in Sec. 3.3.4.

3.3.2 Avalanches Near the Transition

In this section, we focus on the characteristics of the avalanches that occur near the transition from Ising ferromagnetic to a paramagnetic response. We find a rich avalanche structure at intermediate field strengths, as can be seen in the blue and green traces in Fig. 3.2 ($H = 0.041J$ and $H = 0.07J$, respectively). Notice that while the avalanches are apparent in both m_x and in m_y, they are most prominent in m_y, which serves as the order parameter in this system. When magnetization is

cast as an extensive quantity, $\vec{M} = \sum_{i=1}^{N} \vec{S}_i = N\vec{m}$, then in the thermodynamic limit, avalanches $\delta\vec{M}$ of diverging size accompany a second order phase transition.

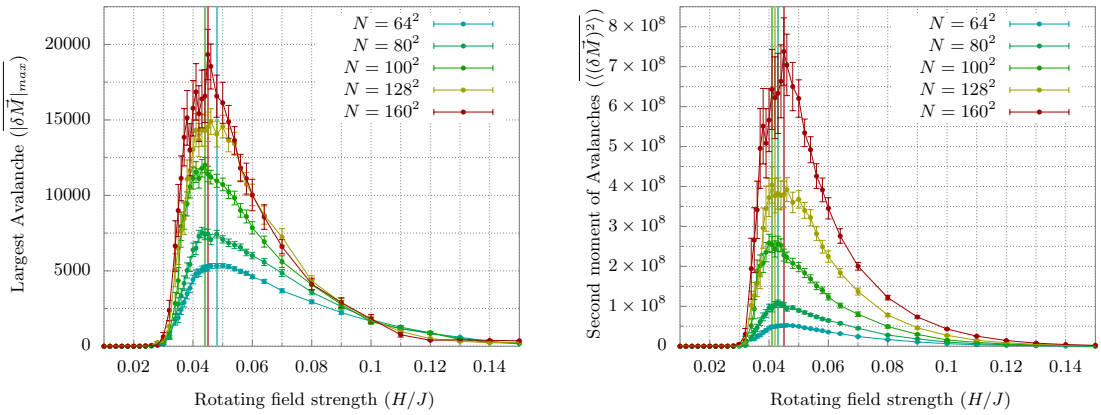

(a) Statistics of largest avalanches

(b) Statistics of second moment of avalanches

Figure 3.3. Avalanche statistics for disorder strength $R_x = 0.5J$ from zero temperature simulations. The response of the magnetization to a rotating driving field often proceeds via avalanches, in which there is a discontinuous jump in the magnetization $\delta\vec{M}$ in response to a small change $\delta\phi$ of the driving field angle. In panel (a), we plot the size of the largest avalanche $|\delta\vec{M}|_{\max}$ per limit-cycle at each rotating field strength, disorder-averaged, for a range of system sizes. Panel (b) shows the disorder-average of the second moment $\delta\vec{M}$ of the avalanche size distribution where the error bars are the standard deviation over the disorder average as described in the text. The brackets $\langle\ \rangle$ denote an average over the limit-cycle, and the overbar denotes a disorder average. By both of these measures, the size of the avalanches grows with system size implying divergent fluctuations at a critical field strength in the thermodynamic limit. The vertical bars in both panels mark the peak value from a running 3-point average. Within the resolution of the plot in panel (a), these values are coincident for sizes $N = 80 \times 80$ and $N = 100 \times 100$, and for sizes $N = 128 \times 128$ and $N = 160 \times 160$. In panel (b), the peak values are coincident for sizes $N = 64 \times 64$ and $N = 160 \times 160$.

Fig. 3.3(a) plots the size of the largest avalanche $|\delta\vec{M}|_{\max}$ at each rotating field strength, for a range of system sizes $N = L \times L$. Results are averaged over several disorder configurations of the random field at disorder strength $R_x = 0.5J$, ranging

from 75 disorder configurations for system size $N = 64^2$, to 30 disorder configurations for system size $N = 160^2$. (See Section 3.6.3.) Notice that fluctuations as measured by the largest avalanche diverge with increasing system size at a critical driving field strength, $H_c(R_x = 0.5J)$. We estimate the value of H_c at $R_x = 0.5J$ as follows: For each system size, the peak value based on a 3-point average is indicated by the vertical bar. The corresponding peak value of the applied field strength, averaged over all system sizes, is $H_c = (0.0452 \pm 0.0015)J$.

In Fig. 3.3(b), we plot the second moment of all avalanches in each limit-cycle, $\left\langle (\delta\vec{M})^2 \right\rangle$ at each rotating driving field strength, for a range of system sizes. Results are disorder averaged, using the same number of disorder configurations as in Fig. 3.3(a). Notice that this alternate measure of fluctuations based on the second moment of the avalanche size distribution is also consistent with the system undergoing a second-order, non-equilibrium phase transition at a critical driving field strength, H_c. In this case, we find that $H_c(R_x = 0.5J) = (0.0432 \pm 0.0016)J$, in agreement with the value of the critical field strength we find from Fig. 3.3(a).

3.3.3 Transient Response

Fig. 3.4(a-c) shows how the magnetization responds to a rotating driving field in the vicinity of the phase transition. There is a transient response before the system settles into a limit-cycle. A limit-cycle is a steadily repeating response in the magnetization due to a rotating driving field. While we find that most limit-cycles have the same period as the driving field, we find that near the transition regime, limit-cycles often have a longer period. We first discuss the behavior of the transient response, before turning our attention to the behavior of the multi-periodic limit-cycles in Sec. 3.3.4

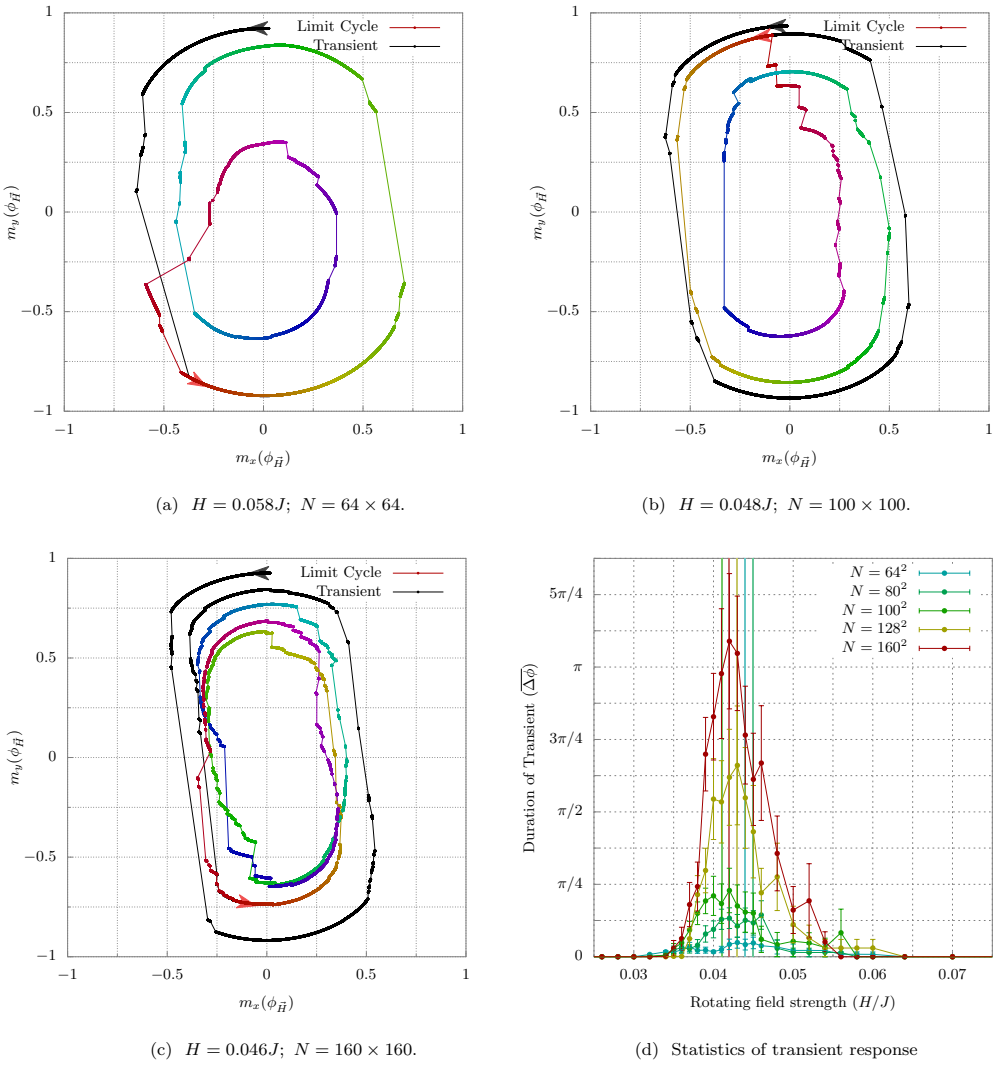

(a) $H = 0.058J$; $N = 64 \times 64$.

(b) $H = 0.048J$; $N = 100 \times 100$.

(c) $H = 0.046J$; $N = 160 \times 160$.

(d) Statistics of transient response

Figure 3.4. Transient response and multi-period limit-cycles at T=0 near the transition field strength for disorder strength $R_x = 0.5J$ with a specific disorder configuration for each system size. Panels (a-c) show the initial transient response (black curves), followed by multi-periodic limit-cycles (rainbow curves). (a) System size $N = 64^2$. Here, the transient response lasts roughly half a cycle before a period-2 limit-cycle is established. (b) System size $N = 100^2$. Here, the transient response lasts roughly one cycle before a period-2 limit-cycle appears. (c) System size $N = 160^2$. Here, the transient response lasts almost 1.5 cycles before a period-3 limit-cycle is established. (d) The disorder-averaged duration of the transient response, as a function of H. The error bars are the standard deviation over the disorder average as described in the text. The mean of the transient distribution function for each system size is marked by a vertical line of the corresponding color.

The transient response in panels (a-c) of Fig. 3.4 is marked in black. In Fig. 3.4(d), we plot the duration of the transient response, as a function of H, for various system sizes. The results shown have been averaged over several disorder configurations. (See Section 3.6.3 for details.) At high and low strength of the driving field, the transient response becomes so negligible as to be smaller than the symbol size on this graph. However, at intermediate driving field strength, the transient response grows with increasing system size. The fact that the transient response grows with increasing system size is further corroboration that the system is undergoing a second-order phase transition. In Fig. 3.4, the mean of each transient distribution function is denoted by a vertical line, color-coded to the system size. The average of the mean value of H from these vertical lines is $\langle H_{tr} \rangle_N = (0.0430 \pm 0.0014)J$, consistent with our previous estimates of $H_c(R_x = 0.5J)$.

3.3.4 Period Increase Near the Transition

We now turn our attention to the behavior of the limit-cycles at intermediate driving field strength. One of the most fascinating features of the limit-cycles in this regime is that some of them have a longer period than that of the driving field. Fig. 3.4 shows some representative cases of this behavior. Fig. 3.7 visualizes how the spin configurations respond to the driving field during one of the period-2 limit-cycles. Domain walls have dramatically different configurations during the second cycle as opposed to the first cycle of the driving field, suggesting a prominent role for domain wall pinning and domain wall creep. More examples of such behavior can be found in our videos [74] of the simulation results.

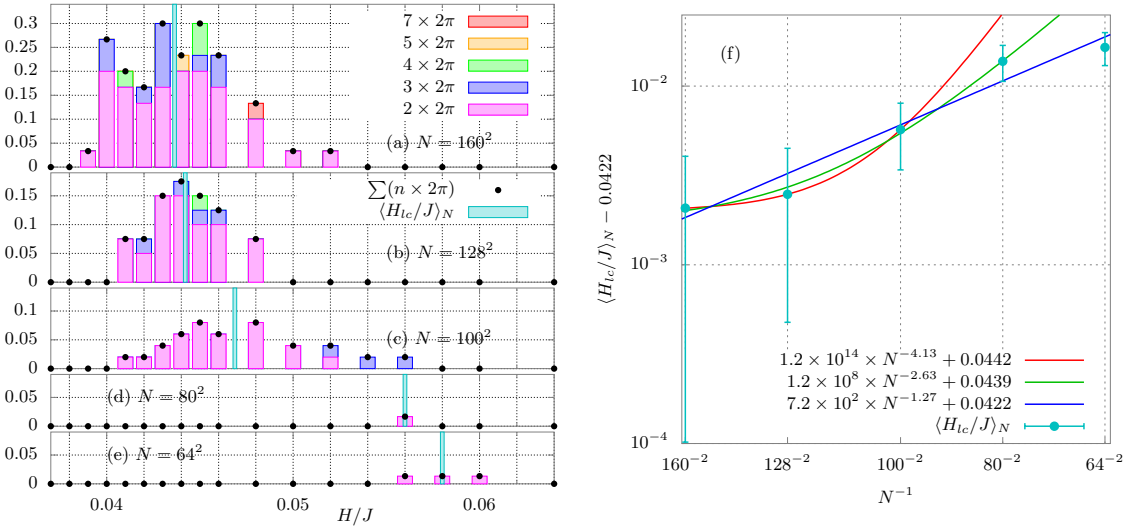

Figure 3.5. Multiperiod limit-cycles at zero temperature. Panels (a-e) show what fraction of limit-cycles that exhibit multi-periodicity as a function of driving field strength H at $R_x = 0.5J$. The smallest system size we simulated, $N = 64 \times 64$, is shown on the bottom left in panel (e). System size increases from bottom to top in the left panels, up to system size $N = 160 \times 160$. In the bar graphs, period-2 limit-cycles are shaded pink; period-3 limit-cycles are purple; period-4 limit-cycles are green; the period-5 limit-cycle is orange; and the period-7 limit-cycle is red. We did not observe any period-6 limit-cycles. Black dots represent the net contribution from all multi-period limit-cycles at each field. In each bar graph, the vertical blue line is the mean of the distribution function, $\langle H_{lc} \rangle$ in units of J. (f) From the results of panels (a-e), we plot $\langle H_{lc} \rangle_N$ *vs.* the inverse of system size N on a log-log scale. In Panel (f), the error bars are standard deviations over the histograms in Panels (a), (b), (c), and (e), respectively. For the fourth point (arising from Panel (d)), we estimate the error to be the average of that in the third and fifth points. A power-law fit of $\langle H_{lc} \rangle_N$ for the three largest system sizes is given by the red curve; the fit for the four largest system sizes is given by the green curve; and the fit for all calculated system sizes is given by the dark blue curve. The y-intercept is consistent among all of these fits, yielding an average value of $\langle H_{lc} \rangle_{N \to \infty} = (0.0434 \pm 0.0020)J$.

In order to explore this behavior quantitatively, we studied several disorder configurations near the transition, as a function of system size. Fig. 3.5 shows a histogram of the likelihood of multi-period limit-cycles. For a given magnitude of the driving field H and a given system size N, we plot the number of disorder configurations whose limit-cycle has a period greater than that of the driving field, divided by the number of all disorder configurations studied at that H and N. Starting from the bottom panel on the lefthand side of Fig. 3.5, panel (e), the system size increases as one moves to the next panel up the page, up to panel (a) which shows the largest system we studied, $N = 160 \times 160$. Different color bars indicate the period of multi-period behavior: pink indicates period-doubling; blue shows period tripling; period-4 limit-cycles are denoted in green; yellow is for period-5, and orange is for period-7. We did not observe any period-6 limit-cycles, although presumably these would appear at certain disorder configurations as well.

The vertical blue bars mark the mean of the distributions in Fig. 3.5(a-e), $\langle H_{lc} \rangle_N$. In Fig. 3.5(f), we plot $\langle H_{lc} \rangle_N$ vs $1/N$ on a log-log plot, in order to determine the limiting value $\langle H_{lc} \rangle_{N \to \infty}$. Fits of the finite size scaling in Fig. 3.5(f) for all system sizes, the four largest system sizes, and the three largest system sizes yield a consistent value for $\langle H_{lc} \rangle_{N \to \infty}$ within error bars. The average of these three methods yields $\langle H_{lc} \rangle_{N \to \infty} = (0.0434 \pm 0.0020)J$.

3.3.5 Approach to Non-Repeatability

We find that at small system sizes, multi-period behavior is rare. However, as the system size is increased, and the disorder configurations can become correspondingly more rich, the likelihood of multi-period behavior increases. In Fig. 3.6(a), we plot the maximum observed period of a limit-cycle, *vs.* $1/N$. The maximum period increases with increasing system size, in a manner consistent with a diverging period in the thermodynamic limit.

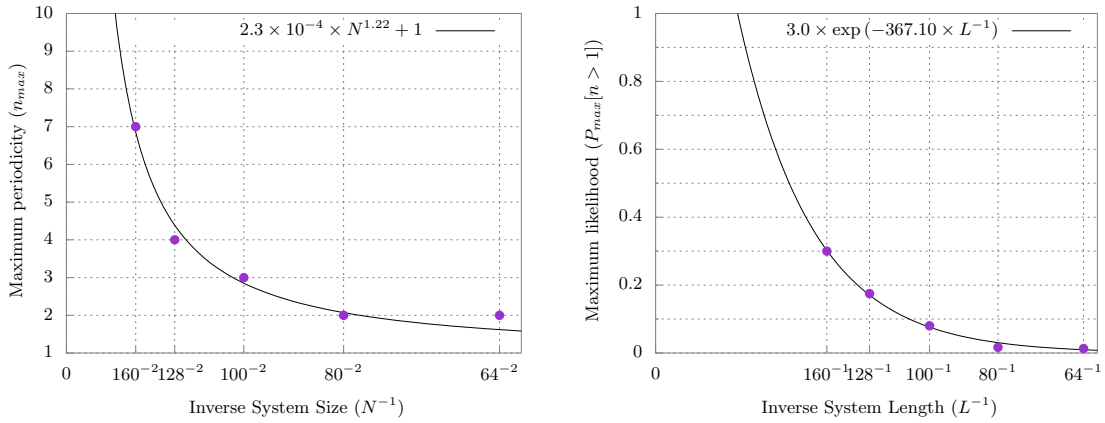

(a) Maximum period of limit cycles.

(b) Maximum likelihood of multiperiod limit cycles.

Figure 3.6. Trends of the zero temperature multi-periodic behavior of the limit-cycles with increasing system size. In panel (a) we plot the maximum period of the limit-cycles observed in Fig 3.5(a-e), as a function of 1/N (purple circles). The black line is a fit to the simulation results. The trend is toward divergence of the period of limit-cycles in the thermodynamic limit. In panel (b), we plot the maximum likelihood of multi-periodic limit-cycles, obtained from the peak heights of the left-hand panels in Fig 3.5 (purple circles). The black line is a fit to the simulation results. The trend is toward saturation of the likelihood of multi-period behavior in the thermodynamic limit.

Notice also that the distribution in Fig. 3.5(a-e) grows in height with increasing system size. For $N = 160 \times 160$, we find that $20-30\%$ of disorder configurations in the range $H = (0.04 - 0.046)J$ display multi-periodic behavior. To quantify these effects, we plot the maximum height of the distributions in Fig. 3.5(a-e) in Fig. 3.6(b). This measure also shows sharp increase with increasing system size. The fact that both the likelihood of multi-period behavior and the period of limit-cycles steadily increase with increasing system size points toward a thermodynamic limit in which the period of limit-cycles goes to infinity. If the period of a system diverges in the thermodynamic limit, then the system has effectively entered a regime of non-repeatability. We discuss further implications of this finding in the next section.

3.3.6 Spin configurations under driving rotating field

In our zero temperature simulations, energy is minimized for each site based on the local field and the configuration of the nearest neighbor interactions. We use two types of driving protocol: one is changing the driving field angle (ϕ) at a constant rate; the other one is a variable rate where the rate is slowed down if the change in response magnetization is large and sped up if the response is small. Both these protocol gives us the same periodicity of the limit-cycle. For example, if the constant rate is too large it can merge two avalanches into one but the overall magnetization remains the same.

We also observe that the system falls into the same limit-cycle however we initialize the spins. Due to the emergent Ising symmetry in the system and the above observation, the limit-cycles will be the same irrespective of the sense of rotating driving field. This is because the spin configurations can be mapped by a symmetry transformation from the response limit-cycle of a clockwise rotating field to the response limit-cycle of counter-clockwise rotating field. Only the transient response depends on the initial spin configuration.

Figure 3.7 shows the various spin configurations the system goes through before and during a limit-cycle with periodicity 4π. The rich structure of the domain walls are stable due to the random field distribution. All the plots in Fig. 3.7 are unique and Figs. 3.7(a-i) does not repeat but Figs. 3.7(j-cc) are part of the limit-cycle which repeats indefinitely. See []PURR3260 for better visualizations of the evolving spin configurations in limit-cycles with $n > 1$ periods.

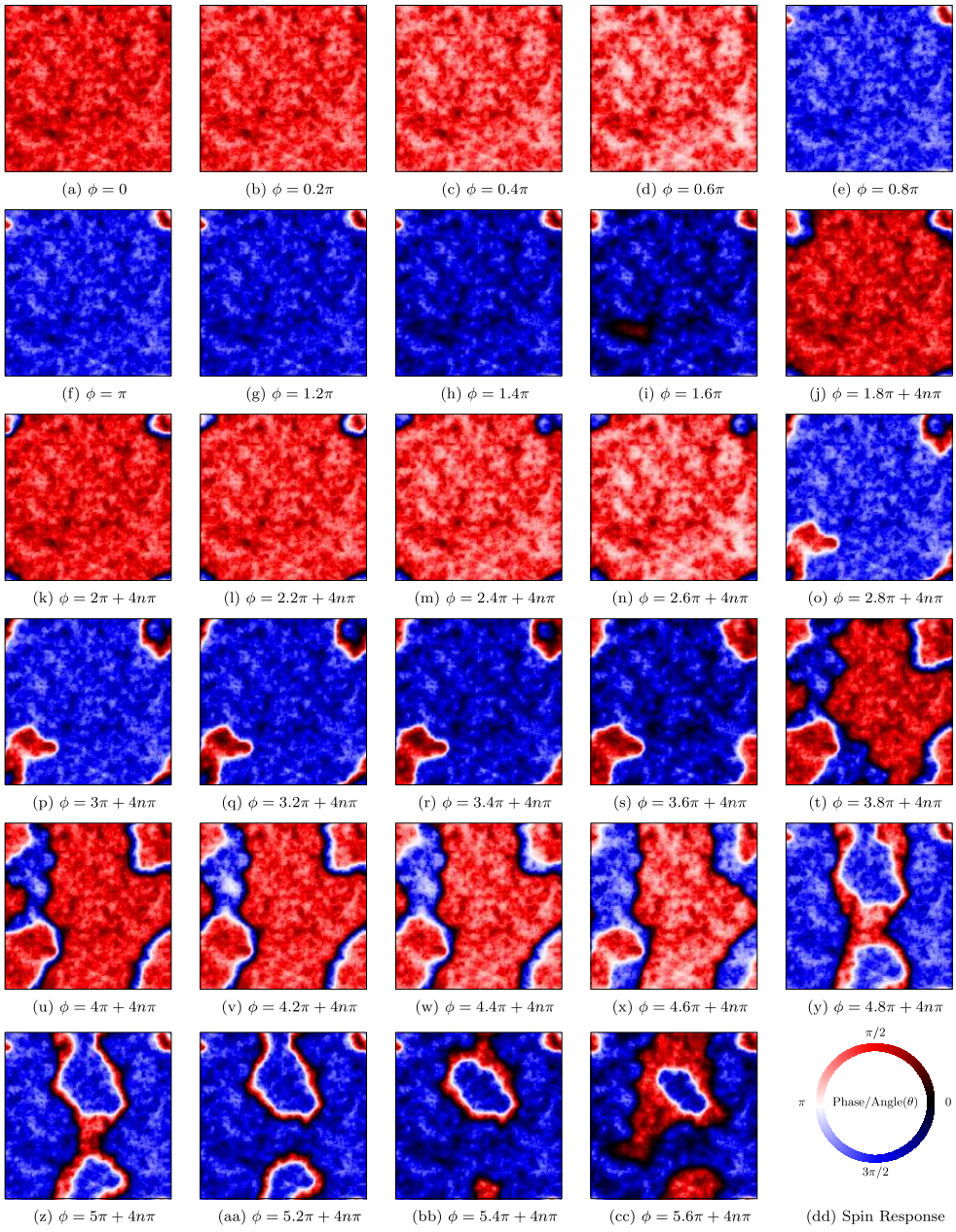

Figure 3.7. Example of spin configurations during a period-2 limit-cycle with transient response of less than 2π. The spin configurations (a-i) are the transient response which does not repeat. The spin configurations (j-cc) are for a limit-cycle with a period of 4π which is twice the periodicity of the driving field. Spin configurations (j-s) are different in the next cycle (t-cc) of the driving field for the same angle ϕ of the driving field. For this particular disorder configuration and system size, the spin configurations repeat every 2 periods of the driving cycle. Here, the driving field strength is $H = 0.04J$, and the system size is 160×160. See the videos in Ref. [74] of simulation results for further examples.

3.4 Evidence of Non-repeatability

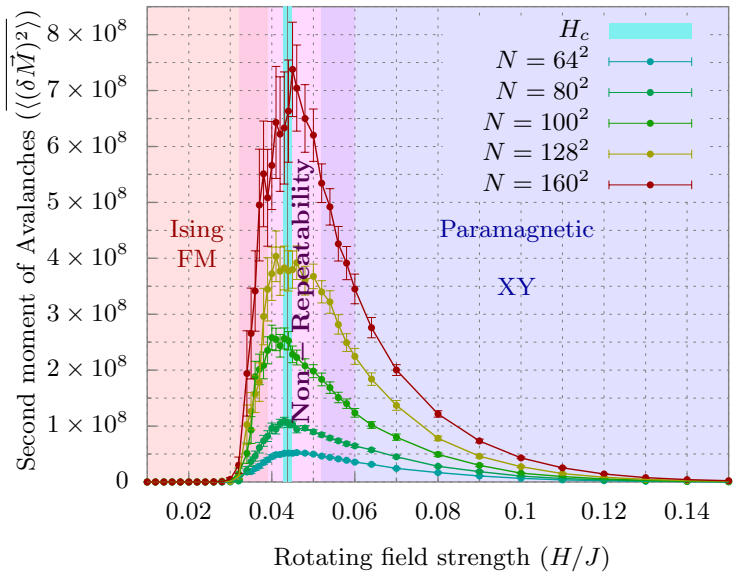

Figure 3.8. This figure shows the zero-temperature phase diagram as a function of the strength of the rotating field in a uniaxial Random field. The region where the number of multi-periodic loops and the maximum periodicity increases with system size is labeled as the expected region of non-repeatability for infinitely large systems. This region coincides with the region where the largest avalanche occurs is this system where $\langle H_c \rangle = (0.0437 \pm 0.0009)J$, which is marked by the vertical blue line. The line plots shows that the disorder-average of the second moment $\delta\vec{M}$ of the avalanche size distribution where the error bars are the standard deviation over the disorder average as described in the text. The brackets $\langle\ \rangle$ denote an average over the limit-cycle, and the overbar denotes a disorder average.

Using four different methods to quantify the fluctuations in the system (see Table 3.1), we find evidence for a second-order non-equilibrium phase transition from spontaneous Ising ferromagnetism at low driving field strength, to XY paramagnetism at high driving field strength. The critical field strength at which this transition

occurs is consistent across all methods we employed, yielding an average value of $H_c = 0.0437 \pm 0.0009$, as denoted in the phase diagram in Fig. 3.8.

Table 3.1.
Critical field strength.

Method	Value of H_c/J
Largest avalanche of limit-cycle	0.0452 ± 0.0015
Second moment of avalanches in limit-cycle	0.0432 ± 0.0016
Duration of transient response	0.043 ± 0.0014
Finite size scaling of multi-periodic behavior	0.0434 ± 0.0020
Overall average of above methods	0.0437 ± 0.0009

We furthermore find that far from being irrelevant, disorder plays a prominent role near the transition. Because the disordered energy landscape makes the system highly susceptible to spatial fluctuations near the transition, there is both longer transient response and a longer period of limit-cycles near H_c. Remarkably, both the likelihood of multi-period behavior and the period of the limit-cycles increase with no sign of saturation as the system size is increased. The trend we find is toward a thermodynamic limit in which limit-cycles never repeat. A large enough physical system at this critical point should therefore display a regime of non-repeatability. As shown in Fig. 3.8, the regime of non-repeatability in the thermodynamic limit coincides with the non-equilibrium phase transition. The dependence of this simple model upon history implies that experiments on XY systems with uniaxial random fields are particularly sensitive to disorder. Conflicting experimental results could arise if hysteresis protocols are not closely monitored.

Similar behavior is predicted to occur in models of amorphous solids under periodic shear stress. [1, 2, 75]. In these systems, simulations revealed that under periodic shear, the response of the system becomes multi-periodic, in a way that is consistent with chaotic behavior at a critical shear amplitude. More work would be needed to

determine whether the multi-periodic cascade observed here is indicative of chaotic behavior in the thermodynamic limit. Similar multi-period cascades signal the onset of chaos in nonlinear systems, suggesting that the multi-period cascades observed here and in periodically driven models of amorphous solids are characteristic of a larger class of transitions in dynamical systems.

While the discussion above points toward non-repeatability in the thermodynamic limit, there is a way to take the thermodynamic limit on this model such that n remains finite. A finite system of size $L \times L$ with a particular disorder pattern at the critical point has a finite period n with respect to the driving period. Now tile space by making k copies of this system (including the particular disorder pattern), and let $k \to \infty$. With this method of taking the thermodynamic limit, the period n remains finite, even for increasing system size. We have verified that when a disorder pattern is tiled into a 2×2 superlattice of the original disorder pattern (*i.e.* $k = 4$) then the spin response in the limit-cycle is also a superlattice of the original spin configuration, and n is unchanged from the case $k = 1$.

By this second method of taking the thermodynamic limit, in the vicinity of the non-equilibrium transition, the system should display the characteristics of a classical [70, 71] discrete time-crystal [76–78], in which the discrete time-translation symmetry imposed by the periodic drive is spontaneously broken in a way that leads to rigid subharmonic entrainment. While some authors are willing to apply the label time crystal to an open system, where energy from the drive moves through the system into a heat bath (as in the present case) [70, 77, 79], others prefer a more restrictive use of the term time crystal, reserving it for closed, conservative systems [80]. We are using the term time crystal in the former, broader sense.

We find that the period of the response remains stable against perturbations in the initial conditions and stable against low-temperature fluctuations (see Section B in Supplementary Information), indicating that the spontaneous breaking of the discrete time-symmetry is rigid. Yao *et al.* [70] find that the critical endpoint between a classical discrete time-crystal and the disordered phase of a dissipative, coupled chain

of classical nonlinear pendula terminates in a critical point which is not in an Ising universality class. Because the non-equilibrium transition we find here is in an Ising universality class, this indicates that there is more than one classical discrete time-crystal universality class. The results here further underscore the fact that long-range interactions are not a necessary ingredient to stabilize a time crystal. [81]

While our results point to the rigidity of n to very low-temperature fluctuations, more analysis would be needed to establish whether the n is truly long-range ordered in time. However, what we observe is a promising avenue toward time crystal behavior in a new system, as can be seen in Fig. 3.7. The figure shows a period-2 limit-cycle. Two types of domain walls are evident in the figure: single domain walls that are either white or black, and double domain walls that are white and black. Comparing Fig. 3.7(k) and Fig. 3.7(u), it is evident that on the second time through the driving cycle, the domain walls are in a very different configuration as compared to the first time through the drive cycle. The same is true while comparing Fig. 3.7(p) and Fig. 3.7(z). Furthermore, the single (white) domain wall in the lower left of Fig. 3.7(p) has no counterpart in Fig. 3.7(z), and is topologically distinct from it. These are all indications that (1) the domain walls are pinned by the random fields, and therefore that (2) spin configurations in the second cycle likely have high energy barriers to spin configurations at the same phase of the drive during the first cycle. In random field models, the timescales to equilibration grow exponentially near criticality [72]. This combination of topological differences, domain wall pinning, and high barriers to equilibration is the physical origin of the stability of the period of these multi-period cycles against low-temperature fluctuations, and likely leads to true time-crystalline rigidity of n if care is taken in how the thermodynamic limit is approached and how dissipation is handled.

The work in this chapter was done at uniaxial random field strength $R_x = 0.5J$, with zero random field strength in the y-direction. Further work is needed to obtain the full phase diagram as a function of random field strengths R_x and R_y.

3.5 Applications to Physical Systems

The uniaxial random field XY model has been applied to many systems, including layers of Josephson junctions, [61] superfluid in a uniaxially stressed aerogel, [62] ultracold atoms in the presence of speckle radiation, [9] uniaxially stressed 2D Wigner crystals, [63–66] and the half-integer quantum Hall effect. [3] Uniaxial random field-induced order has also been discussed in connection with the graphene quantum Hall ferromagnet. [10, 67] We discuss below a few of these systems in which there is also a clear way to drive the system with a rotating field.

3.5.1 Electron nematics

An electron nematic occurs when the electronic degrees of freedom spontaneously break the rotational symmetry of the host crystal. Electron nematics have been observed or proposed in several material systems, including transition metal oxides like cuprate superconductors, manganites, nickelates, and cobaltites; valley symmetry breaking systems like single and bilayer graphene, elemental bismuth, and AlGaAs 2DEG's, as well as strontium ruthenates and iron pnictides. [82, 83] For electron nematics with XY symmetry [49] there is a factor of two between the physical angle of the nematic in the plane, and the natural angles in an XY model. This is because a nematic is symmetric under 180^o rotation, whereas the XY spins change sign under the same operation. The uniaxial random fields we discuss in this paper can arise in these systems if random orienting fields are strong only along the major crystalline axes. Note that in this case, the order-by-disorder transition would induce the electron nematic to orient along a direction which is diagonal to the major crystalline axes.

Several external perturbations can be used as a driving field on an electron nematic, including magnetic field, electric field, high currents, and uniaxial stress. [56,84] Note that similar symmetry considerations apply to the driving field in these systems. For example, a rotating applied magnetic field $\vec{B} = [B_x, B_y] = B[\cos(\omega t)), \sin(\omega t)]$ can be used to exert the rotating driving field of Equation (1.1) for the case of a

nematic, with the caveat that rotating the applied field by 90^o changes the sign of the driving field:

$$\vec{H} = [H_x, H_y] = H[\cos(2\omega t), \sin(2\omega t)] \ . \tag{3.3}$$

3.5.2 Quantum Gases

Random-field induced order has been proposed to happen in coupled Bose-Einstein condensate systems. [9] Theoretical and numerical results on two-component Bose gases predict that by using a Raman field to couple two internal states, uniaxial random field disorder can be produced. The uniaxial nature is achieved by a Raman coupling with a constant phase, while the randomness is achieved through random strength of the Raman field. [11, 85] Similarly, a rotating driving field can be applied by a Raman coupling with uniform strength, but a rotating phase.

3.5.3 Magnetic systems

While the mapping of a magnetic system with XY symmetry to Equation (1.1) is clear, the realization of a uniaxial random field in these systems is less clear. It may be possible to design a system in which epitaxial strain from a substrate exerts random uniaxial fields on a 2D XY ferromagnet through a magnetoelastic coupling.

3.6 Methods

3.6.1 Hysteresis Protocol

The magnetization m_y in the y-direction at intermediate disorder strength $R_x = 0.5J$ remains ordered even in the presence of weak applied transverse field H_x. (See Section 1.2) Therefore, to begin the hysteresis studies, we first initialize the system in a y-magnetized state, by starting from the fully saturated y magnetization, with the driving field aligned along y, $\vec{H}||y$, then allow the system to relax [58] at that applied field. We take the angle ϕ of the applied field to be $\phi = \text{Arctan}(H_y/H_x)$, so

the initial direction of the applied field is $\phi = \pi/2$. After rotating the applied field by an amount $\delta\phi(\vec{H})$, the spin configuration is updated successively so as to minimize the energy, in the $\omega \to 0$ limit. After a transient response, the response of the system then settles into a limit-cycle.

Each time the applied field direction is updated, the energy is minimized on each site by aligning the spin on each site with its effective field, $\vec{h}_i^{eff}$. Hence the following update strategy is repeated until the spin configuration converges to the nearest energy minimum:

$$\begin{aligned} \vec{h}_i^{eff}(t) &= J \sum_{j \in \langle i,j \rangle} \vec{S}_j(t) + \vec{h}_i + \vec{H}, \\ \vec{S}_i(t+1) &= \frac{\vec{h}_i^{eff}(t)}{|\vec{h}_i^{eff}(t)|} \end{aligned} \tag{3.4}$$

This update mechanism is similar to Equation (2) of Ref. [86], however the effective on-site field in our case includes only the instantaneous influence of nearest neighbors, whereas Ref. [86] is working in a mean-field limit. The update algorithm we employ is described in more detail below, in section 3.6.2.

We continue to allow spins to relax under the influence of Equations (3.4) until a limit-cycle is reached, defined by $\{\vec{S}_i\}(\phi + 2\pi n) = \{\vec{S}_i\}(\phi)$. We use the following parameters in our simulations: $\delta m_{cutoff} = 10^{-4}$, $\delta\phi_{max} = 2\pi \times 10^{-4}$, $\delta\phi_{min} = 2^{-14} \times \delta\phi_{max}$. Hence the avalanches ($\delta m$) are only well-defined within the precision of the driving field angle, $\delta\phi_{min} = 2\pi \times 6.1 \times 10^{-9}$.

3.6.2 Spin Relaxation Method

The rotation of the driving field and subsequent relaxation of the spin configuration is performed as follows. Starting from an initial spin state $\{\vec{S}_i\}(\phi)$ for a given applied field direction $\phi = \text{Arctan}(H_y/H_x)$ and with $\delta\phi$ initially set to $\delta\phi = \delta\phi_{max}$:

1. Update $\phi \to \phi + \delta\phi$.

2. Use Equations (3.4) to relax the spin configuration.

3. If $\delta m > \delta m_{cutoff}$, then:

   (a) If $\delta\phi = \delta\phi_{min}$, accept the new spin configuration and the new ϕ, and proceed to Step 1

   (b) Else reject the changes. Set $\delta\phi \to \delta\phi/2$ and proceed to Step 1

4. Else accept the new spin configuration and the new ϕ, and:

   (a) If $\delta\phi = \delta\phi_{max}$ or $\delta m \geq \frac{\delta m_{cutoff}}{2}$, proceed to Step 1.

   (b) Else, set $\delta\phi \to 2 \times \delta\phi$ and proceed to Step 1.

3.6.3 Disorder Averages

Table 3.2 reports the number of disorder configurations used in Figs. 3.3, 3.4, and 3.5.

Table 3.2.
Number of disorder configurations used in Fig. 3.3 (a) and (b), Fig. 3.4(d), and Fig. 3.5 (a-e).

Size ($N = L \times L$)	Configurations
64×64	75
80×80	60
100×100	50
128×128	40
160×160	30

3.7 Conclusions

In conclusion, we have shown that the order-by-disorder transition of the two-dimensional XY model in the presence of a uniaxial random field persists up to a

critical strength of the rotating driving field. Near the critical driving field strength, the response of the system has a period which is an integer multiple $n > 1$ of the driving field period. The trend with increasing system size is toward increasing period n, suggesting the onset of what is effectively non-repeatability as $n \to large$ in the thermodynamic limit. Similar multi-period cascades signal the onset of chaos in nonlinear systems, and signal the onset of irreversibility in periodically driven models of plastic deformation, suggesting that multi-period cascades are characteristic of a larger class of transitions in dynamical systems. Our results further indicate that the period n can be engineered to remain finite if the thermodynamic limit is taken by tiling a particular disorder pattern into a superlattice. In this case, behavior reminiscent of classical discrete time-crystals emerges near criticality.

4. CLASSIFYING SURFACE PROBE IMAGES WITH NEURAL NETS

4.1 Introduction

The types of surface probes, e.g. atomic force microscope (AFM), scanning tunneling microscope (STM), scanning near-field optical microscope (SNOM), scattering scanning near-field infrared Microscope (s-SNIM), and more, [18, 19] and the wealth of data they generate is increasing at a rapid pace, where current classification techniques involve human intervention making the process time-consuming. Automation of this process will help researchers gain insights spending as little time as possible on classification. With the progress in Deep Learning and its broad applicability, it has become a highly used tool in diverse fields. Convolutional neural networks are heavily used in image classification. Lukasz *et al.* has shown that with machine learning, images from simulation can be classified with very good accuracy of $\sim 97\%$. [22] Here we show that a deep learning architecture can classify 2D surface images into one of the 2D/3D clean Ising models, 2D/3D random field Ising models, or 2D/3D percolation models to even better accuracy ($> 99\%$). Furthermore, we have customized the model with symmetry transformations and rejection criteria, which can handle many anomalous predictions. We apply this framework to experimental data to demonstrate its potential.

4.2 Simulations

We consider clean Ising models, random field Ising models (RFIM), and uncorrelated percolation models to generate lattice configurations, which will be used as training examples in section 4.3.

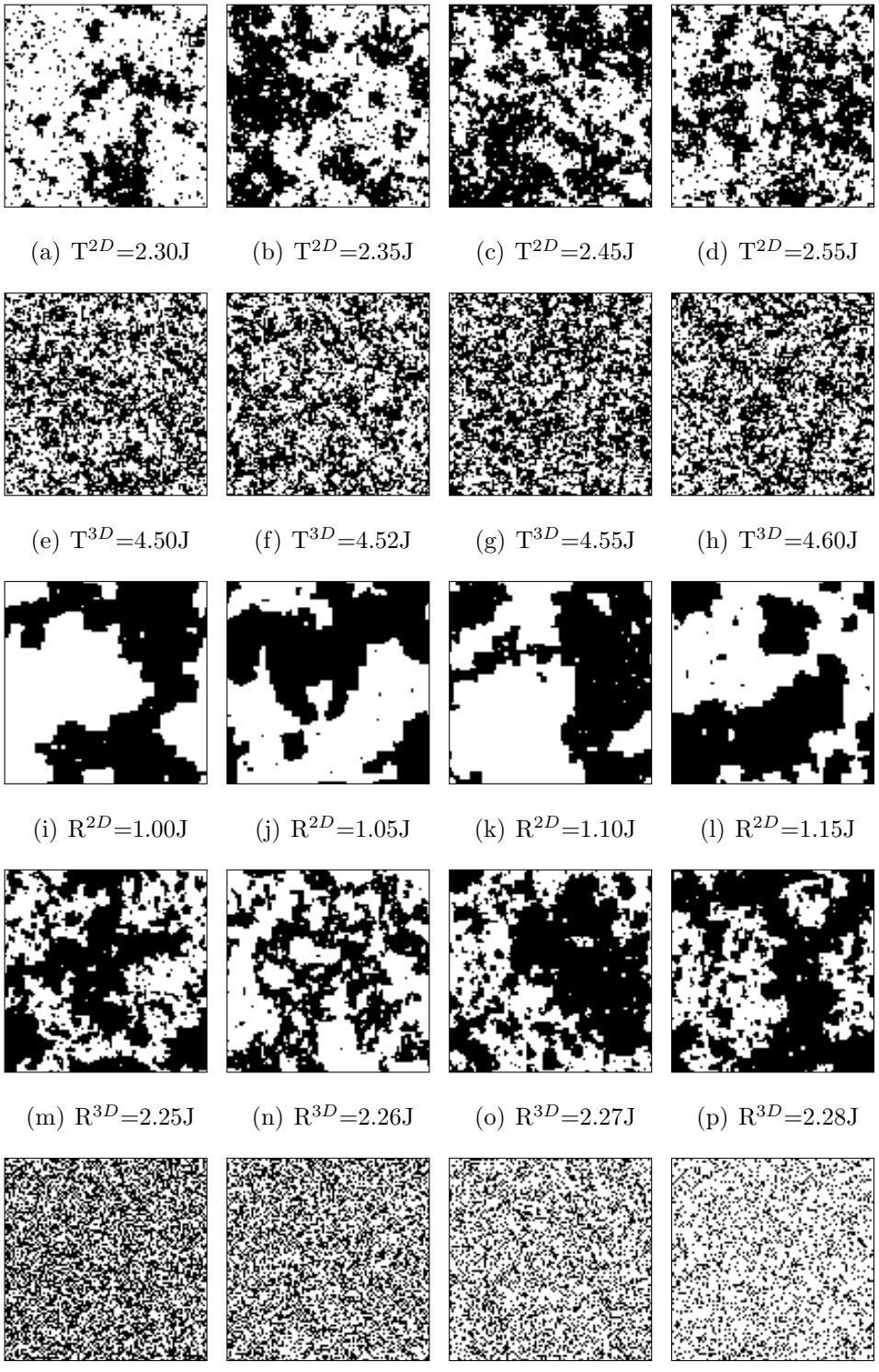

(a) T^{2D}=2.30J (b) T^{2D}=2.35J (c) T^{2D}=2.45J (d) T^{2D}=2.55J

(e) T^{3D}=4.50J (f) T^{3D}=4.52J (g) T^{3D}=4.55J (h) T^{3D}=4.60J

(i) R^{2D}=1.00J (j) R^{2D}=1.05J (k) R^{2D}=1.10J (l) R^{2D}=1.15J

(m) R^{3D}=2.25J (n) R^{3D}=2.26J (o) R^{3D}=2.27J (p) R^{3D}=2.28J

(q) p=0.50 (r) p^{2D}=0.59 (s) p^{3D}=0.69 (t) p=0.80

Figure 4.1. Critical configurations generated from simulations of different Ising models and percolation models.

The Hamiltonian of the clean Ising model is given by equation 2.36 with $\sigma_\phi = 1$. Where, $\sigma_i \in \{+1, -1\}/\{1, 0\}/\{\uparrow, \downarrow\}$ is a two-state local order parameter. This model undergoes a phase transition at a critical temperature of $T_c^{2D} \approx 2.27J$ in two-dimensional systems and $T_c^{3D} \approx 4.51J$ in three-dimensional systems. [48, 87] The simulation consisted of a mixture of Monte-Carlo updates with checkerboard Metropolis and Wolff algorithms to thermalize and generate images near the critical temperature. Figures 4.1(a-d) shows some configurations near and above T_c^{2D} on a 100×100 lattice. Figures 4.1(e-h) shows some configurations near and above T_c^{3D} on the surface of a $100 \times 100 \times 100$ lattice.

The random field Ising model (RFIM) is used to model the disorder in the Ising system as given in equation 3.1. Where most of the variables can be identified with the Ising model Hamiltonian (Eqn. 2.36 with $\sigma_\phi = 1$). In this model, the uniform field h and the local random fields h_i couple with the local order parameter. The random fields are chosen from a Gaussian distribution of strength R where, $P(h_i) \propto \exp(-h_i^2/(2R^2))$. At zero-temperature, this model undergoes a non-equilibrium phase transition at a random field strength of $R \approx 2.16J$ in a three-dimensional system (3D-RFIM) and $R \to 0$ in a two-dimensional system (2D-RFIM). [88] This model was simulated at zero-temperature while sweeping the field h. The most striking patterns form near the coercive field, hence used for training examples for the Neural Net. Figures 4.1(i-l) shows some configurations at the lowest possible disorder strengths on a 100×100 lattice. For a small system, finite-size effects play a key role in pushing the critical field strength to a higher value. Figures 4.1(m-p) shows configurations at the lowest possible disorder strengths on the surface of a $100 \times 100 \times 100$ lattice.

In the uncorrelated percolation model, a site is occupied with a probability p. It is the same as flipping a biased coin where p is the probability of turning up heads. The percolation threshold (critical percolation probability, p_c) is marked by a percolating cluster spanning over the system. In a two-dimensional system this threshold occurs at $p_c^{2D} \approx 0.59$ and in a three-dimensional system at $p_c^{3D} \approx 0.31$. [89] Figures 4.1(r) shows a critical configuration of 100×100 sized 2D percolation. Figures 4.1(s) shows

a critical configuration of a slice in $100 \times 100 \times 100$ 3D percolation. As we shall see in section 4.3.1, configurations generated by the black↔white symmetry transformations are equivalent, hence this represents a configuration generated from critical 3D percolation at $p = 0.31$.

Configurations generated from all other percolation probabilities were put in a separate class. This helps in separating the interesting patterns in the above models near criticality from the images which are mostly black or mostly white (Fig. 4.1(t)) and random noise (Fig. 4.1(q)).

Table 4.1.

Simulation details.

Model	T/J	R/J	p	Type
2D Clean Ising	$2.25 - 2.64$	0	N/A	Monte-Carlo
3D Clean Ising	$4.45 - 4.65$	0	N/A	Monte-Carlo
2D RFIM	0	$1.00 - 1.19$	N/A	Zero-Temperature
3D RFIM	0	$2.25 - 2.29$	N/A	Zero-Temperature
2D Percolation	N/A	N/A	0.57-0.61	Biased coin flip
3D Percolation	N/A	N/A	0.29-0.33	Biased coin flip
	N	N	0.02-0.2	Biased coin flip
Other Percolation	/	/	0.48-0.52	Biased coin flip
	A	A	0.8-0.98	Biased coin flip

4.3 Customized Deep Learning Model

In order to detect a critical configuration of the above models, we simulate them near their respective transitions and feed the results into a deep neural network that specializes in pattern recognition in images. Our approach is geared towards equipping researchers dealing with high volumes of data from surface probes that can be

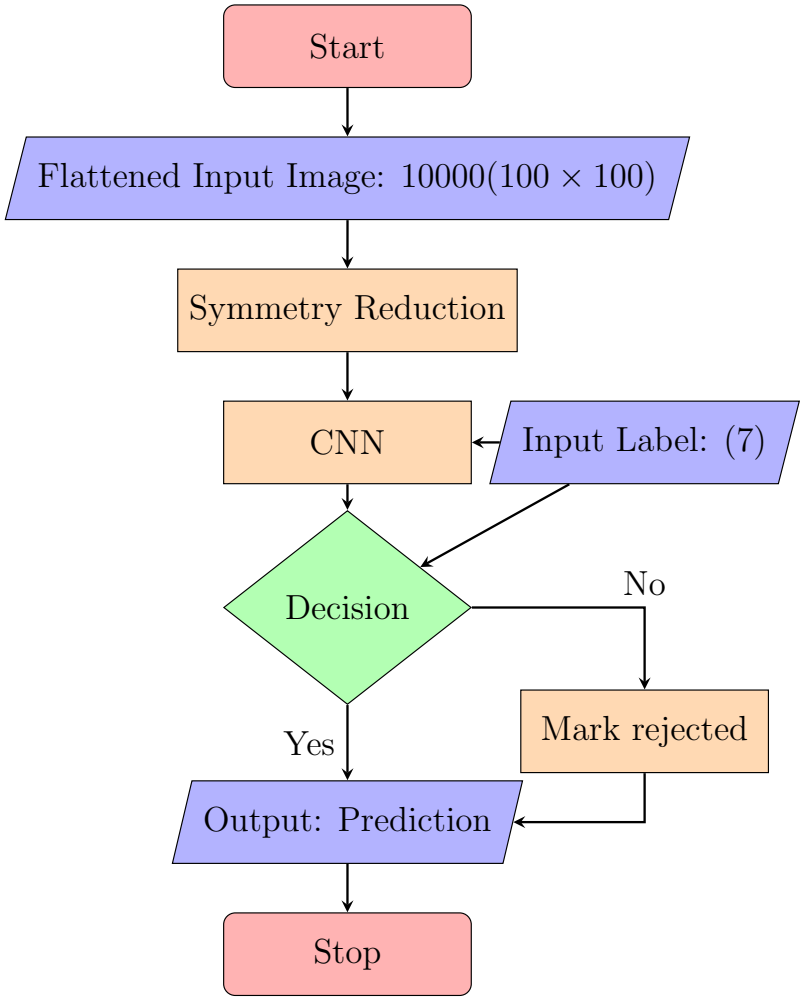

Figure 4.2. End-to-end Classification flowchart with CNN. Here we highlight where the non-trainable part of the classification. The symmetry transformation layer is added which acts on the training dataset and while testing the classification as well. These operations (See Fig. 4.3) has the advantage of reducing the amount of data required to train the network as well as provide one crisp prediction given any one of the 16 possible configurations of a single image. The simulated images and their corresponding labels are provided as training and validation data for the deep learning models (Fig. 4.4). After training, the output distribution from the CNN for all the known classes are stored for a further test which checks whether the prediction class determined from the maximum of 7 unit CNN-output is close to the distribution in the training set, otherwise, it is marked as rejected.

classified into one of these models. Traditional approaches, like the one described in Ref. [20,23,90], are more time consuming and require expert knowledge in the matter. Here, we train a Convolutional Neural Network (CNN) to classify a 2D image into any one of the above models discussed above. For generating 2D images from three-dimensional models we used slices and surface configurations, with an open boundary condition (along one of the axes) for the Ising models. We generate simulation results from 100×100 (2D) and $100 \times 100 \times 100$ (3D) lattice size systems.

The parameters from table 4.1 are used to generate 8000 images for each model near its transition. A percolation probability away from 2D and 3D critical percolation strengths contribute to 16000 images. This dataset is curated by taking all the 16 symmetry operations and passing it through the symmetry reduction, keeping only the unique configurations.

4.3.1 Symmetry Operations

Let us turn our attention to the symmetry operations in effect. These 16 symmetry operations that can be applied to any square image. Most of the 16 transformations can be mapped to a single configuration. This is utilized to our advantage for training and validation without loss of generality:

1. Ising symmetry(2): $\{+1, -1\} \leftrightarrow \{-1, +1\}$. If a configuration has majority down spin, flipping them makes them majority spin up.

2. Rotation(4): Rotate by $\pi/2, \pi, 3\pi/2$. The quadrant (numbered cyclically) which has the most spin up is rotated to become the 1st quadrant.

3. Transpose(2). The quadrants with the most spin up between 2nd and 4th (diagonally opposite) becomes the 2nd quadrant with the help of transpose operation.

All the above operations are performed in the given order and the logic is summarized in Fig. 4.3. There are some configuration which cannot be mapped to a single

configuration using these symmetry operations. For example, if exactly half the spins are up, the first step cannot reduce it down to a unique configuration. But the possibility of that occurrence is $\frac{^{N}C_{N/2}}{2^N} \approx 1.592 \times 10^{3008}/1.995 \times 10^{3010} \approx 0.008$. But this is accounted for when we take all the 16 symmetry operations on a configuration and apply the reduction operations to keep only the unique configurations.

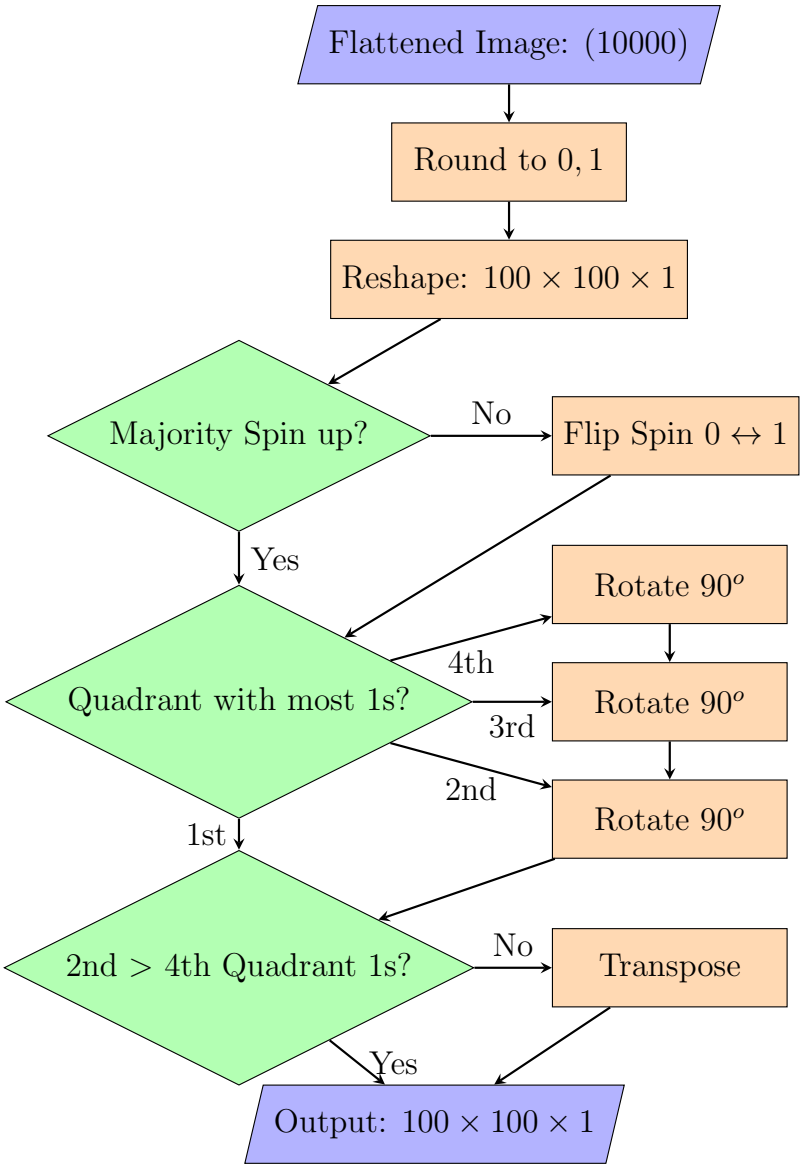

Figure 4.3. Symmetry reduction method.

4.3.2 Convolutional Neural Net Arcitecture

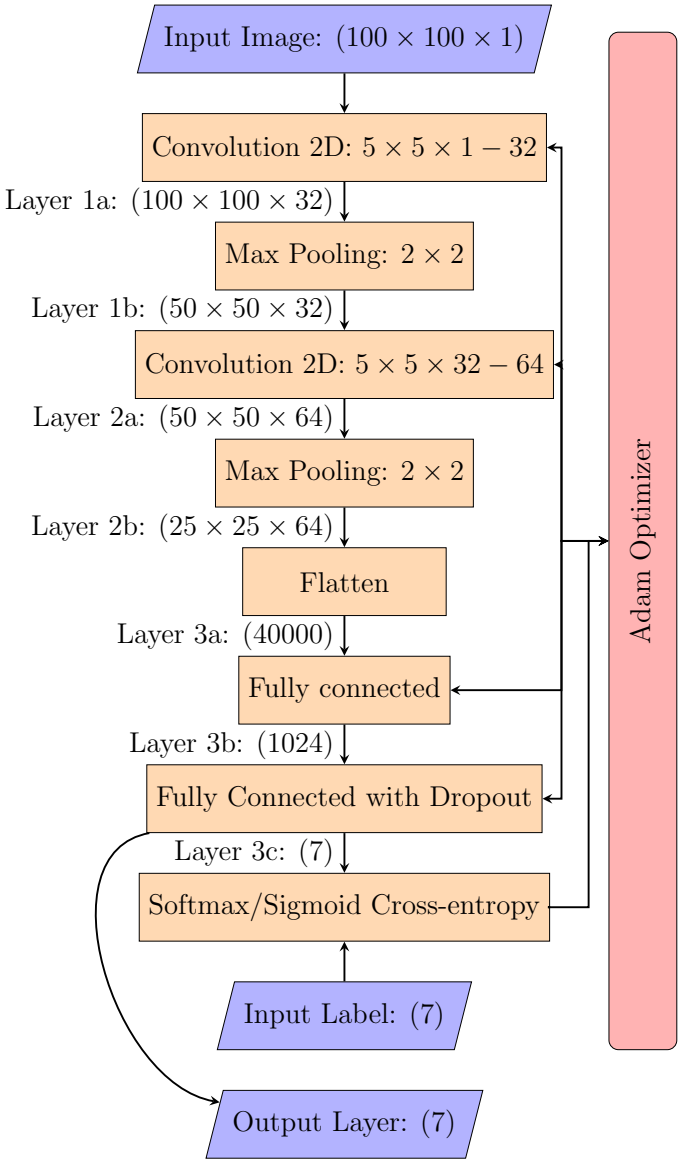

Figure 4.4. Convolutional Neural Network. The input image here is reduced by the symmetry operations given in Fig. 4.3. We use ADAM (Adaptive moment estimation) optimization algorithm to train the network. [91] The output labels/probability is determined using sigmoid/softmax on the output layer.

The convolutional neural net (CNN) consists of two 2D convolution layers and max-pooling layers followed by two fully connected layers resulting in seven-dimensional output classes for classification. This base model is trained with two different activation functions on the output layer based on the type of classification required:

- Using a softmax activation layer on the final output layer would result in a single label classification, if there are n output classes with numbers v_i the softmax is defined as:

$$Y_i^{softmax} = \exp(v_i) / \sum_{j=1}^{n} \exp(v_j) \tag{4.1}$$

  where, $Y_i^{softmax}$ is the output probability/likelihood estimate.

- Whereas a sigmoid activation layer would result in a multi-label classification. The sigmoid is simpler in the sense that it assigns a probability irrespective of the other classes:

$$Y_i^{sigmoid} = 1/(1 + \exp(-v_i)) \tag{4.2}$$

  where, $Y_i^{sigmoid}$ is the output probability/likelihood estimate.

The simulation results after the symmetry reduction is divided into a training set and a validation set. The training set is used to train the network whereas the validation set is used for testing generalization error. A saturating validation error during training roughly marks the onset of overfitting. Figure 4.5 shows that the classification errors are less than 0.5% for both activation functions (softmax and sigmoid).

4.3.3 Rejection Criteria

After training this model, we devised and implemented a method for rejecting the final prediction based on the distribution at the output layer before the softmax/sigmoid activation. Figure 4.6 shows distribution of the output before the final activation layer. Since this distribution is well clustered in the six critical models

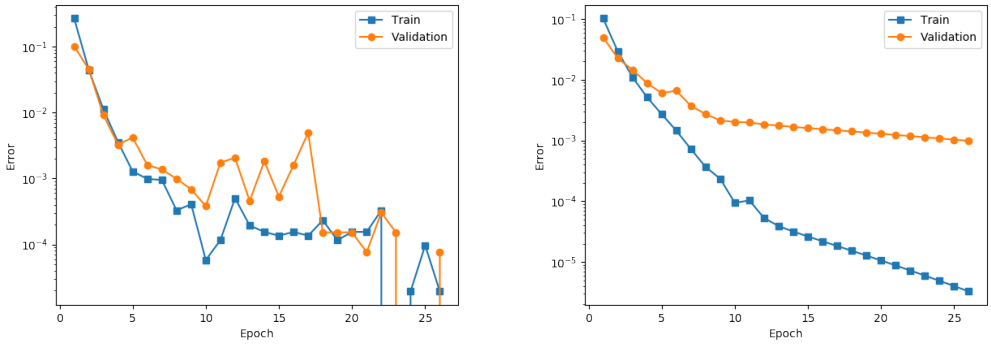

(a) Error from softmax activation

(b) Error from sigmoid activation

Figure 4.5. Error in the training and validation set vs. the number of epochs. Epochs correspond to the number the times the training set went through a training process. (a) Softmax activation(Eqn. 4.1): To prevent overfitting we chose epoch=4 for testing with experimental images. Training/Validation accuracy = 99.64%/99.67% (b) Sigmoid activation(Eqn. 4.2): To prevent overfitting we chose epoch=9 for testing with experimental images. Training/Validation accuracy = 99.97%/99.79%

of interest, a prediction point lying far from its corresponding cluster is marked as an anomaly. For each class, a distribution of the output layer is generated from the training examples. The validation process confirms that the optimum deviation from the training distribution is given by the standard deviation in each output dimension. The generalization of this method would be to use any or all of the intermediate layers for detecting such an anomaly in the input data, see Ref. [92].

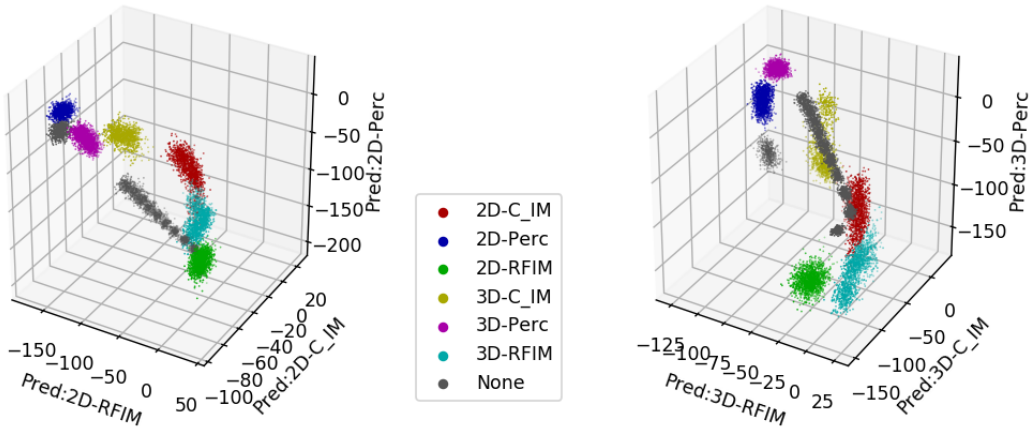

(a) Distribution in layer before softmax.

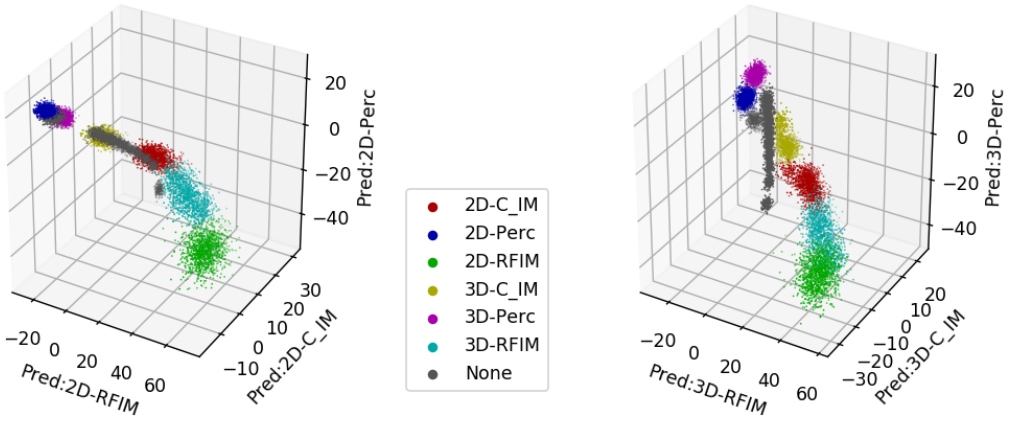

(b) Distribution in layer before sigmoid.

Figure 4.6. The distribution of values in the pre-final layer of each class. As we can see that they cluster near specific values, they can be used to reject any prediction which does not lie sufficiently close to any of these values.

4.4 Application to experimental images

We procured some experimental images which are a good candidate for these models. The image sizes from experiments can be of any size. To use our framework

which was trained on 100×100 images, we can scale it down close to our target size. Since it is best to look at the largest possible length scales we do a block renormalization for black and white images larger than $100(2n+1) \times 100(2n+1)$ of unit cell size $(2n+1) \times (2n+1)$. For grayscale images, we can reduce it by $n \times n$ by averaging and then setting a threshold. The resulting image can go through the classification process if we use a sliding window (like a convolution) over the image. The generated prediction from all of these are averaged into a single result.

The images in figures 4.7, 4.8, 4.10 and 4.12 were obtained from Ref. [23]. The data was collected using s-SNIM on a sample of vanadium dioxide (see section 1.3). A rigorous scaling analysis is available in Ref. [23]. In this part, we were provided with grayscale images of size 256×256, hence were able to scale it down to 128×128 by averaging over 2×2 pixels.

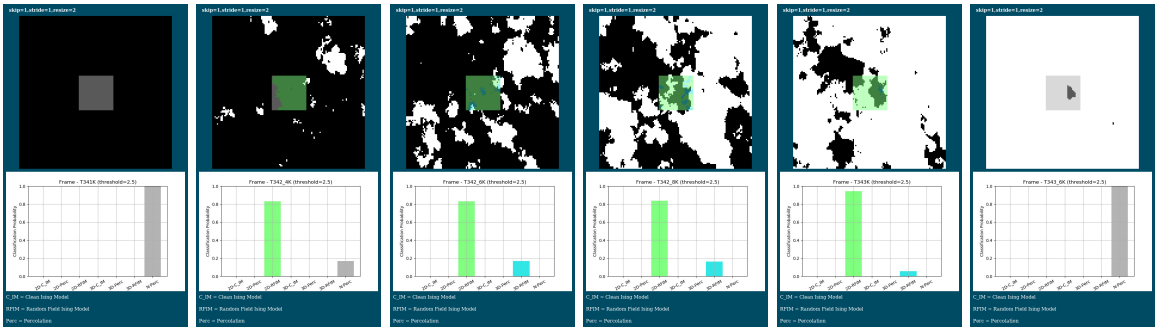

(a) $T = 341.0$K (b) $T = 342.4$K (c) $T = 342.6$K (d) $T = 342.8$K (e) $T = 343.0$K (f) $T = 343.6$K

Figure 4.7. Classification from deep learning model with softmax activation which specializes in categorizing into one label. The test images from a scanning near field microscopy on a sample of VO_2 in the metal-insulator transition regime. The images were downscaled by a factor of two. The resulting image was thresholded using the same threshold that as in Ref. [23]. The outcome is expected to be in RFIM. And since these are planar material 2D RFIM is correctly predicted by our deep learning model. The color-coded overlay is placed on the black and white images to show their corresponding classification. Only one center pixel of a 100×100 window is colored by using this method. And we do the same classification by shifting this window by 1 pixel in either right or down. The probability estimates are averaged over all the predictions into a single prediction probability in the bar chart.

Figure 4.7 shows the results of classification with the CNN trained with a single-label (Eqn. 4.1) classifier. The positive detection for 2D-RFIM is generated for the Figure 4.7(b-e).

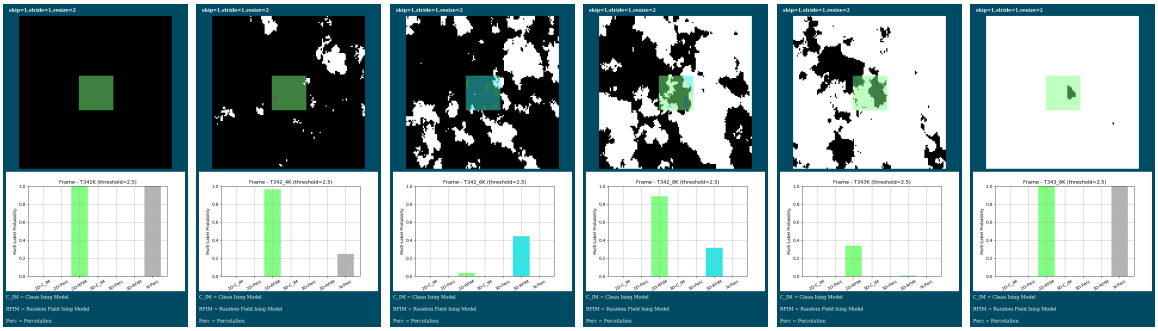

(a) $T = 341.0$K (b) $T = 342.4$K (c) $T = 342.6$K (d) $T = 342.8$K (e) $T = 343.0$K (f) $T = 343.6$K

Figure 4.8. Classification from deep learning model with sigmoid activation which specializes in assigning to probability for multiple classes. The test images are the same as figure 4.7. The outcome is expected to be in RFIM. And since these are planar material 2D RFIM is correctly predicted by our deep learning model. A color-coded overlay is placed on each black and white image to show their corresponding classification. Only one center pixel of 100×100 window is colored by using this method. And we do the same classification by shifting this window by 1 pixel in either right or down. The probability estimates are averaged over all the classifications into a single prediction probability in the bar chart.

Figure 4.7 shows the results of classification with the CNN trained with a multi-label (Eqn. 4.2) classifier. The positive detection for 2D-RFIM is generated for all except Figure 4.7(c). This was not expected as the completely black image was given a high chance of falling in 2D-RFIM.

Can the Rejection Criteria do better?

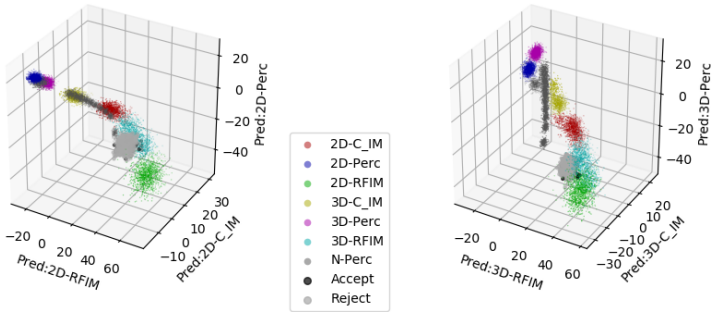

(a) $T = 342.6$K

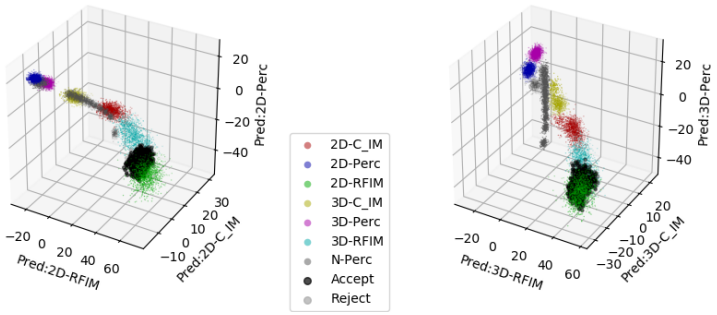

(b) $T = 342.8$K

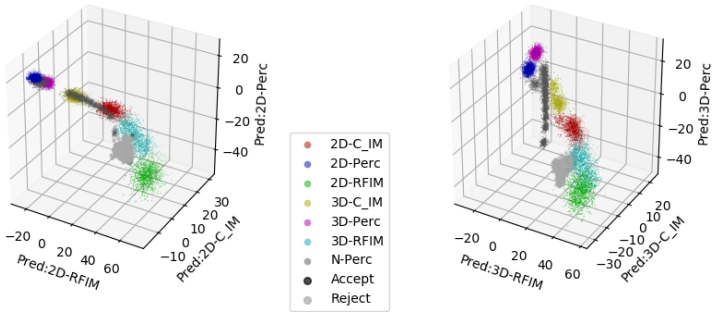

(c) $T = 343.0$K

Figure 4.9. Pre-final layer of CNN before softmax activation(Eqn 4.1). The light gray spots in the figure represent predictions that need to be rejected based on the displacement from the predicted cluster in Sec. 4.3.3. The black spots are the predictions that are accepted. We will see in figure 4.10 how this affects the predictions generated.

We show the distribution in the pre-final layer of the CNN when the test images in figure 4.7(c-e) are passed through the network trained with a softmax activation (Eqn. 4.1), in figure 4.9. In this case, the rejection criteria were able to filter out images that were away from the 2D-RFIM cluster in the training set. In figure 4.10 we demonstrate the rejection criteria on the four images that were predicted as 2D-RFIM to very high possibility. The effect is clear since the only test image surviving the rejection criteria was taken at T=342.8K(Fig. 4.10(c)). Hence, the basis of rejection was able to nail down the test image which was most likely to be in the 2D-RFIM (See Fig. 4.10(c)).

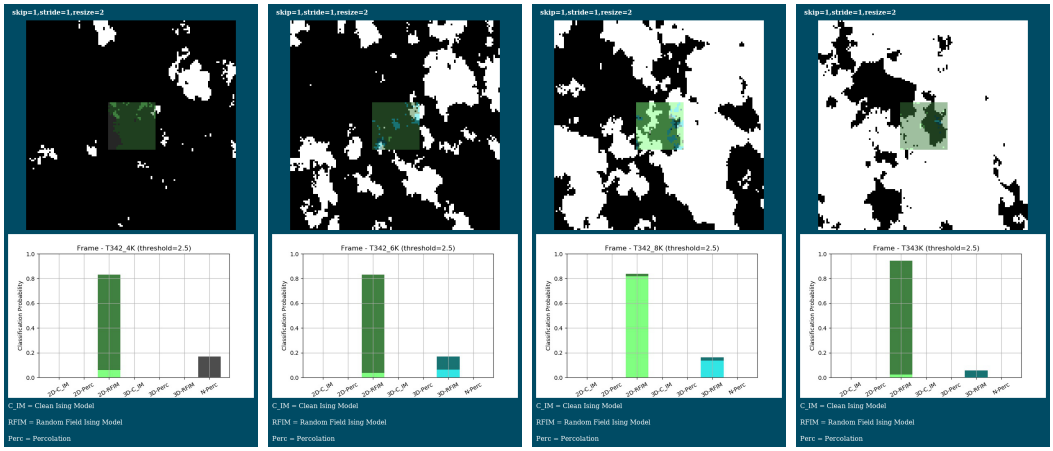

(a) $T = 342.4$K (b) $T = 342.6$K (c) $T = 342.8$K (d) $T = 343.0$K

Figure 4.10. Description same as figure 4.7. The darker colors are from predictions that did not pass the rejection criteria as described in section 4.3.3.

Figure 4.11 shows the distribution of the pre-final layer before the sigmoid activation (Eqn. 4.2) for the test images in figure 4.8(c-e). Firstly, the completely black image classified into 2D-RFIM, is discarded as a badly classified image. In Fig. 4.12(c) the prediction likelihood of 2D-RFIM and 3D-RFIM was reduced, with 2D-RFIM still the better candidate. But in figure 4.12(b) we see 3D RFIM is detected with a small

likelihood. The rejection suppressed more than half of these predictions in the 3D-RFIM. For the rest of the badly classified test images, the rejection criteria handled it quite well.

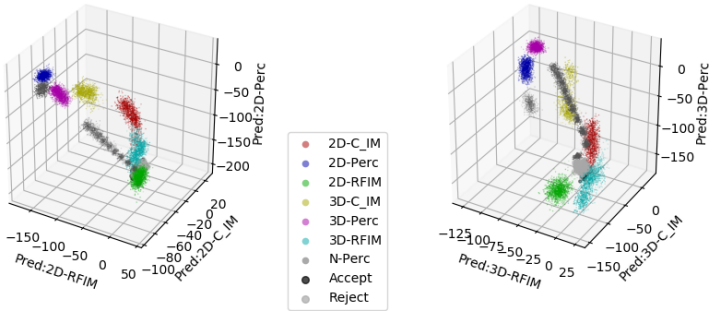

(a) $T = 342.6$K

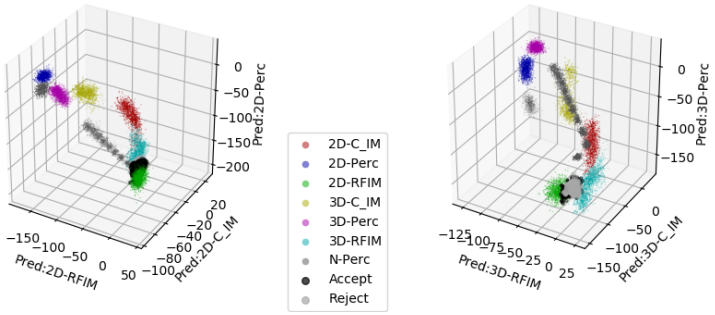

(b) $T = 342.8$K

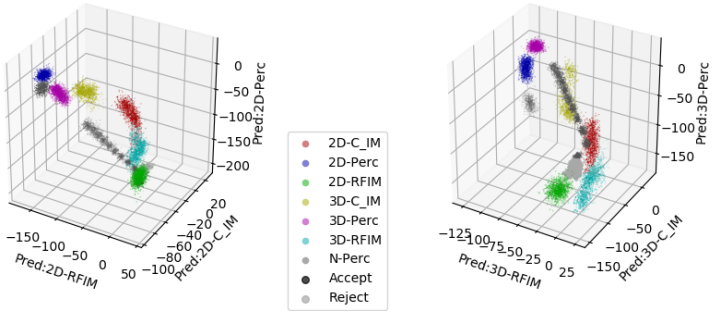

(c) $T = 343.0$K

Figure 4.11. Pre-final layer of CNN before sigmoid activation(Eqn 4.2). The light gray spots in the figure represent predictions that need to be rejected based on the displacement from the predicted cluster in Sec. 4.3.3. The black spots are the predictions that are accepted. We will see in figure 4.12 how this affects the predictions generated.

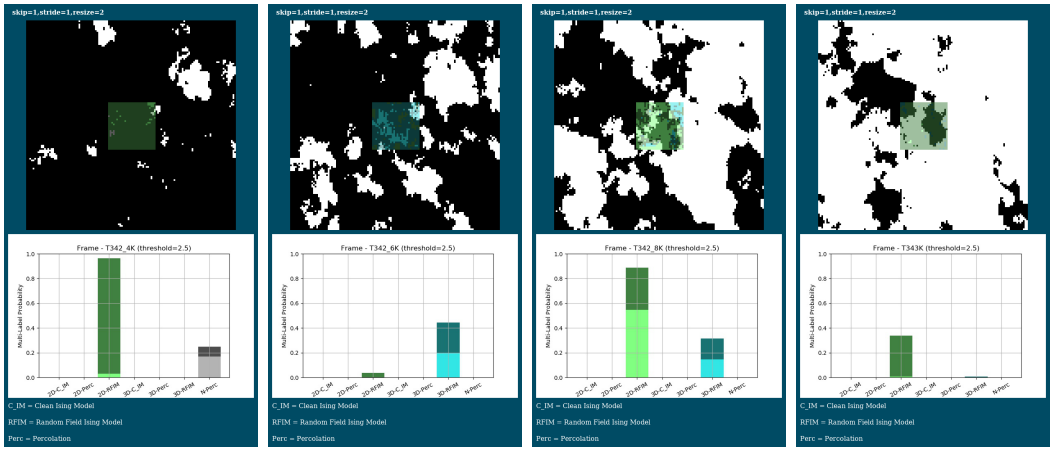

(a) $T = 342.4$K (b) $T = 342.6$K (c) $T = 342.8$K (d) $T = 343.0$K

Figure 4.12. Description same as figure 4.8. The darker colors are from predictions that did not pass the rejection criteria as described in section 4.3.3.

Both the methods gave a larger positive identification for the 2D-RFIM (Fig. 4.10(c) and Fig. **??**(c)). This strengthens our confidence in this classification method, where for all other temperatures almost all of the classification of the Ising model is rejected by our final decision criteria (Fig.4.10(a,b,d) and Fig.4.12(a,b,d)). Although the softmax still has a small edge over the sigmoid activation with less spurious detections.

Experimental images in figure 4.13 is obtained from Alexandre Zimmers Lab at ESPCI, where they used an optical microscope on VO_2 film to measure the local reflectance of the surface. First, let's discuss some details about the experimental setup. A 130nm VO_2 thin film was deposited by rf magnetron sputtering on an r-cut sapphire substrate. Gold electrodes separated by 20μm were deposited on top of the film. The sample showed a clear insulator to metal transition above 68^{o}C by four orders of magnitude drop in its resistivity. [93] The optical experimental setup consists of placing this VO_2 thin film sample on a Peltier heater inside a microscope. Surface reflection images were taken in the visible range with a $\times$150 magnification dry Olympus objective lens with an optical aperture of 0.9 and a focal point of 1mm.

The temperature was typically cycled from 55^{o}C to 75^{o}C around the metal to insulator transition. Inevitable temperature dilation of the Peltier heater brought the sample out of focus while heating:

- To compensate the z drift the sample was moved up and down 10μm periodically (period$\sim$10s) by a piezoelectric crystal under it to bring the sample in and out of focus. In the post-experiment analysis, among the 62000 images recorded during the 14-hour experiment (3 major temperature loops and 10 subloops), 895 images were selected to be in focus by pinpointing the minimum compression ratios.

- Thermal drifts in the x-y plane were compensated post-experiment, using Adobe Premiere Pro program.

How we converted these images from grayscale to black-and-white is by observing that each pixel intensity changed from a high saturation value (I_{max}) near T=55^{o}C to a low saturation value (T_{min}) near T=75^{o}C in a rounded step-like manner. Hence we define a single-pixel-turnon intensity independent of the other pixels at $\frac{I_{min}+I_{max}}{2}$.

Figure 4.13, shows the performance of the two networks with the decision criteria to handle bad predictions. Both of our neural nets identified these as 2D RFIM. The CNN with softmax(Fig. 4.13(a)) activation distinctly identified 2D-RFIM for this image. Whereas the predictions from CNN with sigmoid(Fig. 4.13(b)) activation identified both 2D and 3D-RFIM, with 2D-RFIM being the more likely candidate. The rejection criteria suppressed predictions from both 2D/3D RFIM, making both the predictions suppressed. The 2D-RFIM beats the 3D-RFIM with a very low margin. Hence, some skepticism is justifiable for this CNN. But the model trained with a softmax activation performs significantly better than the sigmoid.

4.5 Conclusion

We have shown the accuracy that can be achieved by using a convolutional neural net to classify simulated images is better than 99%. We also demonstrate that this

framework can be applied to real experimental images. The CNN model trained with a softmax activation (See Eqn. 4.1) performs better on experimental images than the sigmoid activation (See Eqn. 4.2). The symmetry reductions significantly lower training time by reducing the size of the input data without reducing accuracy. The implementation of a distribution based rejection method makes prediction more precise. But, some fine-tuning may be required before going into production. The future scope of this framework is huge, we list a few here: (1) generalize the CNN to handle inputs of any size, (2) a learning-based optimization for the rejection classifier, (3) a regression-based algorithm may be used to detect critical parameter for each model, (4) handling grayscale images without the need to threshold them, and more. Since this deep learning model can be trained on simulated data and/or classified experimental data, it will be a significant boost in detecting the underlying physics from 2D data.

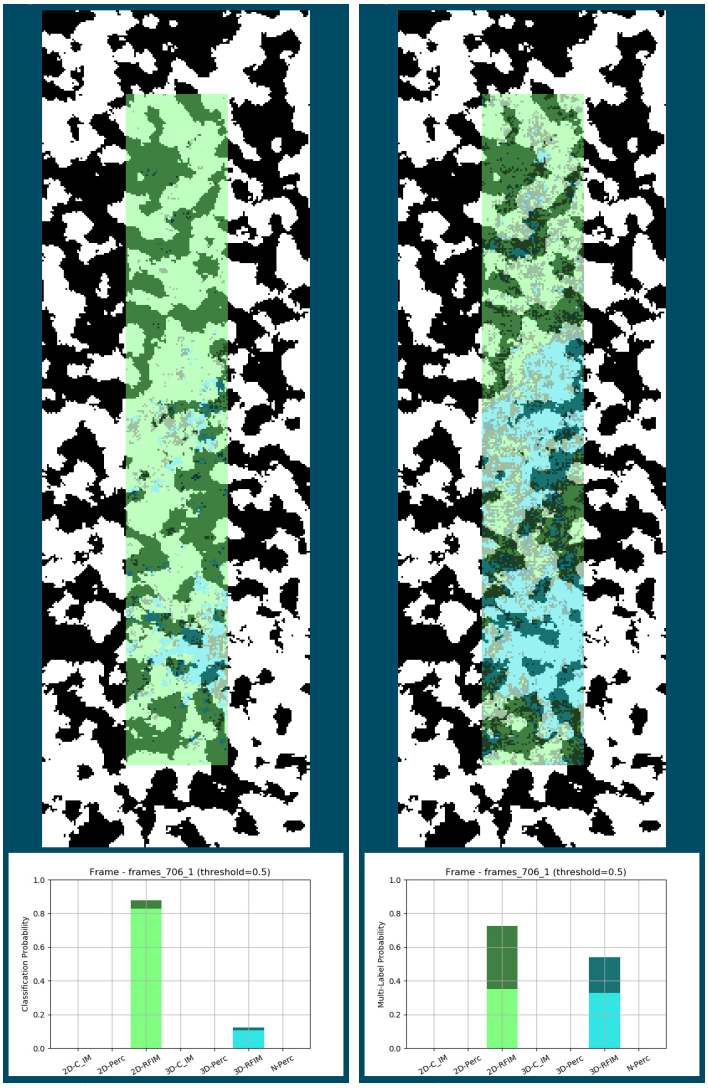

(a) Prediction from CNN with Softmax.

(b) Prediction from CNN with Sigmoid.

Figure 4.13. These images are from a series of images undergoing a Metal-Insulator phase transition, where all the pixels saturate individually to a different minimum(I_{min}) and a maximum(I_{max}) intensity. The intensity of each pixel was scaled from $[I_{min}, I_{max}] \rightarrow [0, 1]$. The threshold was then set to 0.5. This image was taken at T=62.8^{o}C. Classification with deep learning model with (a) Softmax activation, and (b) Sigmoid activation. The bright green/cyan colors, in both the bar plot and the overlay, indicate 2D-RFIM/3D-RFIM classification, respectively, that passed the rejection criteria. Whereas the bright green/cyan colors indicate the rejected classifications. The predicted possibility for each category is shown in the bar plots.

5. SUMMARY

In chapter 2, we have shown that the entire temperature dependence of the observed resistivity anisotropy in NQHM at $\nu = 9/2$ can be well described by taking into account the discrete rotational symmetry of the underlying crystal. We expect similar temperature evolution to occur for $\nu > 9/2$ half-integer fillings, and also for the $\nu = 5/2$ and $7/2$ states which display anisotropic resistivity upon application of a moderate in-plane field. Inclusion of such a symmetry-breaking term shifts the universality class of the electron nematic from the Kosterlitz-Thouless universality class of the two-dimensional XY model to the two-dimensional Ising universality class. We furthermore propose an experimental test for hysteresis that can clearly distinguish whether any 2D electron nematic is in the Ising or XY (Kosterlitz-Thouless) universality class.

In chapter 3, we see that the role and type of quenched disorder is important. The disorder causes both random fields as well as random bonds. In presence of both, the universality class is set by random field disorder as it is relevant in both cases. Random field disorder in an infinite system with an applied field leads to the same universality class in both models. For a random field XY model in $d < 4$ and for a random field Ising model in $d \leq 2$, macroscopic symmetry breaking can not occur even for the weakest coupling possible. But for an XY model in the presence of a uniaxial random field disorder, the macroscopic symmetry breaking is restored in the model. Upon driving the system with a rotating field quasi-statically while the system was attached to a zero-temperature heat bath, we see the response becomes multi-periodic where the avalanche size distribution diverges. We also found a non-equilibrium critical point which is home for a multi-periodic behavior. The increasing periodicity of response with system size grows towards non-repeatability in the thermodynamic limit, which is very much like the transition to chaos. The observed period multiplication in

this model resembles a classical discrete time-crystal. We discuss its application to electron nematic, quantum gas, and XY magnets.

In chapter 4, we worked with two variations of a deep learning model to classify images from various Ising models and percolation models. The machine learning model's better performance with a single-label classifier than the multi-label classifier was demonstrated with experimental images. The specialized symmetry reduction and rejection criteria formulated provide better robustness against anomalous predictions to the deep learning model.

We have outlined two different hysteresis protocols to distinguish an XY model with Ising symmetry from its counterparts without broken symmetry. We also devised a strategy to differentiate Ising models and percolation models with machine learning. In the process, we found a critical discrete time-crystal and similarities with a chaotic dynamical system.

REFERENCES

[1] Ido Regev, John Weber, Charles Reichhardt, Karin A Dahmen, and Turab Lookman. Reversibility and criticality in amorphous solids. *Nature Communications*, 6(1):47–8, Nov 2015. https://doi.org/10.1038/ncomms9805.

[2] Premkumar Leishangthem, Anshul D. S. Parmar, and Srikanth Sastry. The yielding transition in amorphous solids under oscillatory shear deformation. *Nature Communications*, 8(1):14653, April 2017. https://doi.org/10.1038/ncomms14653.

[3] M. P. Lilly, K. B. Cooper, J. P. Eisenstein, L. N. Pfeiffer, and K. W. West. Evidence for an anisotropic state of two-dimensional electrons in high landau levels. *Phys. Rev. Lett.*, 82:394–397, Jan 1999. https://dx.doi.org/10.1103/PhysRevLett.82.394.

[4] M. M. Fogler, A. A. Koulakov, and B. I. Shklovskii. Ground state of a two-dimensional electron liquid in a weak magnetic field. *Phys. Rev. B*, 54:1853–1871, Jul 1996. https://doi.org/10.1103/PhysRevB.54.1853.

[5] Eduardo Fradkin, Steven A. Kivelson, Efstratios Manousakis, and Kwangsik Nho. Nematic phase of the two-dimensional electron gas in a magnetic field. *Phys. Rev. Lett.*, 84:1982–1985, Feb 2000. https://dx.doi.org/10.1103/PhysRevLett.84.1982.

[6] D A Abanin, S A Parameswaran, S A Kivelson, and S L Sondhi. Nematic valley ordering in quantum Hall systems. *Physical Review B*, 82(3):035428–6, July 2010. https://doi.org/10.1103/PhysRevB.82.035428.

[7] V L Berezinskii. Destruction of long-range order in one-dimensional and two-dimensional systems having a continuous symmetry group i. classical systems. *Sov. Phys. JETP*, 32:493–500, 1971. http://www.jetp.ac.ru/cgi-bin/e/index/e/32/3/p493?a=list.

[8] J M Kosterlitz and D J Thouless. Long range order and metastability in two dimensional solids and superfluids. (Application of dislocation theory). *Journal of Physics C: Solid State Physics*, 5(11):L124–L126, Mar 2001. https://doi.org/10.1088/0022-3719/5/11/002.

[9] J. Wehr, A. Niederberger, L. Sanchez-Palencia, and M. Lewenstein. Disorder versus the mermin-wagner-hohenberg effect: From classical spin systems to ultracold atomic gases. *Phys. Rev. B*, 74:224448, Dec 2006. https://doi.org/10.1103/PhysRevB.74.224448.

[10] Dmitry A. Abanin, Patrick A. Lee, and Leonid S. Levitov. Randomness-induced *xy* ordering in a graphene quantum hall ferromagnet. *Phys. Rev. Lett.*, 98:156801, Apr 2007. https://doi.org/10.1103/PhysRevLett.98.156801.

[11] A Niederberger, T Schulte, J Wehr, M Lewenstein, L Sanchez-Palencia, and K Sacha. Disorder-Induced Order in Two-Component Bose-Einstein Condensates. *Physical Review Letters*, 100(3):5–4, January 2008. https://doi.org/10.1103/PhysRevLett.100.030403.

[12] Anindita Bera, Debraj Rakshit, Aditi Sen(De), and Ujjwal Sen. Spontaneous magnetization of quantum xy spin model in joint presence of quenched and annealed disorder. *Phys. Rev. B*, 95:224441, Jun 2017. https://doi.org/10.1103/PhysRevB.95.224441.

[13] Nicholas Crawford. Random field induced order in low dimension. *EPL (Europhysics Letters)*, 102(3):36003, 2013. https://doi.org/10.1209/0295-5075/102/36003.

[14] Anindita Bera, Debraj Rakshit, Maciej Lewenstein, Aditi Sen(De), Ujjwal Sen, and Jan Wehr. Classical spin models with broken symmetry: Random-field-induced order and persistence of spontaneous magnetization in the presence of a random field. *Phys. Rev. B*, 90:174408, Nov 2014. https://doi.org/10.1103/PhysRevB.90.174408.

[15] Anindita Bera, Debraj Rakshit, Maciej Lewenstein, Aditi Sen(De), Ujjwal Sen, and Jan Wehr. Disorder-induced enhancement and critical scaling of spontaneous magnetization in random-field quantum spin systems. *Phys. Rev. B*, 94:014421, Jul 2016. https://doi.org/10.1103/PhysRevB.94.014421.

[16] Brian J. Minchau and Robert A. Pelcovits. Two-dimensional xy model in a random uniaxial field. *Phys. Rev. B*, 32:3081–3087, Sep 1985. https://doi.org/10.1103/PhysRevB.32.3081.

[17] D. É. Fel'dman. Critical behavior of a degenerate ferromagnet in a uniaxial random field: Exact results in a space of arbitrary dimension. *Journal of Experimental and Theoretical Physics*, 88(6):1170–1178, Jun 1999. https://doi.org/10.1134/1.558907.

[18] D. N. Basov, Richard D. Averitt, Dirk van der Marel, Martin Dressel, and Kristjan Haule. Electrodynamics of correlated electron materials. *Rev. Mod. Phys.*, 83:471–541, Jun 2011. https://doi.org/10.1103/RevModPhys.83.471.

[19] G. Binnig and H. Rohrer. In touch with atoms. *Rev. Mod. Phys.*, 71:S324–S330, Mar 1999. https://doi.org/10.1103/RevModPhys.71.S324.

[20] B. Phillabaum, E. W. Carlson, and K. A. Dahmen. Spatial complexity due to bulk electronic nematicity in a superconducting underdoped cuprate. *Nature Communications*, 3(1):915, Jun 2012. https://doi.org/10.1038/ncomms1920.

[21] Shuo Liu, E. W. Carlson, and K. A. Dahmen. Connecting complex electronic pattern formation to critical exponents, 2018. https://arxiv.org/abs/1803.08485.

[22] L. Burzawa, S. Liu, and E. W. Carlson. Classifying surface probe images in strongly correlated electronic systems via machine learning. *Phys. Rev. Materials*, 3:033805, Mar 2019. https://doi.org/10.1103/PhysRevMaterials.3.033805.

[23] Shuo Liu, B. Phillabaum, E. W. Carlson, K. A. Dahmen, N. S. Vidhyadhiraja, M. M. Qazilbash, and D. N. Basov. Random field driven spatial complexity at the mott transition in vo_2. *Phys. Rev. Lett.*, 116:036401, Jan 2016. https://dx.doi.org/10.1103/PhysRevLett.116.036401.

[24] M. M. Qazilbash, M. Brehm, Byung-Gyu Chae, P.-C. Ho, G. O. Andreev, Bong-Jun Kim, Sun Jin Yun, A. V. Balatsky, M. B. Maple, F. Keilmann, Hyun-Tak Kim, and D. N. Basov. Mott transition in vo2 revealed by infrared spectroscopy and nano-imaging. *Science*, 318(5857):1750–1753, 2007. https://doi.org/10.1126/science.1150124.

[25] S. A. Kivelson, E. Fradkin, and V. J. Emery. Electronic liquid-crystal phases of a doped mott insulator. *Nature*, 393(6685):550–553, Jun 1998. https://doi.org/10.1103/10.1038/31177.

[26] Eduardo Fradkin and Steven A. Kivelson. Liquid-crystal phases of quantum hall systems. *Phys. Rev. B*, 59:8065–8072, Mar 1999. https://doi.org/10.1103/PhysRevB.59.8065.

[27] S. A. Kivelson, I. P. Bindloss, E. Fradkin, V. Oganesyan, J. M. Tranquada, A. Kapitulnik, and C. Howald. How to detect fluctuating stripes in the high-temperature superconductors. *Rev. Mod. Phys.*, 75:1201–1241, Oct 2003. https://doi.org/10.1103/RevModPhys.75.1201.

[28] R. A. Borzi, S. A. Grigera, J. Farrell, R. S. Perry, S. J. S. Lister, S. L. Lee, D. A. Tennant, Y. Maeno, and A. P. Mackenzie. Formation of a nematic fluid at high fields in sr3ru2o7. *Science*, 315(5809):214–217, 2007. https://doi.org/10.1103/10.1126/science.1134796.

[29] Chen Fang, Hong Yao, Wei-Feng Tsai, JiangPing Hu, and Steven A. Kivelson. Theory of electron nematic order in lafeaso. *Phys. Rev. B*, 77:224509, Jun 2008. https://doi.org/10.1103/PhysRevB.77.224509.

[30] Cenke Xu, Markus Müller, and Subir Sachdev. Ising and spin orders in the iron-based superconductors. *Phys. Rev. B*, 78:020501, Jul 2008. https://doi.org/10.1103/PhysRevB.78.020501.

[31] I. I. Mazin and M. D. Johannes. A key role for unusual spin dynamics in ferropnictides. *Nat Phys*, 5(2):141–145, Feb 2009. https://doi.org/10.1103/10.1038/nphys1160.

[32] Yoichi Ando, Kouji Segawa, Seiki Komiya, and A. N. Lavrov. Electrical resistivity anisotropy from self-organized one dimensionality in high-temperature superconductors. *Phys. Rev. Lett.*, 88:137005, Mar 2002. https://doi.org/10.1103/PhysRevLett.88.137005.

[33] V. Hinkov, D. Haug, B. Fauqué, P. Bourges, Y. Sidis, A. Ivanov, C. Bernhard, C. T. Lin, and B. Keimer. Electronic liquid crystal state in the high-temperature superconductor yba2cu3o6.45. *Science*, 319(5863):597–600, 2008. https://doi.org/10.1103/10.1126/science.1152309.

[34] Xiao Li, Fan Zhang, and A. H. MacDonald. Su(3) quantum hall ferromagnetism in snte. *Phys. Rev. Lett.*, 116:026803, Jan 2016. https://doi.org/10.1103/PhysRevLett.116.026803.

[35] Benjamin E. Feldman, Mallika T. Randeria, András Gyenis, Fengcheng Wu, Huiwen Ji, R. J. Cava, Allan H. MacDonald, and Ali Yazdani. Observation of a nematic quantum hall liquid on the surface of bismuth. *Science*, 354(6310):316–321, 2016. https://doi.org/10.1103/10.1126/science.aag1715.

[36] Eduardo Fradkin, Steven A. Kivelson, Michael J. Lawler, James P. Eisenstein, and Andrew P. Mackenzie. Nematic fermi fluids in condensed matter physics. *Annual Review of Condensed Matter Physics*, 1(1):153–178, 2010. https://doi.org/10.1103/10.1146/annurev-conmatphys-070909-103925.

[37] R.R. Du, D.C. Tsui, H.L. Stormer, L.N. Pfeiffer, K.W. Baldwin, and K.W. West. Strongly anisotropic transport in higher two-dimensional landau levels. *Solid State Communications*, 109(6):389 – 394, 1999. https://doi.org/10.1103/http://dx.doi.org/10.1016/S0038-1098(98)00578-X.

[38] Yizhi You, Gil Young Cho, and Eduardo Fradkin. Theory of nematic fractional quantum hall states. *Phys. Rev. X*, 4:041050, Dec 2014. https://doi.org/10.1103/PhysRevX.4.041050.

[39] Yizhi You, Gil Young Cho, and Eduardo Fradkin. Nematic quantum phase transition of composite fermi liquids in half-filled landau levels and their geometric response. *Phys. Rev. B*, 93:205401, May 2016. https://doi.org/10.1103/PhysRevB.93.205401.

[40] M. O. Goerbig. Quantum Hall Effects. *ArXiv e-prints*, September 2009. https://arxiv.org/abs/0909.1998.

[41] M. Büttiker, Y. Imry, R. Landauer, and S. Pinhas. Generalized many-channel conductance formula with application to small rings. *Phys. Rev. B*, 31:6207–6215, May 1985. https://doi.org/10.1103/PhysRevB.31.6207.

[42] P. M. Chaikin and T. C. Lubensky. *Principles of Condensed Matter Physics*. Cambridge University Press, 1995. https://doi.org/10.1017/CBO9780511813467.

[43] E W Carlson, K A Dahmen, E Fradkin, and S A Kivelson. Hysteresis and Noise from Electronic Nematicity in High-Temperature Superconductors. *Physical Review Letters*, 96(9):097003–4, Mar 2006. https://doi.org/10.1103/PhysRevLett.96.097003.

[44] K.B. Cooper, M.P. Lilly, J.P. Eisenstein, T. Jungwirth, L.N. Pfeiffer, and K.W. West. An investigation of orientational symmetry-breaking mechanisms in high landau levels. *Solid State Communications*, 119(2):89 – 94, 2001. https://doi.org/10.1103/http://dx.doi.org/10.1016/S0038-1098(01)00212-5.

[45] A. A. Koulakov, M. M. Fogler, and B. I. Shklovskii. Charge density wave in two-dimensional electron liquid in weak magnetic field. *Phys. Rev. Lett.*, 76:499–502, Jan 1996. https://doi.org/10.1103/PhysRevLett.76.499.

[46] R. Moessner and J. T. Chalker. Exact results for interacting electrons in high landau levels. *Phys. Rev. B*, 54:5006–5015, Aug 1996. https://doi.org/10.1103/PhysRevB.54.5006.

[47] Vadim Oganesyan, Steven A. Kivelson, and Eduardo Fradkin. Quantum theory of a nematic fermi fluid. *Phys. Rev. B*, 64:195109, Oct 2001. https://doi.org/10.1103/PhysRevB.64.195109.

[48] Lars Onsager. Crystal statistics. i. a two-dimensional model with an order-disorder transition. *Phys. Rev.*, 65:117–149, Feb 1944. https://doi.org/10.1103/PhysRev.65.117.

[49] S. Basak and E. W. Carlson. Distinguishing xy from ising electron nematics. *Phys. Rev. B*, 96:081303, Aug 2017. https://doi.org/10.1103/PhysRevB.96.081303.

[50] M. P. Lilly, K. B. Cooper, J. P. Eisenstein, L. N. Pfeiffer, and K. W. West. Anisotropic states of two-dimensional electron systems in high landau levels: Effect of an in-plane magnetic field. *Phys. Rev. Lett.*, 83:824–827, Jul 1999. https://dx.doi.org/10.1103/PhysRevLett.83.824.

[51] Q. Shi, M. A. Zudov, J. D. Watson, G. C. Gardner, and M. J. Manfra. Reorientation of quantum hall stripes within a partially filled landau level. *Phys. Rev. B*, 93:121404, Mar 2016. https://doi.org/10.1103/PhysRevB.93.121404.

[52] Q. Shi, M. A. Zudov, J. D. Watson, G. C. Gardner, and M. J. Manfra. Evidence for a new symmetry breaking mechanism reorienting quantum hall nematics. *Phys. Rev. B*, 93:121411, Mar 2016. https://doi.org/10.1103/PhysRevB.93.121411.

[53] Sunanda P Koduvayur, Yuli Lyanda-Geller, Sergei Khlebnikov, Gabor Csathy, Michael J Manfra, Loren N Pfeiffer, Kenneth W West, and Leonid P Rokhinson. Effect of Strain on Stripe Phases in the Quantum Hall Regime. *Physical Review Letters*, 106(1):016804–4, Jan 2011. https://dx.doi.org/10.1103/PhysRevLett.106.016804.

[54] J. Zhu, W. Pan, H. L. Stormer, L. N. Pfeiffer, and K. W. West. Density-induced interchange of anisotropy axes at half-filled high landau levels. *Phys. Rev. Lett.*, 88:116803, Mar 2002. https://dx.doi.org/10.1103/PhysRevLett.88.116803.

[55] E. W. Carlson and K. A. Dahmen. Using disorder to detect locally ordered electron nematics via hysteresis. *Nature Communications*, 2:379, Jul 2011. https://doi.org/10.1038/ncomms1375.

[56] Ken B. Cooper. *New Phases of Two-Dimensional Electrons in Excited Landau Levels*. PhD thesis, California Institute of Technology, 2003. http://thesis.library.caltech.edu/2125/1/KenBCooperThesis.pdf.

[57] J M Kosterlitz. The critical properties of the two-dimensional xy model. *Journal of Physics C: Solid State Physics*, 1974. https://doi.org/10.1088/0022-3719/7/6/005.

[58] Ravá da Silveira and Mehran Kardar. Critical hysteresis for n-component magnets. *Phys. Rev. E*, 59:1355–1367, Feb 1999. https://doi.org/10.1103/PhysRevE.59.1355.

[59] Karin Dahmen and James P. Sethna. Hysteresis, avalanches, and disorder-induced critical scaling: A renormalization-group approach. *Phys. Rev. B*, 53:14872–14905, Jun 1996. https://doi.org/10.1103/PhysRevB.53.14872.

[60] Q. Shi, M. A. Zudov, B. Friess, J. Smet, J. D. Watson, G. C. Gardner, and M. J. Manfra. Apparent temperature-induced reorientation of quantum hall stripes. *Phys. Rev. B*, 95:161404, Apr 2017. https://dx.doi.org/10.1103/PhysRevB.95.161404.

[61] Lacour-Gayet, P. and Toulouse, G. Ideal bose einstein condensation and disorder effects. *J. Phys. France*, 35(5):425–432, 1974. https://doi.org/10.1051/jphys:01974003505042500.

[62] Kazushi Aoyama and Ryusuke Ikeda. Pairing states of superfluid ^{3}He in uniaxially anisotropic aerogel. *Phys. Rev. B*, 73:060504, Feb 2006. https://doi.org/10.1103/PhysRevB.73.060504.

[63] S. Ostlund and B. I. Halperin. Dislocation-mediated melting of anisotropic layers. *Phys. Rev. B*, 23:335–358, Jan 1981. https://doi.org/10.1103/PhysRevB.23.335.

[64] David R. Nelson and B. I. Halperin. Dislocation-mediated melting in two dimensions. *Phys. Rev. B*, 19:2457–2484, Mar 1979. https://doi.org/10.1103/PhysRevB.19.2457.

[65] B. I. Halperin and David R. Nelson. Theory of two-dimensional melting. *Phys. Rev. Lett.*, 41:121–124, Jul 1978. https://doi.org/10.1103/PhysRevLett.41.121.

[66] A. P. Young. Melting and the vector coulomb gas in two dimensions. *Phys. Rev. B*, 19:1855–1866, Feb 1979. https://doi.org/10.1103/PhysRevB.19.1855.

[67] S. M. Girvin and A. H. MacDonald. Multicomponent quantum hall systems: The sum of their parts and more. *Perspectives in Quantum Hall Effects: Novel Quantum Liquids in Low-Dimensional Semiconductor Structures, ed. Das Sarma and Pinczuk*. https://doi.org/10.1002/9783527617258.ch5.

[68] J M Kosterlitz and D Thouless. Ordering, metastability and phase transitions in two-dimensional systems. *Journal of Physics C: Solid State Physics*, 6:1181, 1973. https://doi.org/10.1088/0022-3719/6/7/010.

[69] Yoseph Imry and Shang-keng Ma. Random-field instability of the ordered state of continuous symmetry. *Phys. Rev. Lett.*, 35:1399–1401, Nov 1975. https://doi.org/10.1103/PhysRevLett.35.1399.

[70] Norman Y. Yao, Chetan Nayak, Leon Balents, and Michael P. Zaletel. Classical discrete time crystals. *Nature Physics*, 16(4):438–447, Apr 2020. https://doi.org/10.1038/s41567-019-0782-3.

[71] Alfred Shapere and Frank Wilczek. Classical time crystals. *Phys. Rev. Lett.*, 109:160402, Oct 2012. https://doi.org/10.1103/PhysRevLett.109.160402.

[72] Daniel S. Fisher. Scaling and critical slowing down in random-field ising systems. *Phys. Rev. Lett.*, 56:416–419, Feb 1986. https://doi.org/10.1103/PhysRevLett.56.416.

[73] J P Sethna, K A Dahmen, and C R Myers. Crackling noise. *Nature*, 410:242, 2001. https://doi.org/10.1038/35065675.

[74] Sayan Basak, Erica Carlson, and Karin Dahmen. Period n-tupling in uniaxial random field xy magnet with rotating driving field. *Purdue University Research Repository*, Sep 2019. https://doi.org/10.4231/B90H-VH37.

[75] Ido Regev, Turab Lookman, and Charles Reichhardt. Onset of irreversibility and chaos in amorphous solids under periodic shear. *Phys. Rev. E*, 88:062401, Dec 2013. https://doi.org/10.1103/PhysRevE.88.062401.

[76] Vedika Khemani, Achilleas Lazarides, Roderich Moessner, and S L Sondhi. Phase Structure of Driven Quantum Systems. *Physical Review Letters*, 116(25):250401–6, June 2016. https://doi.org/10.1103/PhysRevLett.116.250401.

[77] Dominic V Else, Bela Bauer, and Chetan Nayak. Prethermal Phases of Matter Protected by Time-Translation Symmetry. *Physical Review X*, 7(1):1515–21, March 2017. https://doi.org/10.1103/PhysRevX.7.011026.

[78] N Y Yao, A C Potter, I D Potirniche, and A Vishwanath. Discrete Time Crystals: Rigidity, Criticality, and Realizations. *Physical Review Letters*, 118(3):030401–6, January 2017. https://doi.org/10.1103/PhysRevLett.118.030401.

[79] Toni L Heugel, Matthias Oscity, Alexander Eichler, Oded Zilberberg, and R Chitra. Classical Many-Body Time Crystals. *Physical Review Letters*, 123(12):124301, September 2019. https://doi.org/10.1103/PhysRevLett.123.124301.

[80] Vedika Khemani, Roderich Moessner, and S L Sondhi. A Brief History of Time Crystals. *ArXiv*, page 1910.10745, October 2019. https://arxiv.org/abs/1910.10745.

[81] Wing Chi Yu, Jirawat Tangpanitanon, Alexander W Glaetzle, Dieter Jaksch, and Dimitris G Angelakis. Discrete time crystal in globally driven interacting quantum systems without disorder. *Physical Review A*, 99:033618, March 2019. https://doi.org/10.1103/PhysRevA.99.033618.

[82] S A Kivelson, I P Bindloss, E Fradkin, V Oganesyan, J M Tranquada, A Kapitulnik, and C Howald. How to detect fluctuating stripes in the high-temperature superconductors. *Reviews of Modern Physics*, 75:1201–1241, October 2003. https://doi.org/10.1103/RevModPhys.75.1201.

[83] E Fradkin and S A Kivelson. Electron nematic phases proliferate. *Science*, 327(5962):155, August 2010. https://doi.org/10.1126/science.1183464.

[84] E W Carlson and K A Dahmen. Using disorder to detect locally ordered electron nematics via hysteresis. *Nature Communications*, 2:379, July 2011. https://doi.org/10.1038/ncomms1375.

[85] Laurent Sanchez-Palencia and Maciej Lewenstein. Disordered quantum gases under control. *Nature Physics*, 6(2):87–95, February 2010. https://doi.org/10.1038/nphys1507.

[86] Prabodh Shukla and R. S. Kharwanlang. Critical hysteresis in random-field XY and heisenberg models. *Phys. Rev. E*, 83:011121, Jan 2011. https://doi.org/10.1103/PhysRevE.83.011121.

[87] Michael E. Fisher. The renormalization group in the theory of critical behavior. *Rev. Mod. Phys.*, 46:597–616, Oct 1974. https://doi.org/10.1103/RevModPhys.46.597.

[88] Olga Perković, Karin Dahmen, and James P. Sethna. Avalanches, barkhausen noise, and plain old criticality. *Phys. Rev. Lett.*, 75:4528–4531, Dec 1995. https://doi.org/10.1103/PhysRevLett.75.4528.

[89] Youjin Deng and Henk W. J. Blöte. Monte carlo study of the site-percolation model in two and three dimensions. *Phys. Rev. E*, 72:016126, Jul 2005. https://doi.org/10.1103/PhysRevE.72.016126.

[90] E. W. Carlson, Shuo Liu, B. Phillabaum, and K. A. Dahmen. Decoding spatial complexity in strongly correlated electronic systems. *Journal of Superconductivity and Novel Magnetism*, 28(4):1237–1243, Apr 2015. https://doi.org/10.1007/s10948-014-2898-0.

[91] Diederik P. Kingma and Jimmy Ba. Adam: A Method for Stochastic Optimization. *arXiv e-prints*, page arXiv:1412.6980, December 2014. https://arxiv.org/abs/1412.6980.

[92] K. S. Sivamani, R. Sahay, and A. E. Gamal. Non-intrusive detection of adversarial deep learning attacks via observer networks. *IEEE Letters of the Computer Society*, 3(1):25–28, 2020. https://doi.org/10.1109/LOCS.2020.2990897.

[93] A. Zimmers, L. Aigouy, M. Mortier, A. Sharoni, Siming Wang, K. G. West, J. G. Ramirez, and Ivan K. Schuller. Role of thermal heating on the voltage induced insulator-metal transition in vo_2. *Phys. Rev. Lett.*, 110:056601, Jan 2013. https://doi.org/10.1103/PhysRevLett.110.056601.